Challenge Journal of STRUCTURAL MECHANICS

Vol.11 No.4 (2025)

auxetic buckling load building codes
compressive strength dynamic analysis
earthquake finite element method
girder bridge Jaya algorithm metaheuristic
algorithms modal analysis optimization
prestresing pushover analysis reinforced
concrete seismic design shallow foundations
smart concrete stability static analysis
steel structures structural dynamics
temperature effects thick plate wind

ISSN 2149-8024

TULPAR ACADEMIC PUBLISHING

Challenge Journal of Structural Mechanics

E-mail: *cjsmec@challengejournal.com*

Web page: *cjsmec.challengejournal.com*

Tulpar Academic Publishing
www.tulparpublishing.com

Challenge Journal of Structural Mechanics

CONTENTS

Research Articles

TULPAR ACADEMIC PUBLISHING

Challenge Journal of Structural Mechanics

Research Article

Enhancing the mechanical performance of perforated steel plates through fiber-reinforced composite reinforcement: A finite element analysis study

Husam A. M. Alshabrawi [a,*], Habib Uysal [a]

[a] *Department of Civil Engineering, Atatürk University, Erzurum 25240, Türkiye*

ABSTRACT

Reinforced concrete and steel plates are widely used in civil engineering and are important components of many structural systems and ground reinforcement projects. These plates effectively carry different loads, enhance ground support, and improve the durability of structures. Moreover, the proper selection and use of these materials during the design and planning stages of construction projects have a direct impact on cost and time efficiency. In addition to their structural contributions, the effective use of reinforced concrete and steel plates is critical for the safety and success of construction projects. In order to transfer loads to the frame system, reinforced concrete plates serve as horizontal load-carrying components. Load-bearing capacity, stiffness, fire resistance, and sound insulation are important properties of reinforced concrete plates. Perforated plates are widely used in structural applications but suffer from stress concentration around openings, reducing their mechanical performance. This study investigates the reinforcement of perforated steel plates using fiber-reinforced polymer (FRP) composites around holes to enhance structural integrity. The research employs finite element analysis (FEA) to assess the effects of different reinforcement widths under varying loads. A detailed comparison of stress and deformation distributions before and after reinforcement is presented. The findings indicate that FRP reinforcement significantly reduces stress concentration and improves the load-bearing capacity of perforated plates, providing practical insights for industrial and construction applications.

ARTICLE INFO

Article history:
Received – January 7, 2025
Revision requested – February 5, 2025
Revision received – April 22, 2025
Accepted – May 5, 2025

Keywords:
Perforated plates
Reinforcement techniques
Fiber-reinforced polymer composites
Finite element analysis
Stress distribution
Mechanical performance

Citation: Alshabrawi HAM, Uysal H (2025). Enhancing the mechanical performance of perforated steel plates through fiber-reinforced composite reinforcement: A finite element analysis study. *Challenge Journal of Structural Mechanics*, 11(4), 174–183.

1. Introduction

Plates are structural elements characterized by their two-dimensional geometry, where their thickness is small relative to their other dimensions. They play critical roles in enhancing structural integrity in architectural applications, reinforced concrete and steel structures, the automotive industry, and various industrial sectors.

Perforated plates are widely used in engineering projects (Zhou 2016). These plates are components made of metals, plastics, or fiber-reinforced composites with regularly or irregularly arranged holes on their surfaces.

Steel is one of the most commonly used metallic materials for perforated plates due to its strength, durability, and cost-effectiveness. Steel perforated plates are resistant to impact, abrasion, and harsh environmental conditions, making them suitable for demanding applications in industries such as construction, automotive, and manufacturing. The high tensile strength of steel allows for the creation of plates with various hole sizes and patterns without compromising structural integrity. Moreo-

* *Corresponding author*. E-mail address: silva.hosam.ma@gmail.com (H. A. M. Alshabrawi)
ISSN: 2149-8024 / DOI: https://doi.org/10.20528/cjsmec.2025.04.001

ver, steel is easily formable and manufacturable, enabling customization to meet specific design requirements.

Composite structures are often used in many areas due to their lightweight nature and adaptability to changing mechanical conditions (Demir 2024; Sunar and Uysal 2024). Using composites called fiber-reinforced polymers, obtained by combining fibers with high-strength proper-ties with the help of epoxy resin, has become widespread in the last twenty years. Carbon fiber is a lightweight and high-strength reinforcement material commonly used in advanced composite materials. Carbon fiber composites exhibit exceptional strength-to-weight ratios, stiffness, and resistance to temperature variations (Hou et al. 2025). Compared to traditional materials such as steel or aluminum, these composites offer superior mechanical properties. Carbon fiber is widely utilized in industries such as aerospace, automotive, wind energy, sports equipment, and high-performance engineering. The use of carbon fiber composites helps reduce the weight of structures without compromising strength, making them an ideal choice for applications where weight reduction is critical (Tarhan et al. 2025; Xie et al. 2020).

Durability is a critical factor to consider when selecting perforated plates. The strength of a plate determines its ability to withstand loads and forces without deformation or failure. Plates with higher strength can support heavier loads and provide increased structural stability, making them suitable for demanding applications. The strength of a plate depends on various factors such as material composition, thickness, and manufacturing processes. To effectively meet the requirements of an application, careful attention must be given to the anticipated loads and forces the plate will encounter, ensuring the selection of a plate with adequate strength.

Reinforced concrete plates are structural elements that act as horizontal load-carrying components, transferring loads to the frame system. Key characteristics of reinforced concrete plates include load-bearing capacity, rigidity, fire resistance, and sound insulation. These plates are particularly suitable for spanning large distances and allow for the addition of extra layers to structures (Baş 2024).

Reinforced concrete plates are widely used in building floors. Additionally, they are frequently preferred in industrial facilities, bridge structures, water structures, and infrastructure projects. Due to their high strength and durability, they provide excellent solutions for spanning large distances and meeting various structural needs.

Steel plates are often made of high-strength steel alloys and are available in various thicknesses. These plates can be composed of carbon steel, stainless steel, or alloy steel, offering durability, high strength, and flexibility. These characteristics make steel plates widely applicable in civil engineering.

Steel plates are commonly used in load-bearing systems of large-span structures in civil engineering. Additionally, they are preferred for industrial facilities, infrastructure projects, bridges, viaducts, warehouses, crane beams, and high-rise buildings. Steel plates are also extensively applied in vehicle and train passageways (Demirel 2023).

Perforated plates, often made of steel, are structural components with regularly spaced holes that significantly reduce weight while maintaining flexibility and durability. These advantageous features make perforated plates highly effective and widely used in large-span structural elements and ground reinforcement applications. They are preferred in engineering designs for their combination of robustness and economic efficiency, contributing significantly to the construction industry (Caştur 2021).

Perforated plates are frequently used in ground reinforcement applications and large-span structural elements. They are also commonly applied in bridges, buildings, crane beams, and platforms that carry heavy loads. By reducing weight, they provide significant cost savings and offer greater flexibility and load-bearing capacity compared to solid steel plates. Their versatility, durability, and adaptability to various projects have made perforated plates indispensable in structural engineering (Yücesoy 2021).

This paper is prepared to examine the benefits of using fiber-reinforced composites, an innovative reinforcement method, to improve the strength of perforated plates. The goal is to enhance the performance of these plates and provide engineers and designers with more innovative and effective solutions for construction and industrial applications. Within this scope, a steel plate with a central hole was reinforced around the hole using fiber-reinforced polymer (FRP) composites of varying widths. The study investigates the effectiveness of these reinforcements made with composite materials to achieve higher performance in structural applications.

2. Materials and Method

Reinforced concrete and steel plates are commonly utilized in civil engineering and play significant roles in various structural systems and ground reinforcement works. In addition to their structural contributions, the effective use of reinforced concrete and steel plates is critical for the safety and success of construction projects. Their flexibility in engineering applications, as well as their adaptability to various climatic conditions and subsurface environments, make these materials invaluable in the field of engineering. The wide range of applications, the improvement in labor efficiency, and the acceleration of construction processes further highlight their significance (Seçkin 2022).

2.1. Composite materials

Composite materials have been gaining increasing popularity in both the industrial and construction sectors, a trend that continues to strengthen each year. Owing to their unique advantages and distinctive properties, many industries have started to favor the use of such materials. Composites, created by combining materials with different characteristics, are particularly notable for being lighter than metals and plastics. This quality enables composite materials to stand out in various applications.

Detailed investigations address topics such as the definition, properties, types, classification, advantages, and disadvantages of composites, supported by comprehensive research. These studies aim to provide extensive knowledge on how to utilize these materials most effectively in both theoretical and practical fields. For instance, composites are widely used in applications where both strength and lightness are required simultaneously. Therefore, their application in construction projects and engineering designs contributes to improving processes and final outcomes, enhancing safety standards, and significantly supporting the overall efficiency of projects.

Composite materials represent a type of material created through the combination of different components to produce a stronger and more durable result. They typically consist of a matrix material reinforced with a secondary material. The harmonious integration of these two components endows composite materials with superior characteristics, such as high strength, lightness, flexibility, and chemical resistance. These unique attributes make composites widely utilized across various sectors, including construction, aerospace, automotive, and sports. As a result, composite materials play a significant role in modern engineering designs and excel in diverse applications (Yılmaz and Vural 2018).

2.2. Strengthening of plates

Extensive research conducted in the fields of structural engineering and materials science on plate strengthening holds significant importance. Considering that enhancing the resistance and durability of structures substantially contributes to structural safety and extends their service life, this subject is of critical relevance. Such studies aim to develop various methods and techniques for reinforcing plates. Therefore, in-depth investigations into plate strengthening have the potential to improve the safety and longevity of structures while enriching the existing body of knowledge. These efforts are valuable not only in the field of engineering but also for offering environmentally sustainable outcomes.

The increasing number of studies on plate strengthening is enabling structures to become more resilient. This trend holds great importance not only in academic circles but also in industrial and practical applications. The results obtained from strengthening plates in engineering projects form the basis for the reliable and efficient performance of numerous structures. In this context, the development of innovative techniques and the improvement of existing methods for plate strengthening offer significant contributions to researchers and engineering professionals alike. As a result, projects aimed at enhancing structural durability and safety can be further advanced, laying the groundwork for sustainable engineering approaches.

Furthermore, the discovery of innovative methods in this domain serves the development of the construction sector, thereby paving the way for a healthier future from both economic and environmental perspectives. The strengthening of plates will remain a noteworthy field of research and application both now and in the future.

Plates, one of the fundamental components of a structure, are horizontal structural elements that bear and transmit loads. Proper support and reinforcement of plates are essential for ensuring structural integrity and durability. Since their primary function is to transmit and bear vertical loads, strengthening plates can enhance the long-term stability and performance of structures. The definition and importance of plates are fundamental topics for professionals in structural engineering and the construction sector, playing a critical role in effectively planning and implementing strengthening projects.

Strengthening plates offers numerous structural and economic advantages. Structural benefits include increased durability, enhanced resistance to earthquakes, and extended service life of structures. These advantages improve the safety of buildings and other structures, ensuring longer-lasting performance.

2.3. Numerical modelling

Finite element analysis (FEA) is a computerized method used to predict how a product reacts to real-world forces, such as mechanical stresses, vibrations, thermal fluctuations, fluid flow dynamics, and other physical effects. FEA enables engineers to simulate the behavior of complex structures and systems by creating a virtual model composed of finite elements. By applying loads, constraints, and boundary conditions, engineers can observe and analyze the impacts on a product's performance and durability. Over the years, FEA has proven to be an invaluable tool in the design and development of a wide range of products, including perforated trays, sieves, and gas-preventing mats. Its industry-specific and application-focused approach has revolutionized the way engineers address engineering challenges, providing efficient and optimized designs for various sectors (Chen et al. 2022; Abualigah et al. 2022).

In this study, a steel plate with a central hole was analyzed under three different force values: 1.5 kN, 2.0 kN, and 3.0 kN. The study considered both unreinforced and reinforced scenarios, with FRP layers of varying widths (40 mm, 50 mm, and 60 mm) applied symmetrically around the hole.

An advanced finite element method based software ANSYS were used to create and analyse the models. The material properties used in the numerical model are presented in Table 1. Determining the mesh size, Cheng and Zhao (2010) and Singh and Singh (2021) were taken into account and the similar modeling procedure in these studies was followed. Finite element analysis was performed to simulate the behavior of perforated steel plates under static loading.

3. Results and Discussion

In perforated plates, lateral buckling and stress accumulation are commonly observed problems. These issues reduce the load-carrying capacity of the plates and shorten their service life. Additionally, significant stress concentrations occur around the perforations. Reinforcement is critically important to address these weaknesses.

In this study, the effects of using fiber materials to enhance the mechanical strength of perforated plates were analyzed in detail. The analyses were conducted using the advanced finite element method (FEM)-based ANSYS software, evaluating critical mechanical parameters such as total deformation, equivalent stress (von-Mises stress), The primary objective of this study was to systematically investigate the extent to which the fiber material added around the perforation could improve the overall strength of the plate.

During the modeling process, the perforated plate was designed as a simple rectangular geometry with a length of 300 mm, a height of 200 mm, and a width of 30 mm. At the center of the plate, a circular perforation with a diameter of 30 mm was included.

In the first stage, the behavior of the plate was analyzed before adding the composite material using three different forces 1.5, 2.0, and 3.0 kN as shown in Fig. 1. The plate was fixed from the top and bottom with a fixed support as shown in Fig. 2, and the analysis results obtained for each load value are given in Figs. 3–5, respectively.

Table 1. Material parameters used in modelling.

Material	Unit volume weight (kg/m^3)	Modulus of elasticity (Pa)	Poisson's ratio (–)
FRP composites	1600	2.30e+11	0.30
Structural steel	7850	2.00e+11	0.28

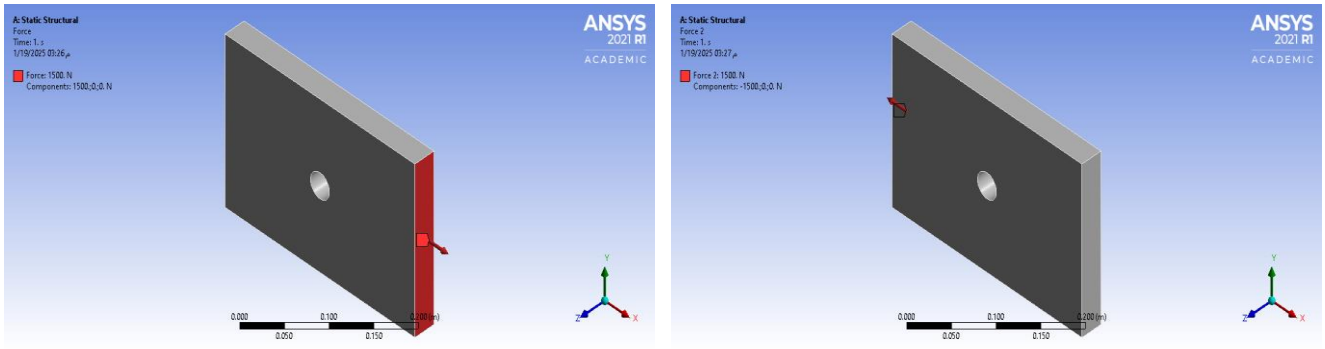

Fig. 1. Force applied from the right and left sides (1.5, 2.0 and 3.0 kN applied respectively).

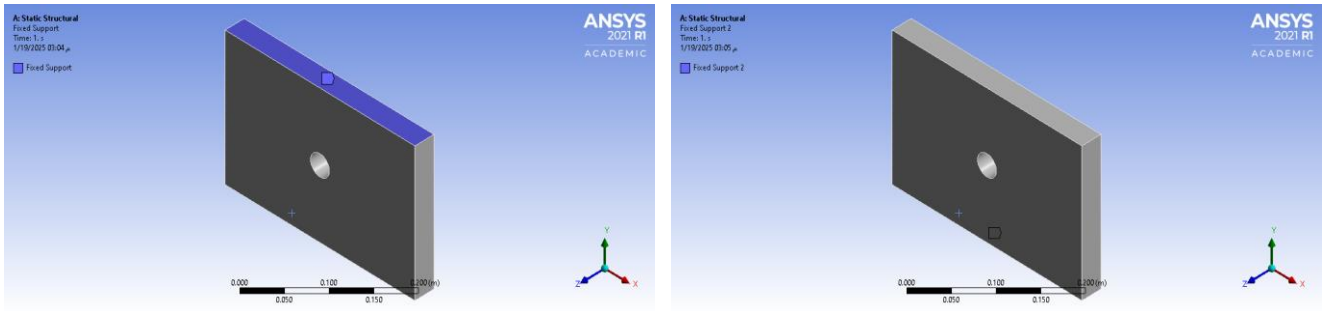

Fig. 2. Fixed support at the top and lower sides.

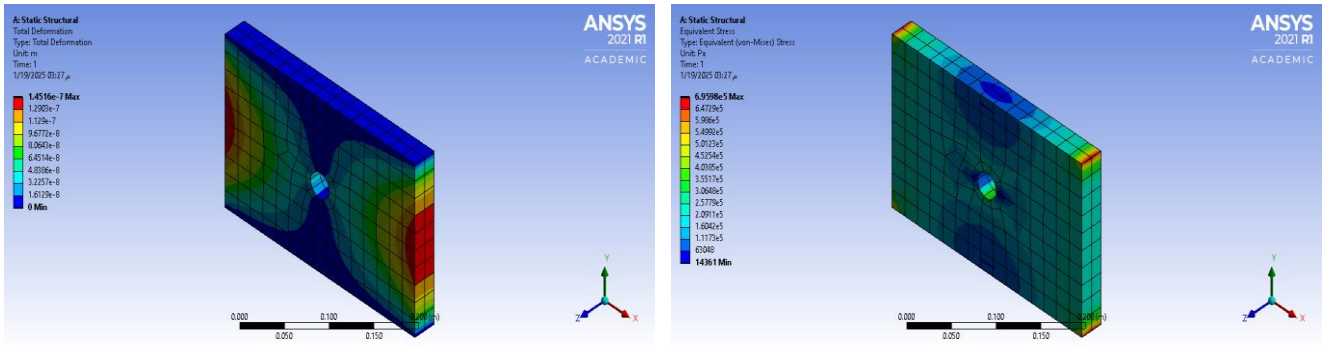

Fig. 3. Total deformation and equivalent stress distribution (1.5 kN).

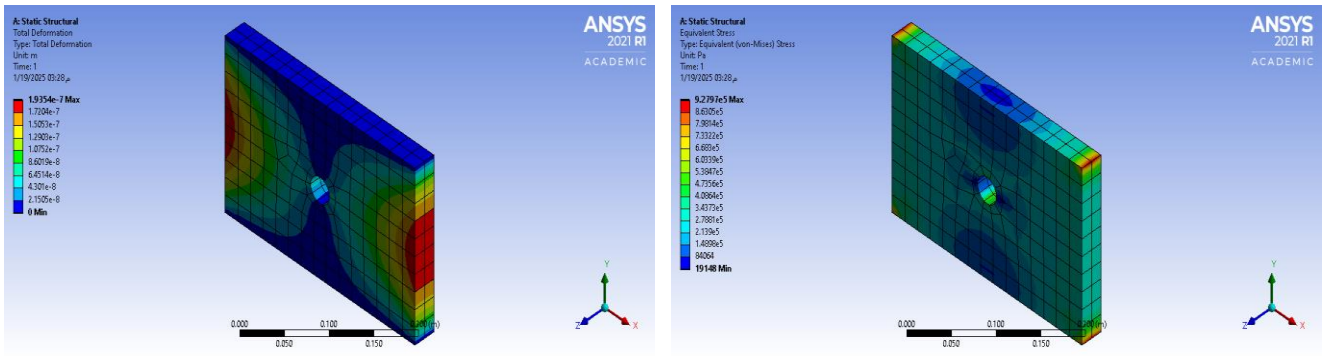

Fig. 4. Total deformation and equivalent stress distribution (2.0 kN).

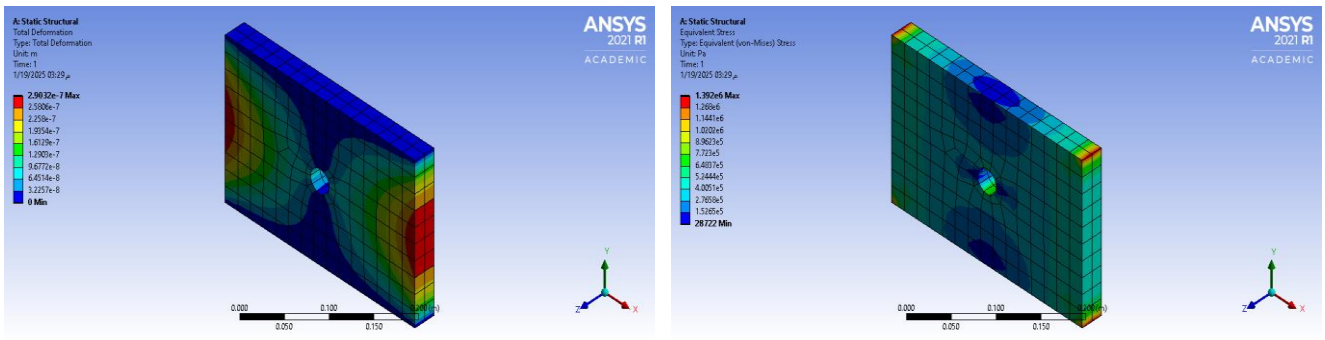

Fig. 5. Total deformation and equivalent stress distribution (3.0 kN).

In second case, carbon fiber reinforced composite material in varying widths was used for the plate (40×200 mm^2, 50×200 mm^2 and 60×200 mm^2). Loads of 1.5, 2.0, and 3.0 kN were applied to both the right and left edges, respectively. Loads of 1.5, 2.0, and 3.0 kN were applied to both the right and left edges, respectively as shown in Fig. 6, and a fixed support was added to the upper and lower edges as shown in Fig. 7.

The results were obtained by linear static analysis using ANSYS software. The total deformation and equivalent stress (von Mises) distribution resulting from the analysis are shown in Figs. 8–16.

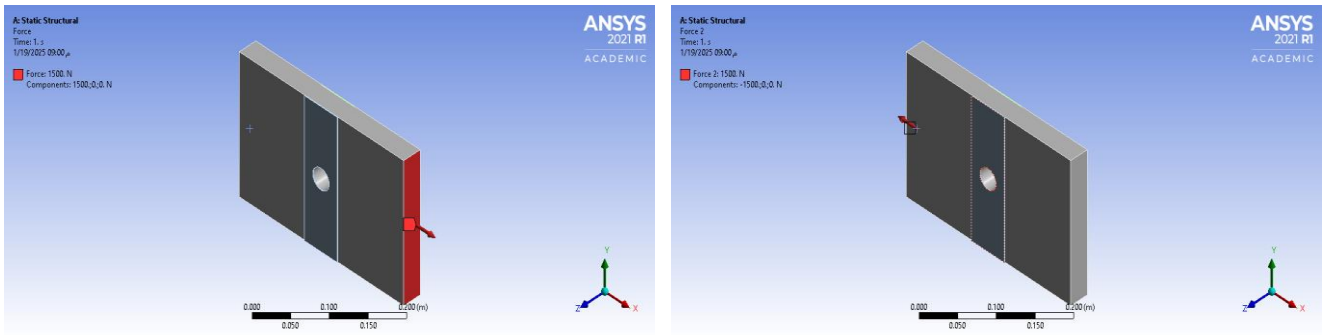

Fig. 6. Force applied from the right and left sides (1.5 kN).

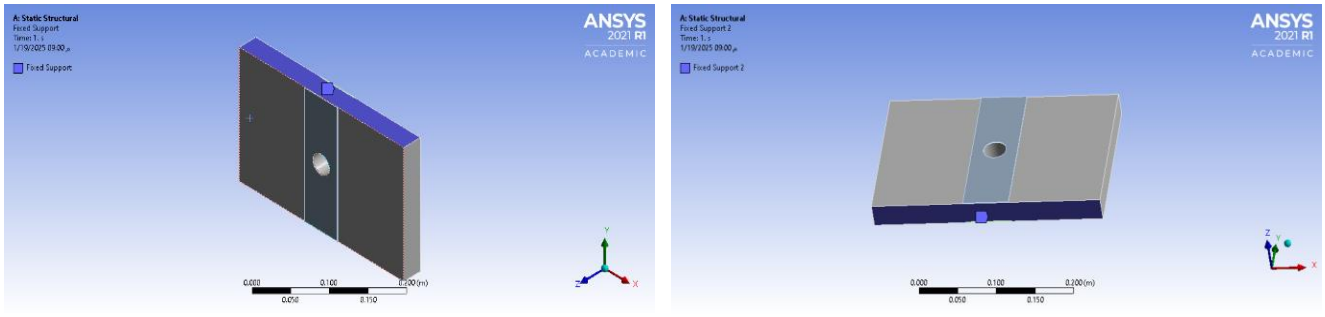

Fig. 7. Fixed support at the top and lower sides.

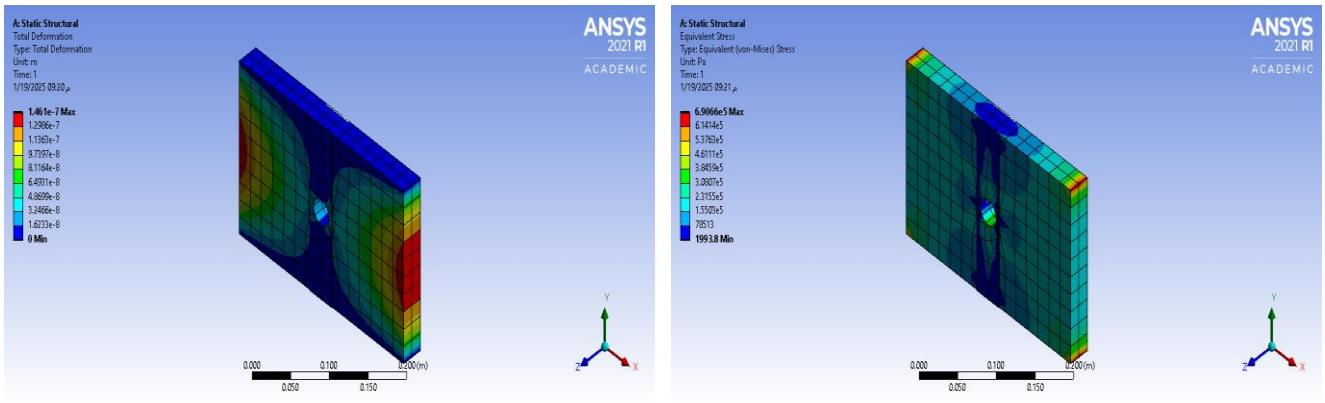

Fig. 8. Total deformation and equivalent stress distribution (FRP=40×200 mm² and *F*=1.5 kN).

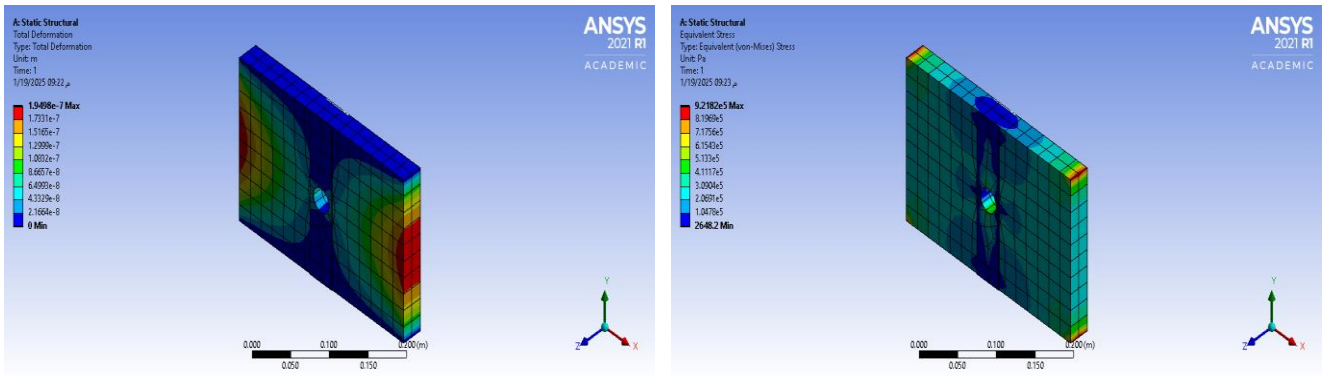

Fig. 9. Total deformation and equivalent stress distribution (FRP=40×200 mm² and *F*=2.0 kN).

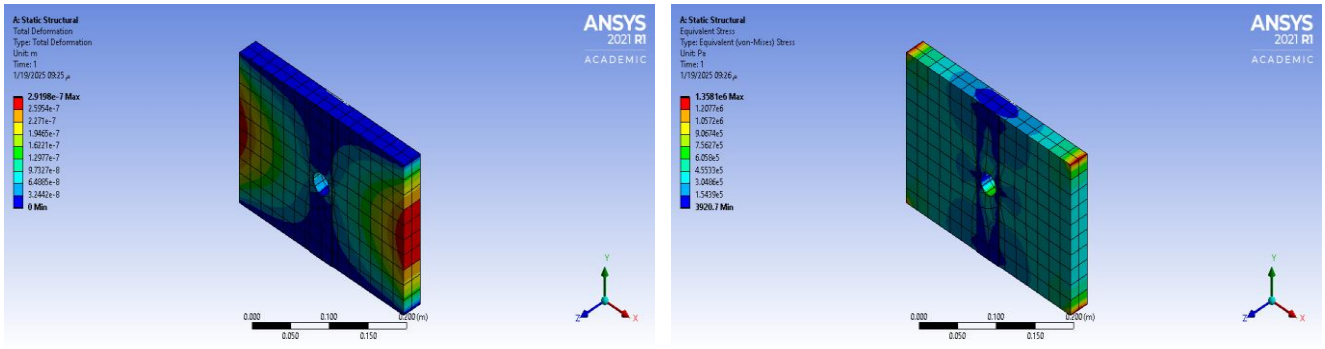

Fig. 10. Total deformation and equivalent stress distribution (FRP=40×200 mm² and *F*=3.0 kN).

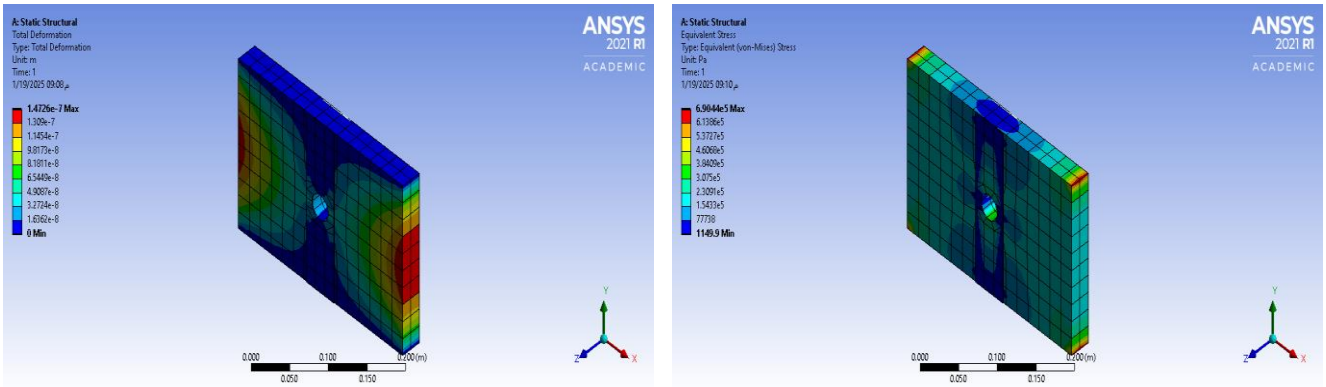

Fig. 11. Total deformation and equivalent stress distribution (FRP=50×200 mm² and *F*=1.5 kN).

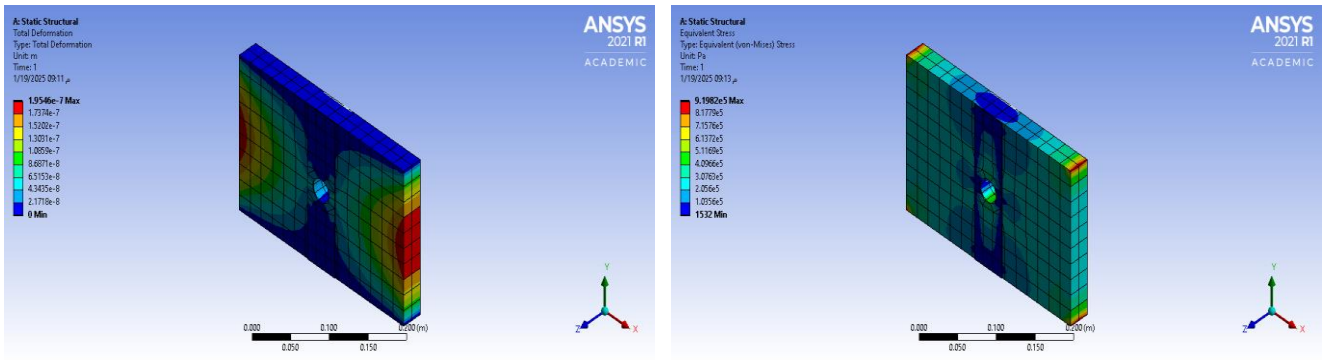

Fig. 12. Total deformation and equivalent stress distribution (FRP=50×200 mm² and *F*=2.0 kN).

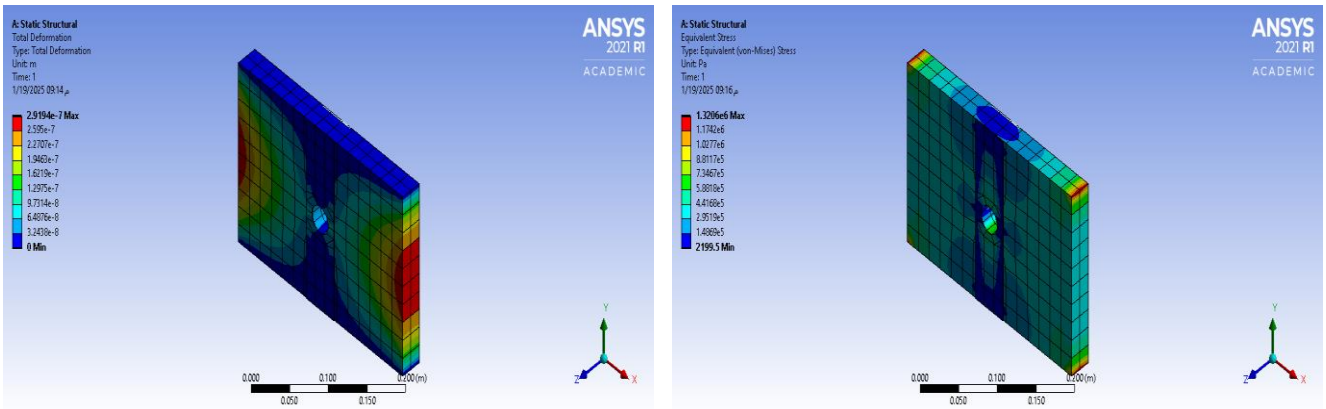

Fig. 13. Total deformation and equivalent stress distribution (FRP=50×200 mm² and *F*=3.0 kN).

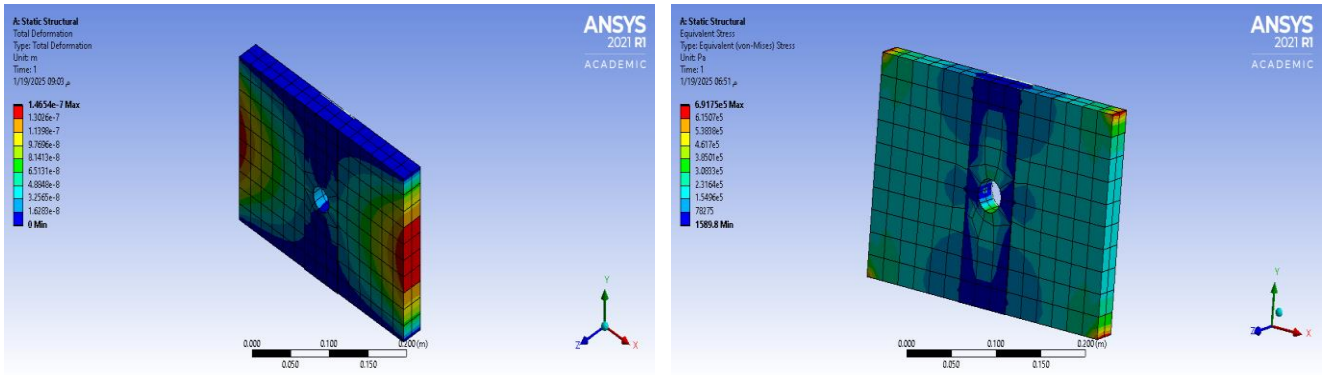

Fig. 14. Total deformation and equivalent stress distribution (FRP=60×200 mm² and *F*=1.5 kN).

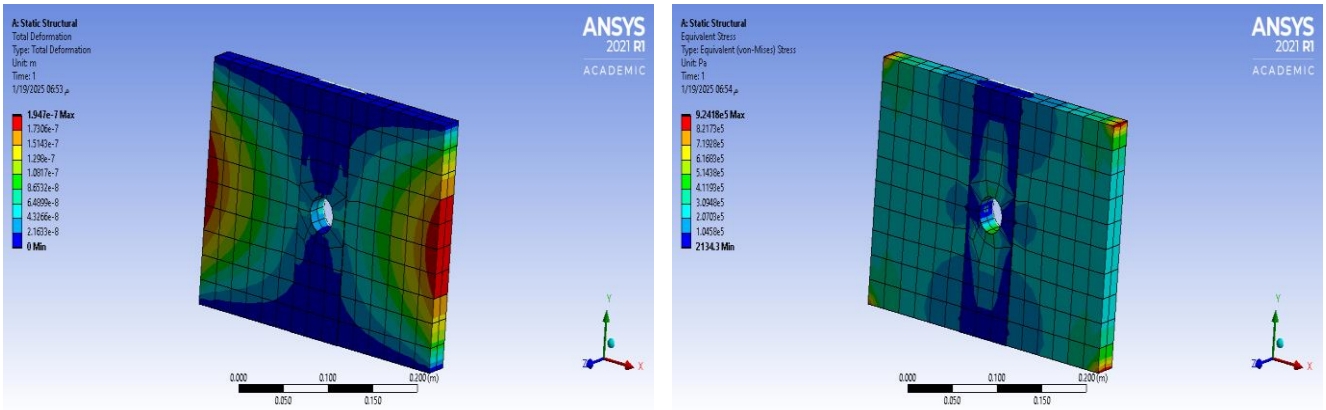

Fig. 15. Total deformation and equivalent stress distribution (FRP=60×200 mm² and *F*=2.0 kN).

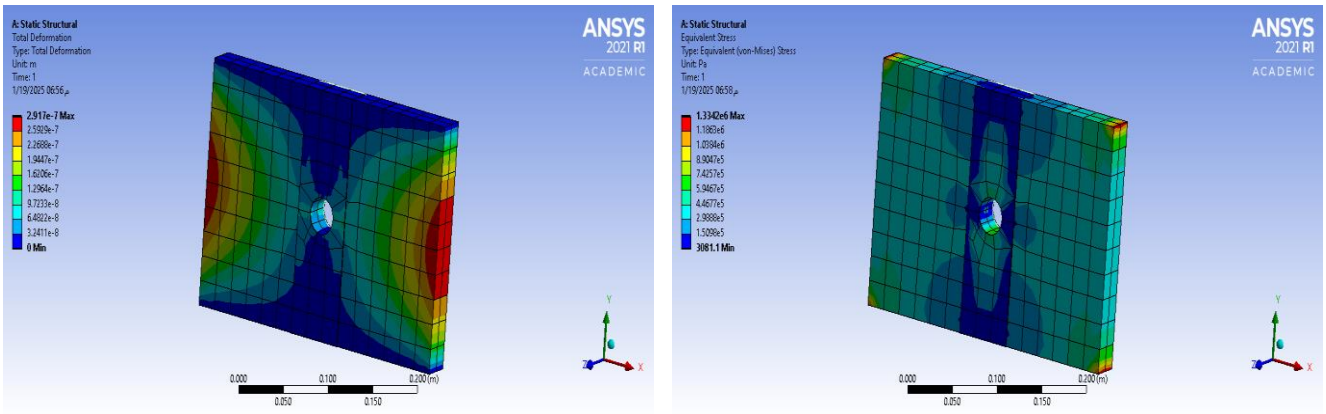

Fig. 16. Total deformation and equivalent stress distribution (FRP=60×200 mm² and *F*=3.0 kN).

Figs. 3–5 illustrate the stress concentration and deformation in the unreinforced plate under different load conditions. The results confirm that stress accumulation is highest around the hole, leading to significant structural weakening.

Figs. 8–16 present the deformation and stress distribution in the reinforced plates for different reinforcement widths. The results demonstrate a clear improvement in load-bearing capacity, with stress concentration significantly reduced as the reinforcement width increases.

Table 2 shows the change in total deformation and equivalent stress values before and after reinforcement by the composite material.

Figs. 17–19 show the linear relationship between the stress and total deformation values induced by the applied force for the cases before and after the addition of the composite material.

Table 2. Evaluation of the reinforcement effect.

		Parameters	Before fiber reinforcement	After fiber reinforcement	Change (%)
FRP=40×200 mm²	*F*=1.5 kN	Total deformation (m)	1.45e-07	1.46e-07	+0.69
		Equivalent stress (Pa)	6.95 e05	6.90 e05	−0.72
	F=2.0 kN	Total deformation (m)	1.93e-07	1.95e-07	+1.04
		Equivalent stress (Pa)	9.27 e05	9.22 e05	−0.54
	F=3.0 kN	Total deformation (m)	2.90e-07	2.92e-07	+0.69
		Equivalent stress (Pa)	1.39 e06	1.35 e06	−2.88
FRP=50×200 mm²	*F*=1.5 kN	Total deformation (m)	1.45e-07	1.47e-07	+1.38
		Equivalent stress (Pa)	6.95 e05	6.90 e05	−0.72
	F=2.0 kN	Total deformation (m)	1.93e-07	1.95e-07	+1.04
		Equivalent stress (Pa)	9.27 e05	9.20 e05	−0.76
	F=3.0 kN	Total deformation (m)	2.90e-07	2.92e-07	+0.69
		Equivalent stress (Pa)	1.39 e06	1.32 e06	−5.04
FRP=60×200 mm²	*F*=1.5 kN	Total deformation (m)	1.45e-07	1.46e-07	+0.69
		Equivalent stress (Pa)	6.95 e05	6.91 e05	−0.58
	F=2.0 kN	Total deformation (m)	1.93e-07	1.95e-07	+1.04
		Equivalent stress (Pa)	9.27 e05	9.24 e05	−0.32
	F=3.0 kN	Total deformation (m)	2.90e-07	2.92e-07	+0.69
		Equivalent stress (Pa)	1.39 e06	1.33 e06	−4.32

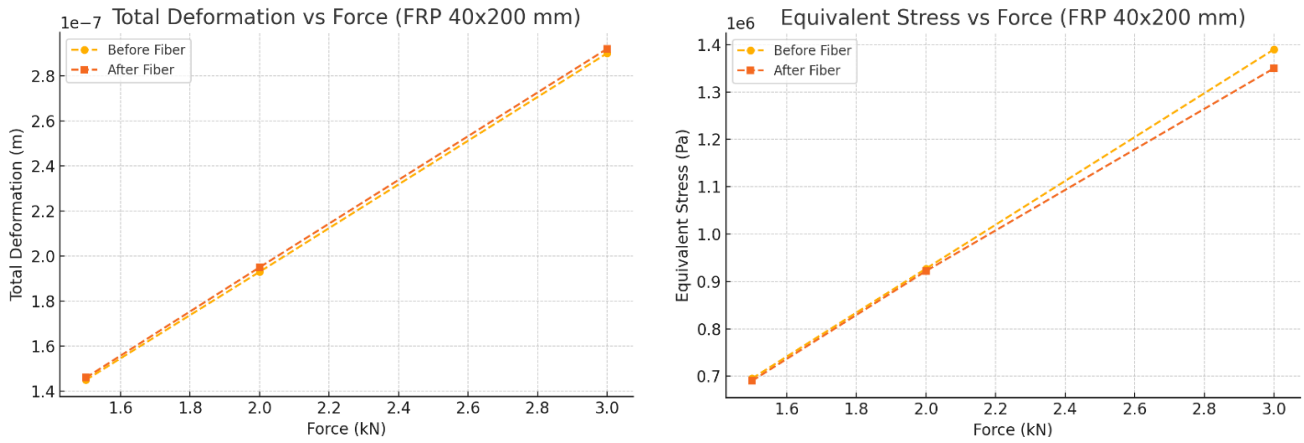

Fig. 17. Total deformation and equivalent stress graph (FRP=40×200 mm²).

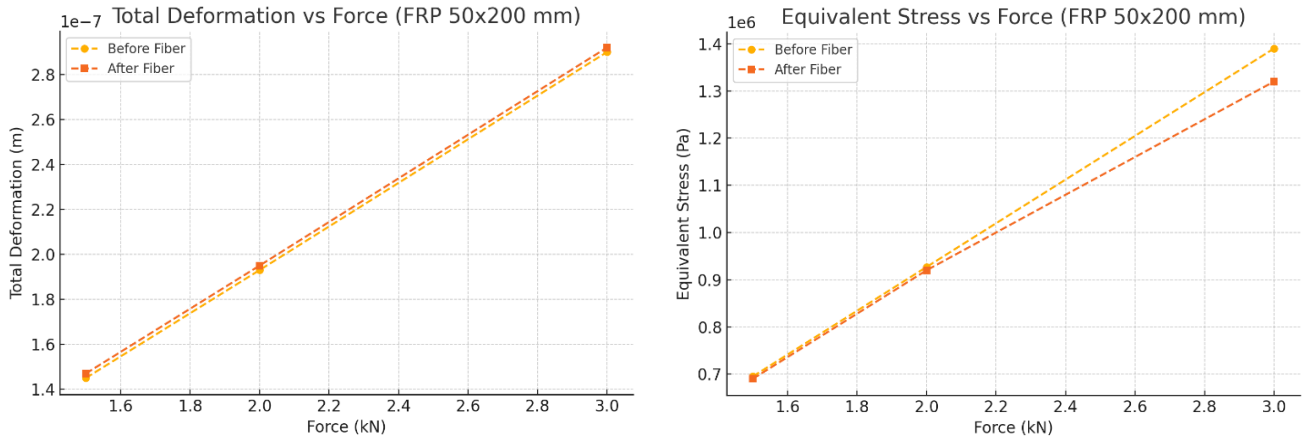

Fig. 18. Total deformation and equivalent stress graph (FRP=50×200 mm²).

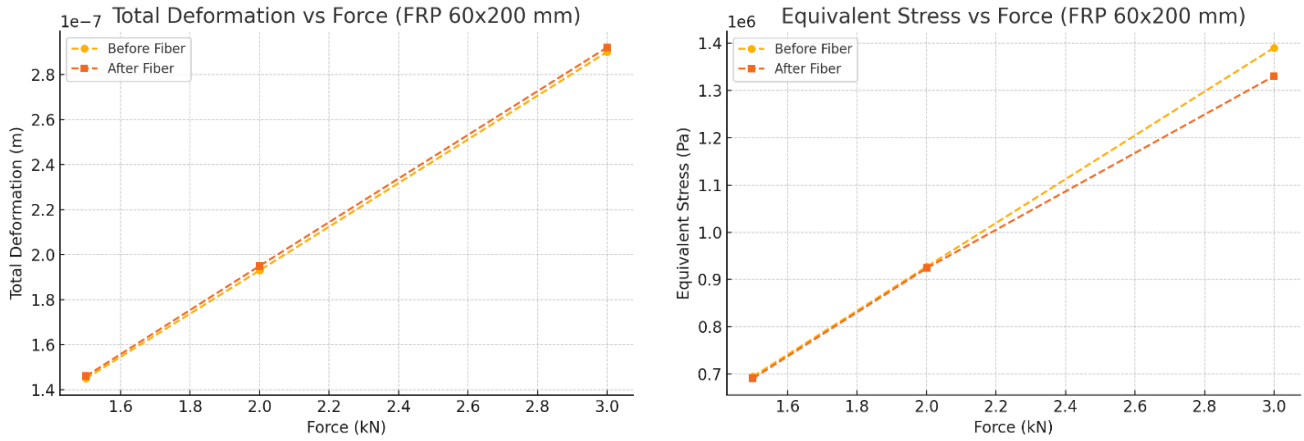

Fig. 19. Total deformation and equivalent stress graph (FRP=60×200 mm²).

Under forces of 1.5, 2.0, and 3.0 kN applied laterally, the unreinforced plate exhibited significant deformation and stress concentrations around the perforation. The stress distribution highlighted areas of high von Mises stress around the circular hole, reducing the load-bearing capacity of the plate. The addition of FRP material symmetrically around the hole significantly enhanced the mechanical performance of the plate. Compared to the unreinforced scenario, the reinforced plate showed reduced stress concentrations. This improvement was consistent across all loading conditions. The effective-ness of the reinforcement was evident from the comparison of deformation and stress distributions between the reinforced and unreinforced plates.

According to obtained results the FRP reinforcement mitigated stress concentrations and improved the plate's ability to distribute loads more evenly, enhancing structural integrity. The comparative analysis demonstrated that the FRP material contributed to a substantial reduction in von Mises stress, particularly under higher loads (3.0 kN). This indicates the potential of FRP reinforcements in extending the lifespan and reliability of perforated plates.

4. Conclusions

This study examined the effects of reinforcing a perforated steel plate with fiber-reinforced polymer (FRP) composites around the perforation to improve its structural performance. Critical mechanical parameters such as total deformation and equivalent stress (von Mises stress) under varying loading conditions were evaluated by finite element analysis (FEA) performed with ANSYS software.

This study demonstrates that reinforcing perforated steel plates with FRP significantly reduces stress concentration, thereby improving structural integrity. The findings provide valuable insights for engineers and designers in optimizing reinforcement strategies for practical applications in construction and industrial settings.

The results emphasize the importance of reinforcement in extending the service life of structural elements subjected to mechanical stress. By distributing loads more effectively, FRP materials reduce the risk of localized failure, ensuring more durable and reliable performance over time. This is particularly relevant for industries such as aerospace, automotive, and civil engineering, where lightweight yet strong materials are essential for efficient structural performance.

Future research could further explore experimental validation of the findings by conducting physical load tests on reinforced perforated plates. Moreover, studying the long-term durability of FRP reinforcements under dynamic and cyclic loading conditions will provide deeper insights into their practical applications. Investigations into alternative reinforcement configurations and fiber orientations could also enhance the effectiveness of strengthening techniques.

Acknowledgements

None declared.

Funding

The authors received no financial support for the research, authorship, and/or publication of this manuscript.

Conflict of Interest

The authors declared no potential conflicts of interest with respect to the research, authorship, and/or publication of this manuscript.

Author Contributions

All of the authors made substantial contributions to conception and design, or acquisition of data, or analysis and interpretation of data; were involved in drafting the manuscript or revising it critically for important intellectual content; and gave final approval of the version to be published.

Data Availability

The datasets created and/or analyzed during the current study are not publicly available, but are available from the corresponding author upon reasonable request.

REFERENCES

Abualigah L, Elaziz MA, Khasawneh AM, Alshinwan M, Ibrahim RA, Al-Qaness MA, Gandomi AH (2022). Meta-heuristic optimization algorithms for solving real-world mechanical engineering design problems: A comprehensive survey, applications, comparative analysis, and results. *Neural Computing and Applications*, 34, 1-30.

Baş S (2024). Use of seismic isolators in reinforced concrete structures and examination of seismic isolator types. *M.Sc. thesis*, Sakarya University of Applied Sciences, Sakarya, Türkiye.

Caştur N (2021). Analysis of industrial timber building elements and building examples used in today's architecture. *M.Sc. thesis*, Fatih Sultan Mehmet University, İstanbul, Türkiye.

Cheng B, Zhao J (2010). Strengthening of perforated plates under uniaxial compression: Buckling analysis. *Thin-Walled Structures*, 48, 905-914.

Demir E (2024). Experimental study on large deflections of perforated composite plates. *Journal of the Brazilian Society of Mechanical Sciences and Engineering*, 46(1), 5.

Demirel S (2023). Selection of building bearing systems with AHP-PROMETHEE method. *M.Sc. thesis*, Istanbul Kültür University, İstanbul, Türkiye.

Hou G, Huang X, Li Z, Cui Y (2025). Wear mechanisms of carbon fiber-reinforced resin matrix composite at extreme temperatures. *Polymer Composites*, 46(52), S874-S888.

Klazly MM, Bognár G (2020). CFD study for the flow behaviour of nanofluid flow over flat plate. *International Journal of Mechanics*, 14, 49-55.

Singh TG, Singh KD (2021). Design of perforated cold-formed steel hollow stub columns using direct strength method. *Thin-Walled Structures*, 168, 108265.

Sunar N, Uysal H (2024). Dynamic characteristics of CFRP-strengthened wooden beams: Experimental and numerical study. *Structural Engineering and Mechanics*, 89(3), 323-334.

Tarhan İH, Savalle N, Uysal H, Silva LCM, Lourenço PB (2025). Seismic capacity of unstrengthened and FRP-strengthened masonry arches: Tilting test and nonlinear numerical analysis. *Earthquake Engineering & Structural Dynamics*, 54, 1009-1027.

Yan S, Wu J, Chen J, Xiong Y, Mao Q, Zhang X (2022). Optimization design and analysis of honeycomb micro-perforated plate broadband sound absorber. *Applied Acoustics*, 186, 108487.

Yılmaz S, Vural N (2018). Usage possibilities of wood concrete composite system in architecture. In: *Proceedings of the 4th National Construction Congress and Exhibition "Innovative Approaches in the Construction Sector"*, Antalya, Türkiye, 315-328.

Yücesoy A (2021). Analysis of lateral and bending torsional buckling problems of structural members by semi-analytical methods. *Ph.D. thesis*, Kocaeli University, Kocaeli, Türkiye.

Zhou CW, Lainé JP, Ichchou M, Zine AM (2016). Numerical and experimental investigation on broadband wave propagation features in perforated plates. *Mechanical Systems and Signal Processing*, 75, 556-575.

Challenge Journal of Structural Mechanics

Research Article

Effect of elevated temperatures on mechanical properties of hydraulic lime-based mortar in historical structures

Ahmet Fazil Kara [a,*], Ferit Cakir [a], Metehan Calis [b]

[a] *Department of Civil Engineering, Gebze Technical University, 41400 Kocaeli, Türkiye*
[b] *Testing and Calibration Centre, Turkish Standards Institution, 34197 İstanbul, Türkiye*

ABSTRACT

Historic masonry structures are subjected to various negative effects from the time they are built. As a result, these structures suffer damage, leading to restoration and reinforcement efforts. Hydraulic lime-based mortars (HLMs), which are compatible with the nature of historic structures, are used in restoration and reinforcement. This study investigated the fire resistance of hydraulic lime-based mortars. Within the scope of this study, HLMs were prepared in accordance with restoration standards, and prism specimens were prepared with HLMs. These specimens were exposed to high temperatures ranging from 200 °C to 700 °C, and bending and compression tests were conducted on the specimens exposed to temperature. During the elevated temperature tests (ETTs), a total of 27 specimens were prepared, including three test specimens, one temperature monitoring specimen for each temperature, and three reference specimens. While the reference specimens were tested at room temperature, the other specimens were kept until they reached room temperature after the ETTs were completed and then tested under the same conditions as the reference specimens. No tests were performed on the temperature monitoring specimens, and these specimens were only used to monitor the temperatures inside the specimens with thermocouples placed inside. As a result of the experimental studies and evaluations, it was determined that the HLMs began to lose their mechanical properties with increasing temperature, but even after 700 °C, they still exhibited mechanical properties observed in low-grade mortars.

ARTICLE INFO

Article history:
Received – April 8, 2025
Revision requested – May 6, 2025
Revision received – May 23, 2025
Accepted – June 2, 2025

Keywords:
Hydraulic lime-based mortar
Elevated temperature test
Mechanical properties
Compression strength
Flexural strength

Citation: Kara AF, Cakir F, Calis M (2025). Effect of elevated temperatures on mechanical properties of hydraulic lime-based mortar in historical structures. *Challenge Journal of Structural Mechanics*, 11(4), 184–200.

1. Introduction

Historic masonry structures are subjected to a multitude of adverse conditions, enduring ravages of time, natural disasters, and human interventions. In addition to their behavior against atmospheric conditions and aging, historic mortars are also exposed to harsh conditions during natural disasters, such as earthquakes, landslides, air pollution, extreme temperatures, floods, and fires. Fire poses a particularly formidable threat to these architectural treasures, capable of erasing centuries of history in hours and causing irreversible damage. In addition to architectural and cultural value loss, fires can lead to costly and destructive situations in historical structures. The performance of structural elements during and after a fire is crucial for the future of a building. In particular, the thermal behavior of construction materials during and after a fire and the changes in their physical and mechanical properties are critical for structural performance. The mortar in joint areas, considered the weakest link in the chain, is the construction material that most significantly affects the fire performance of historical structures. It is known that even the smallest weaknesses occurring at the connection points can lead to ir-

* *Corresponding author*. E-mail address: akara2019@gtu.edu.tr (A. F. Kara)
ISSN: 2149-8024 / DOI: https://doi.org/10.20528/cjsmec.2025.04.002

reversible damage throughout the entire structure. Although the composition of mortar varies depending on the era, historical mortars primarily consist of lime-based materials, including air lime mortars, lime-pozzolan mortars, natural hydraulic lime mortars, and ternary mortars.

Although the fire resistance and physical and mechanical performance of hydraulic lime-based mortars HLM after a fire are significant topics, studies conducted in the literature are quite limited. Studies in the literature have primarily focused on cement-based mortars. For example, Neto et al. (2022) investigated the impact of post-fire curing on the mechanical behavior of cement-lime based masonry mortars, which are often overlooked in contemporary structures. Three mortar mixes were subjected to fire tests and cured at different post-fire ages. Mechanical tests revealed that longer post-fire curing led to reduced mechanical properties and increased deformability, particularly in mortars with higher lime content. The mortars exhibited progressive deterioration and became more ductile over time during the post-fire curing. Additionally, a theoretical model with correlations accurately predicted the post-fire mechanical behavior of masonry mortars. Bamonte et al. (2021) focused on the behavior of three bed-fixing cement-lime based mortars at high temperatures (up to 900 °C) to understand their mechanical properties and thermal diffusivity. This study aimed to expand knowledge on this subject and develop stress-strain relationships for potential use in masonry structure design. Their study emphasized that while the mechanical decay at high temperatures is similar to that of ordinary concrete, they exhibit higher mass loss, lower thermal diffusivity, and greater ductility. This led to the calibration of an analytical stress-strain law for compression, which considered the specific characteristics of the mortars.

Pachta et al. (2021) conducted a study on the use of brick residues in historic mortars to enhance pozzolanicity and resistance to humidity, as well as to assess their performance at elevated temperatures. Three mortar series were tested: lime, lime with natural pozzolan, and lime with natural pozzolan and brick dust. Physico-mechanical properties were tested at 28 and 90 days, and mortars were exposed to temperatures ranging from 200 °C to 1000 °C. The study suggested that the 90-day age is more representative, and the inclusion of crushed brick and brick dust improves the structural integrity at extreme temperatures. Rais et al. (2019) discussed how high temperatures affect the fresh and aged strengths, as well as the microstructure properties of fly ash mortars. Various blends were tested, and after exposure to temperatures ranging from 100 °C to 500 °C, compression strengths was measured and compared between blended and plain mortars. Mortars with 10% fly ash exhibited superior performance at 500 °C. The proposed model accurately predicted the aged strength of blended mortar after heating, offering potential benefits for concrete construction and sustainability. Pachta et al. (2018) examined the impact of elevated temperatures on lime-based mortars used in historical restoration. Mortar specimens were exposed to temperatures from 200 °C to 1000 °C, and their properties were tested before and after exposure. The results indicated that lime-based mortars generally retain their structure and characteristics after exposure to high temperatures, with the lime-pozzolan matrix displaying particularly high resistance. Zhang et al. (2018) investigated the impact of heat treatment on fly ash (FA) cement mortar, focusing on color and thermal conductivity changes. Different FA replacement percentages (10%, 20%, and 40%) were examined across 45 samples exposed to temperatures ranging from room temperature to 800 °C. The study emphasized a critical temperature range (400–600 °C) causing pH reduction due to carbonization and calcium hydroxide decomposition, shortening mortar lifespan. The thermal conductivity decreased at higher temperatures, which correlated with the density ratio. The findings suggest an optimal FA percentage for improved mortar properties heat exposure.

Horszczaruk et al. (2017) investigated the impact of nanosilica on cement mortars containing quartz, magnetite, and barite aggregates exposed to high temperatures (200 °C to 800 °C). The mortars were modified with nanosilica in various proportions. The findings revealed that an optimal nanosilica content enhances thermal resistance and prevents crack extension, particularly in mortars with quartz and magnetite aggregates. However, mortars containing barite aggregates tend to crack and exhibit spalling owing to the lower thermal resistance of the aggregate. Pan et al. (2017) examined the high-temperature performance of cementitious materials containing fine glass powder (GP) as a partial replacement for ordinary Portland cement. Various mixtures were prepared using different proportions of GP. Compressive strength tests were conducted at temperatures ranging from 20 °C to 800 °C, alongside X-ray diffraction (XRD), scanning electron microscopy (SEM), and thermal strain tests on corresponding pastes. The results indicate two distinct temperature ranges for the effects of GP on the mortar strength. Below 500 °C, mortars with 20% GP showed superior performance because of reduced calcium hydroxide content. Between 500 °C and 800 °C, GP mortars exhibited higher strength loss, attributed to greater thermal incompatibility arising from paste shrinkage and sand particle expansion.

Pachta et al. (2018) and Bamonte et al. (2021) referred that the chemical composition and hydration products, carbonation and thermal stability, microstructural porosity and permeability, thermal expansion and ductility factors collectively explain why high-performance concrete (HLM) retains residual mechanical properties even at 700 °C, whereas cementitious mortars undergo rapid deterioration beyond 400 °C. İsafça et al. (2022) investigated the effect of elevated temperature on polypropylene fiber reinforced Khorasan mortar. Aruntaş et al. (2021) investigated lime usage in cement paste and mortar with different proportion of lime at room temperature.

Although studies have been conducted on the fire resistance or post-fire mechanical properties of cement-based mortars or mortars reinforced with other materials as a result of literature research, studies on HLMs are quite scarce and insufficient. Therefore, in this study, the effects of fire exposure at different levels on the mechanical strength of HLMs were investigated. As part of the

investigation, the HLM was formulated following restoration standards, and prism-shaped specimens were prepared with HLMs. Subsequently, the specimens were exposed to elevated temperatures ranging from 200 °C to 700 °C. This was followed by a series of bending and compression tests. It is believed that the conducted research and experimental studies will fill this gap in the literature and present an original study.

2. Materials and Method

In this study, the fire resistance of HLMs is investigated. Within the scope of this research, these mortars were prepared according to restoration standards, and prism samples were created with HLMs. These samples were then subjected to bending and compression tests at temperatures ranging from 200 °C to 700 °C after being exposure to high temperatures. A total of 27 samples were included in the high-temperature tests, with three experimental samples, one temperature-monitoring sample, and three reference samples for each temperature. The reference samples were tested at room temperature, whereas the other samples were held at room temperature after completing the fire test and then tested under the same conditions as the reference samples. No tests were conducted on the temperature-monitoring samples; they were only used to monitor the internal temperatures of the samples using the embedded thermocouples that differs from past studies. In this study, all steps were performed according to the flowchart (Fig. 1).

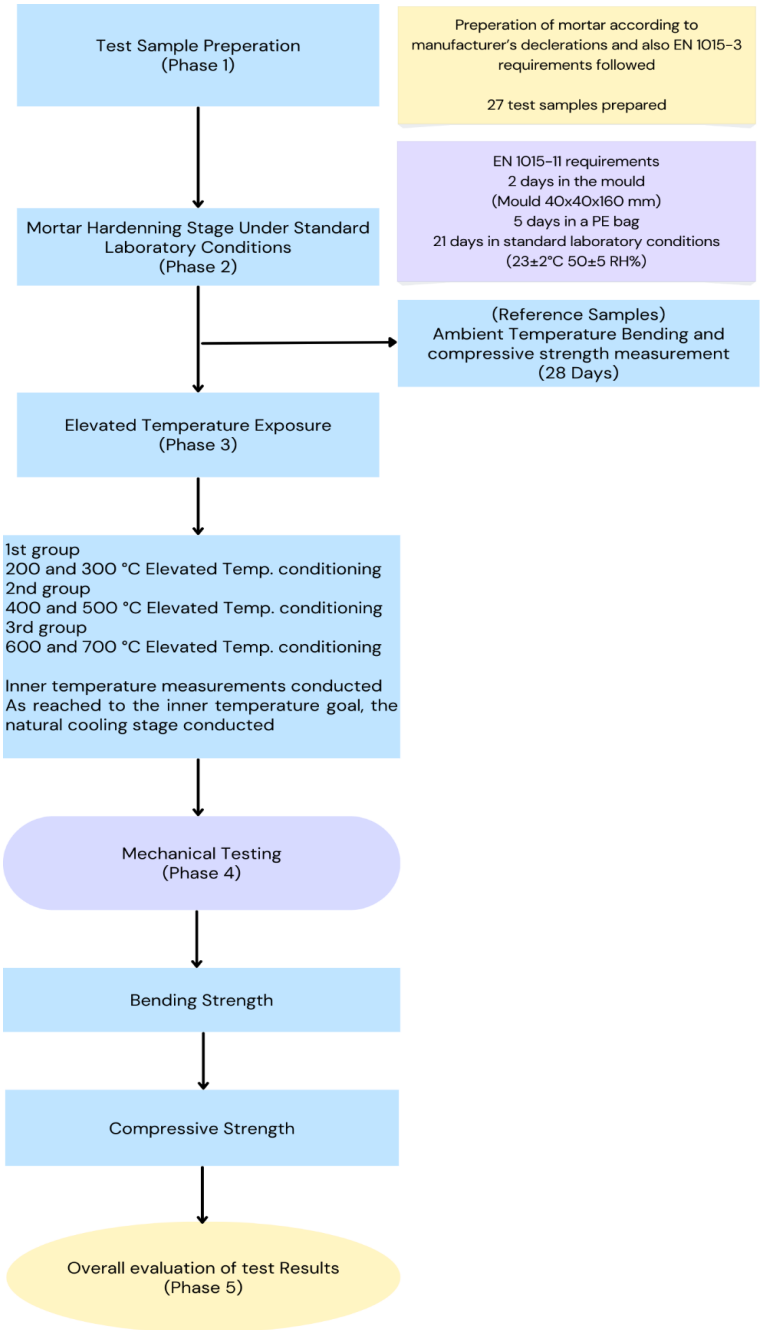

Fig. 1. Flowchart for the study.

2.1. Hydraulic lime-based mortar

Mortar serves as an adhesive substance that binds stones or bricks and plays a crucial role in masonry construction. It functions to fill the spaces between building blocks (mortar joints), thereby enhancing structural integrity. Additionally, mortar provides resistance to air and water infiltration, which bolsters the durability of masonry structures. The key properties of mortars include their workability, cohesiveness, resistance to external forces, and ease of spreading. The strength and durability of masonry structures are significantly influenced by the physical properties of the mortar. The bond strength and binding characteristics of mortar play a crucial role in determining the overall performance of a building. A well-formulated mortar with a strong bond strength enhances the structural integrity of the masonry, ensuring stability and resilience against various external forces and environmental factors. Consequently, understanding and optimizing these mortar properties are essential for ensuring the longevity and effectiveness of masonry structures. Cakir (2011) investigated the required volume of mortar varies based on the type of masonry, typically ranging from 0 to 20 percent of the total volume. Despite its relatively small volume, mortar plays a crucial role in masonry structures. The initial state of the mortar was plastic, but it rapidly commenced a hardening process. Mortar is typically produced by blending sand, lime, cement, and water. Previously, traditional mortar was composed of mud, clay, and lime. Lime mortars, among the earliest variants, trace back to Babylonian origins, although Egyptians advanced mortar technology by incorporating lime and gypsum to construct pyramids. Historical masonry structures commonly use HLM. However, Sánchez (2007) described Romans revolutionized mortar production by introducing cement, which subsequently became the predominant material for mortar applications.

HLMs are most commonly used to repair and restore historical masonry structures, and are special mortars prepared for historical structures without cement. It provides breathability and high water vapor permeability. It is compatible with historical structures and allows the production of mortars with different properties. Natural hydraulic lime (NHL) acquires its characteristics by calcining argillaceous or siliceous limestones, followed by pulverization via slaking with or without grinding. HLMs solidify via a dual process involving hydration, which forms a calcium-silicate-hydrate structure, and carbonation, which occurs as calcium hydroxide reacts with carbon dioxide in the air. Bompa and Elghazouli (2020) investigated commercial binders are categorized based on their hydraulicity levels, which correlate with the strength development. Natural hydraulic limes are categorized based on their compressive strengths. For example, the compressive strengths of the NHL2, NHL3.5, and NHL5 mortars were 2.0, 3.5, and 5.0 MPa, respectively.

In the scope of this study, a Teknorep 520 mortar (TEKNO Construction Chemical, Turkey), specially developed for historical buildings in accordance with the TS EN 998-2:2011 “Specification for mortar for masonry - Part 2: Masonry mortar” standard, was used utilizing NHL5 class natural hydraulic lime. The technical data for Teknorep 520 are listed in Table 1.

Table 1. Technical data of Teknorep 520.

General Information	
Material structure	Special blend with natural hydraulic lime based and adjusted gradients
Cement content	0%
Appearance	Off-white and white coffee
Shell life	12 months in dry place in unopened packaging
Package	20 kg kraft bag
Application Information	
Implementation process	Min. 30 minutes
Application ground temperature	(+5 °C)–(+35 °C)
Grain size	< 2 mm
Application thickness	Each storey 1–5 cm
Performance Information	
Flexural strength	>2.0 N/mm^2
Compressive strength (EN 1015-11)	10–15 N/mm^2 (M10 Class)
Water vapor permeability (EN 1745)	$\mu < 35$
Capillary water absorption (EN 1015-18)	0.2 kg m^{-2} h$^{-0,5}$
Bond strength	> 0.15 N/mm^2
Reaction to fire	A1

2.2. Preparation of hydraulic lime-based mortar specimens

To prepare the specimens, Teknorep520 was mixed at 20/6 water content ratio in the laboratory. Subsequently, the mixed mortar was poured into molds measuring 40 × 40 × 160 mm, according to the specifications outlined in EN 1015-11. These specimens were then enclosed in polyethylene bags to maintain a relative humidity of 95% ± 5, as to the guidelines provided in EN 1015-11 (Fig. 2). After a period of five days, the specimens were extracted from the molds and kept in polyethylene bags for an additional two days, for a 7-day duration. Subsequently this, the specimens were transferred to laboratory conditions of 65% ± 5% relative humidity and 20 °C for further testing.

Fig. 2. Test specimens.

3. Elevated Temperature Tests (ETTs)

In this study, the experimental studies took place at the Construction Materials, Fire and Acoustic Laboratory of the Turkish Standards Institution (TSE) in İstanbul, Türkiye. The specimens were subjected to a designated constant temperature using the ISO 834-1 temperature–time curve. A specialized furnace powered by natural gas burners was to achieve these temperatures. To adhere to the EN 1363-1 standard and prevent direct flame contact, the specimens were positioned 750 mm away from the furnace burner. Two-plate K-type thermocouples were deployed throughout the tests to regulate the furnace temperature and positioned 100 mm from the specimens, following the guidelines outlined in EN 1363-1. Additionally, a K-type Inconel thermocouple was utilized to accurately gauge the temperature of the specimens (Fig. 3). This controlled specimen, which is distinct from those used for mechanical property evaluation, served solely to monitor the temperature levels.

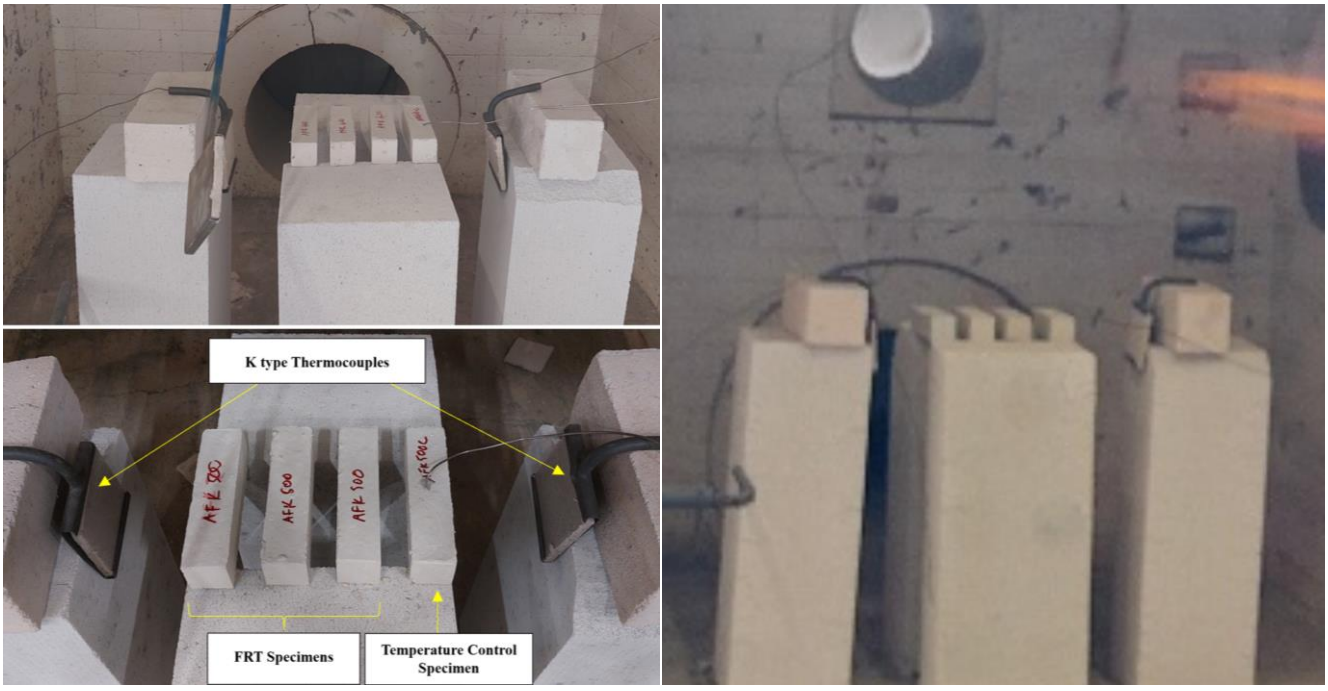

Fig. 3. ETT system.

This study conducted six ETTs spanning temperatures ranging from 200 °C to 700 °C in increments of 100 °C. For each test, four specimens were used, with one designated for measuring the mortar temperature and the remaining three for assessing the mechanical properties. Upon reaching the target temperature for each specimen, the furnace cover was removed, and both the furnace and specimen were allowed to cool until below 100 °C, with the cooling phases meticulously recorded. The standard temperature-time curve obtained from the thermocouples is shown in Fig. 4, and the temperature profiles for elevated conditions are depicted in Figs. 5–10.

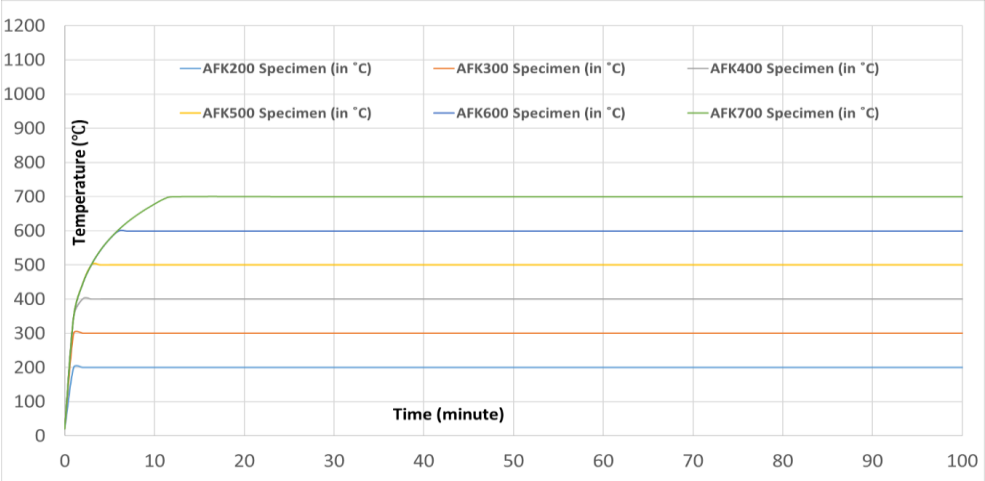

Fig. 4. Standard temperature-time curve (ISO 834).

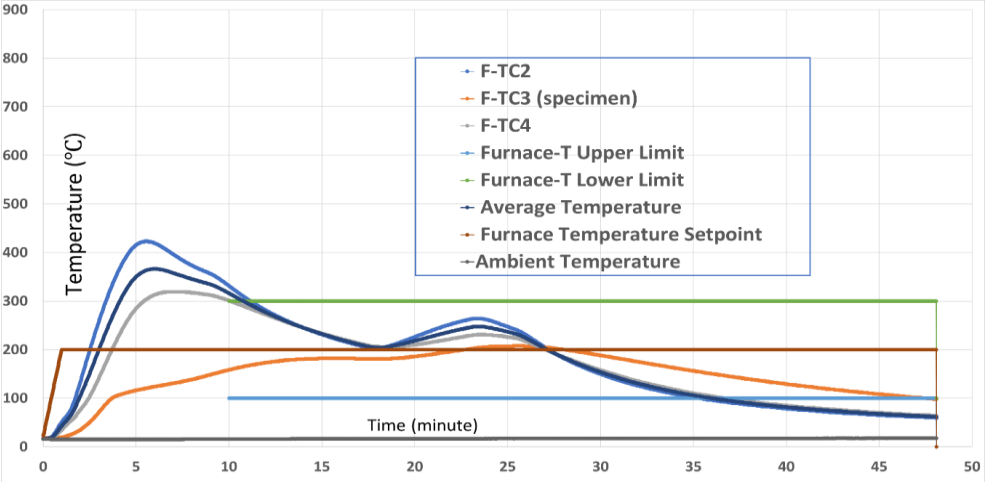

Fig. 5. Time-temperature exposure curve for 200 °C test specimen.

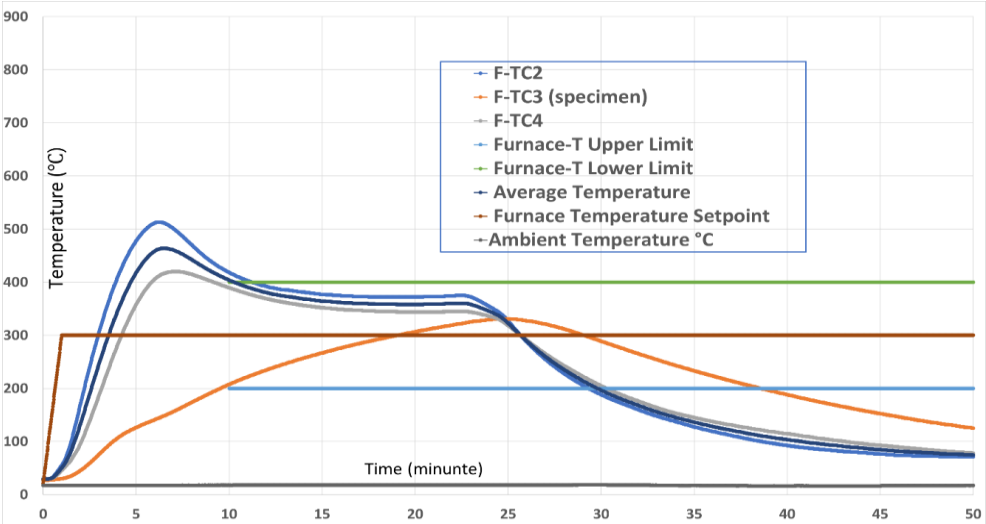

Fig. 6. Time-temperature exposure curve for 300 °C test specimen.

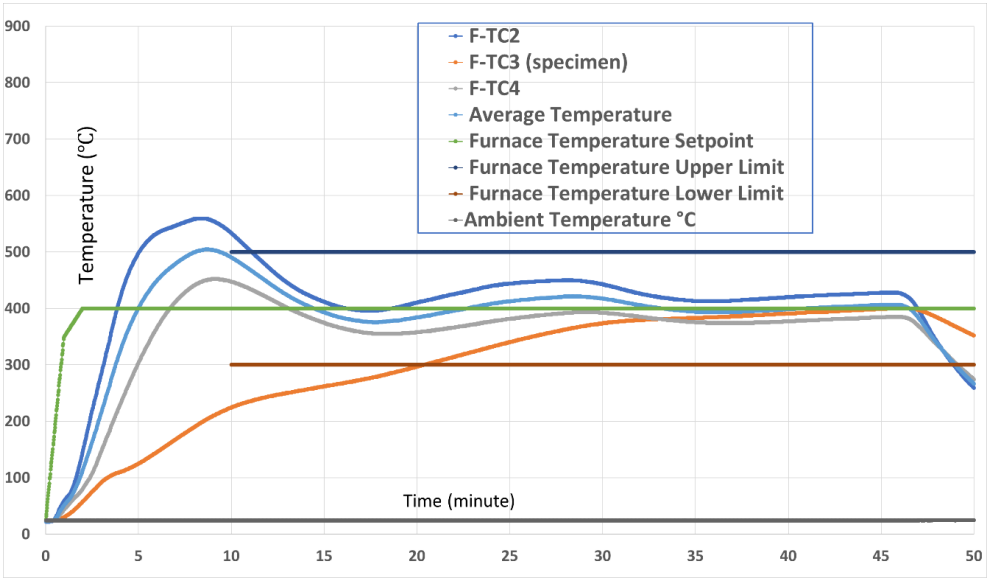

Fig. 7. Time-temperature exposure curve for 400 °C test specimen.

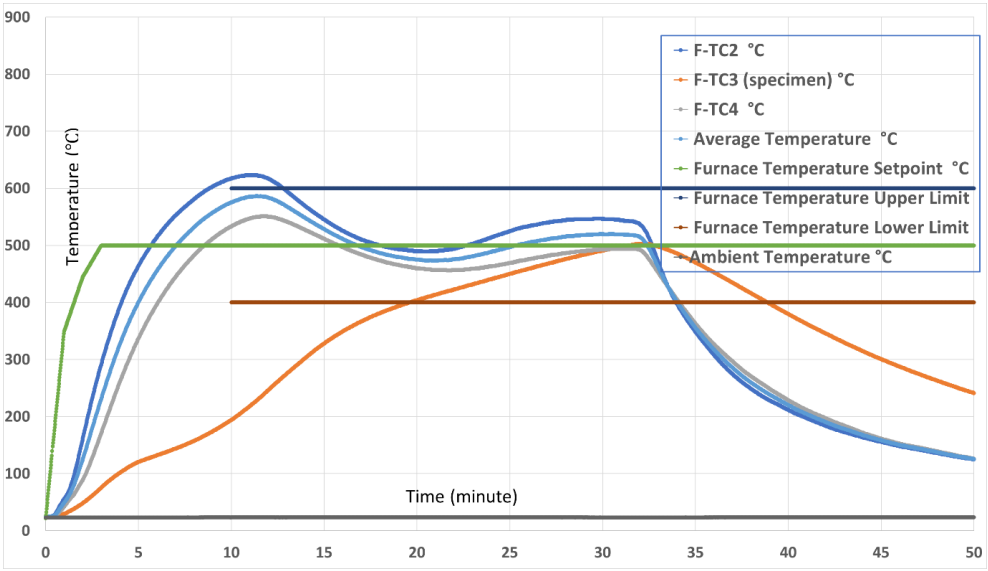

Fig. 8. Time-temperature exposure curve for 500 °C test specimen.

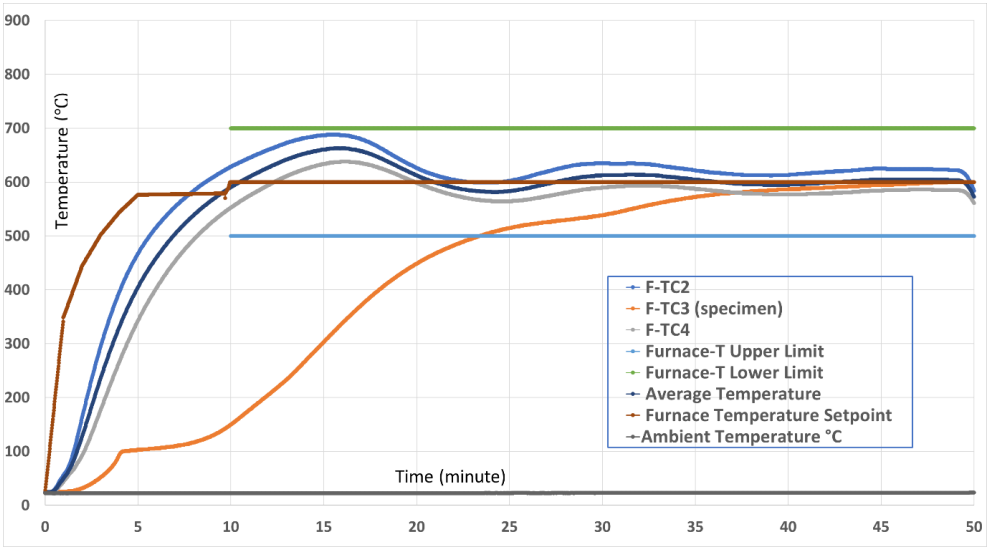

Fig. 9. Time-temperature exposure curve for 600 °C test specimen.

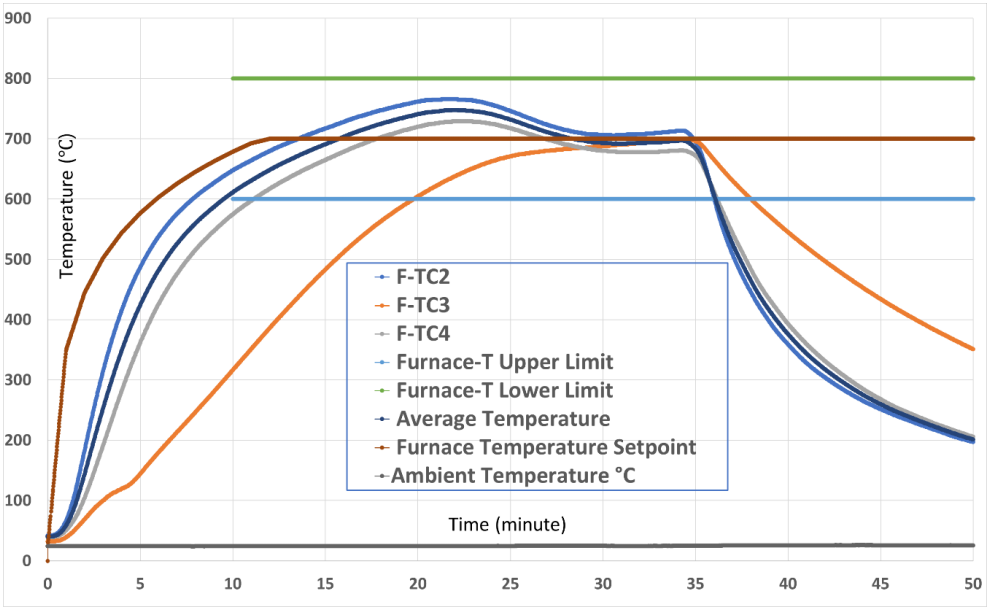

Fig. 10. Time-temperature exposure curve for 700 °C test specimen.

4. Mechanical Tests After ETTs

After the ETTs were completed, subsequent mechanical assessments were conducted to evaluate the structural integrity of the specimens under varying temperature conditions. Both bending and compression tests were performed to comprehensively analyze the mechanical properties following EN 1015-11. For each temperature increment tested during the ETTs, the specimens underwent three-point bending tests (Fig. 11) to assess their flexural strength and stiffness. The specimens were subjected to controlled loading until failure or until a predefined displacement limit was reached. Bending tests provide crucial insights into the ability of a material to withstand bending forces, which are essential for assessing its performance in real-world applications.

In addition to the bending tests, compression tests were conducted on separate specimens exposed to each temperature level during ETTs (Fig. 12). The specimen mechanical tests were performed 1-day after ETTs in order to be sure cooled to room temperature. Compression tests involve the application of axial loads to specimens to determine their compressive strength and deformation behavior. These tests help to understand how the material responds to compressive forces, which is vital for evaluating its structural stability and load-bearing capacity.

5. Results and Discussion

In this section, the findings of the study are presented and engaged in a comprehensive discussion to interpret the results. Additionally, the findings are contextualized within relevant literature and theoretical frameworks, fostering a perspective that enriches the discourse surrounding the findings.

5.1. Flexural strength

The flexural strength exhibited a distinct pattern with an increase in temperature. At 200 °C, the flexural strength decreased to approximately 70% of the ambient level, followed by a gradual decline of approximately 10% per 100 °C until reaching 700 °C. Ultimately, the flexural strength to a mere 20% of the ambient level at the highest temperature point. This gradual decrease underscores the susceptibility of the material to thermal degradation over prolonged exposure to elevated temperatures (Figs. 13–19).

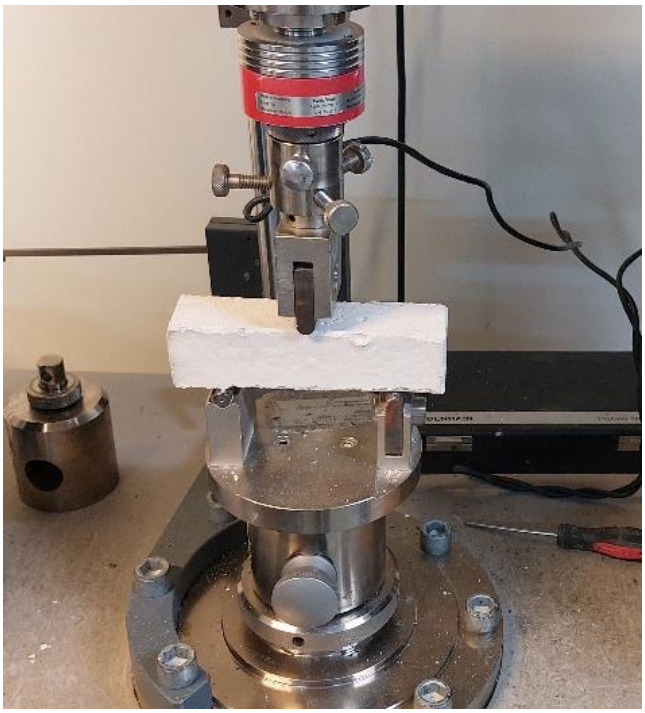

Fig. 11. Three-point bending test on the specimens.

Fig. 12. Compression test on the specimens.

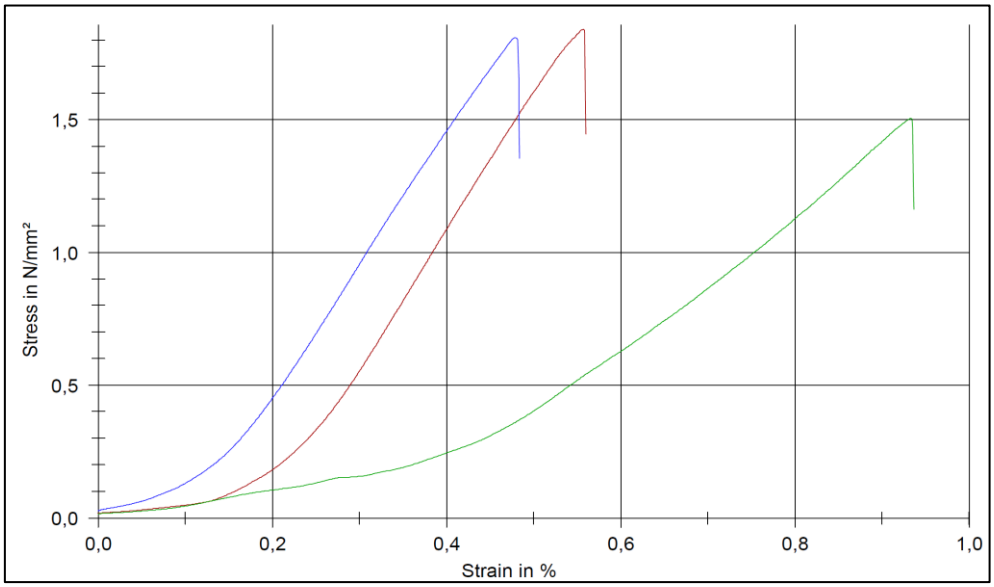

Fig. 13. The flexural strength at 20 °C.

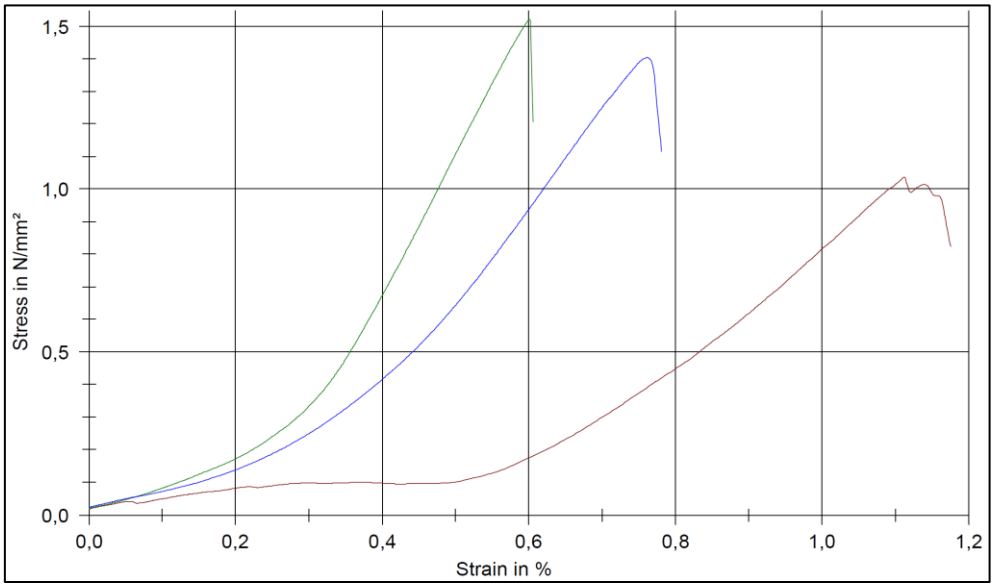

Fig. 14. The flexural strength at 200 °C.

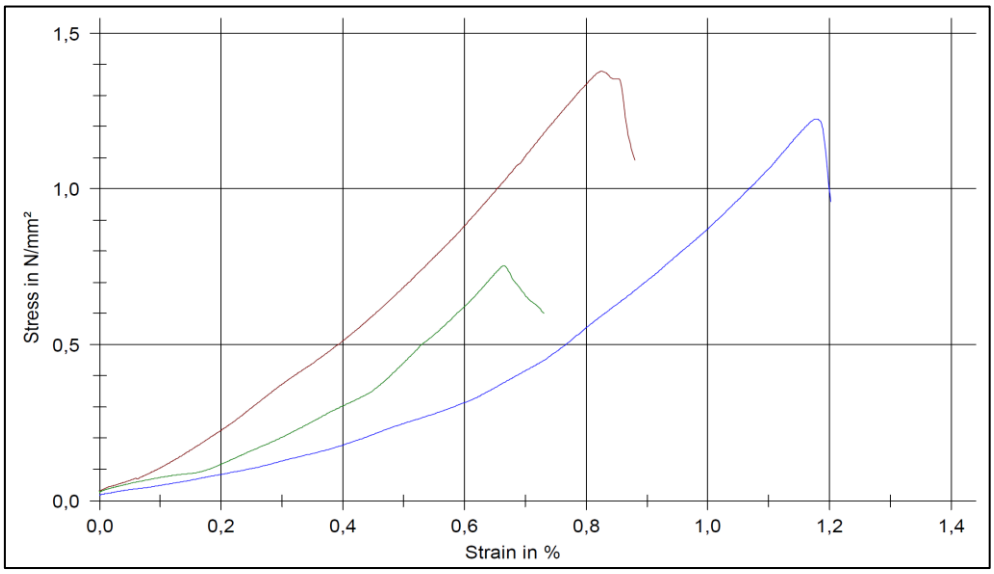

Fig. 15. The flexural strength at 300 °C.

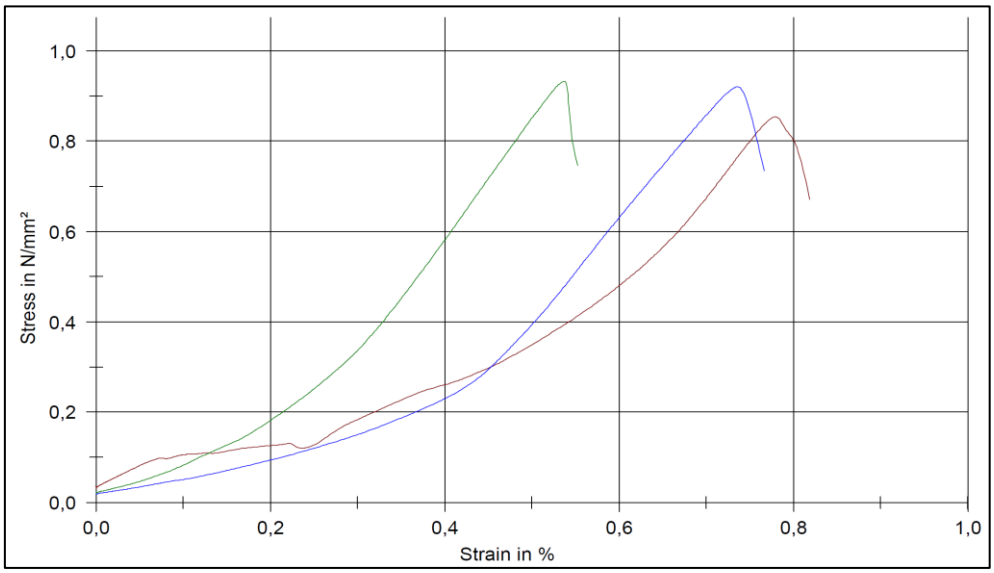

Fig. 16. The flexural strength at 400 °C.

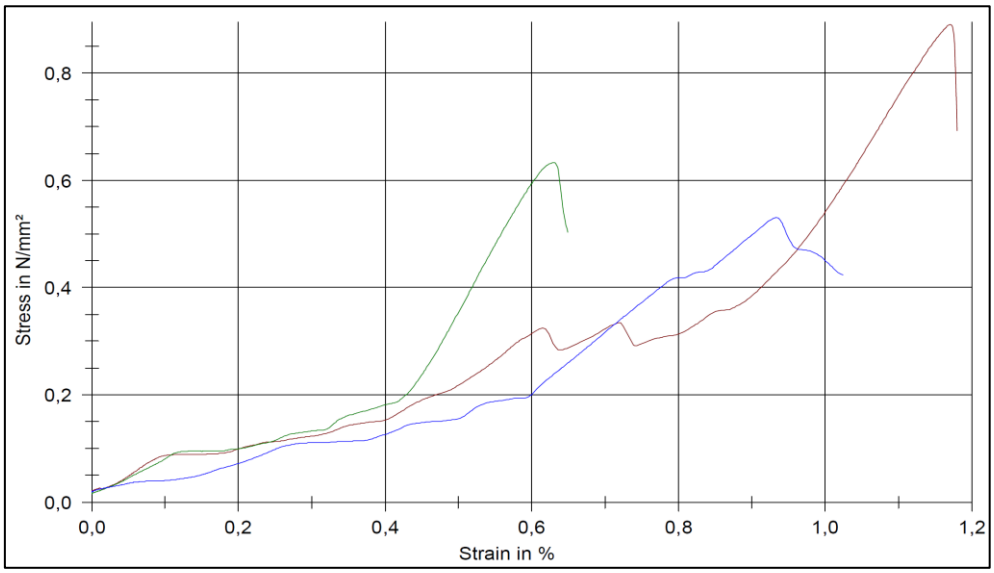

Fig. 17. The flexural strength at 500 °C.

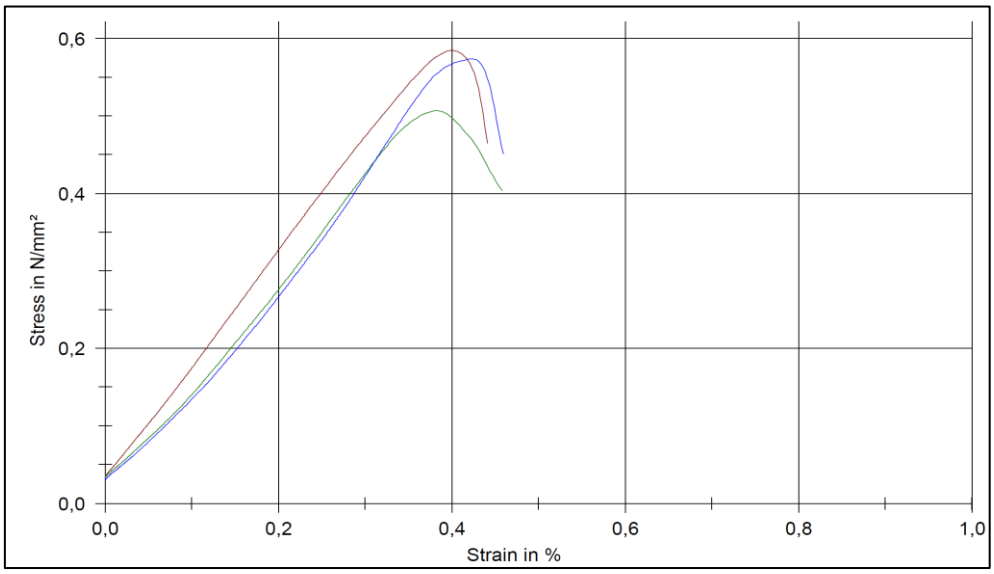

Fig. 18. The flexural strength at 600 °C.

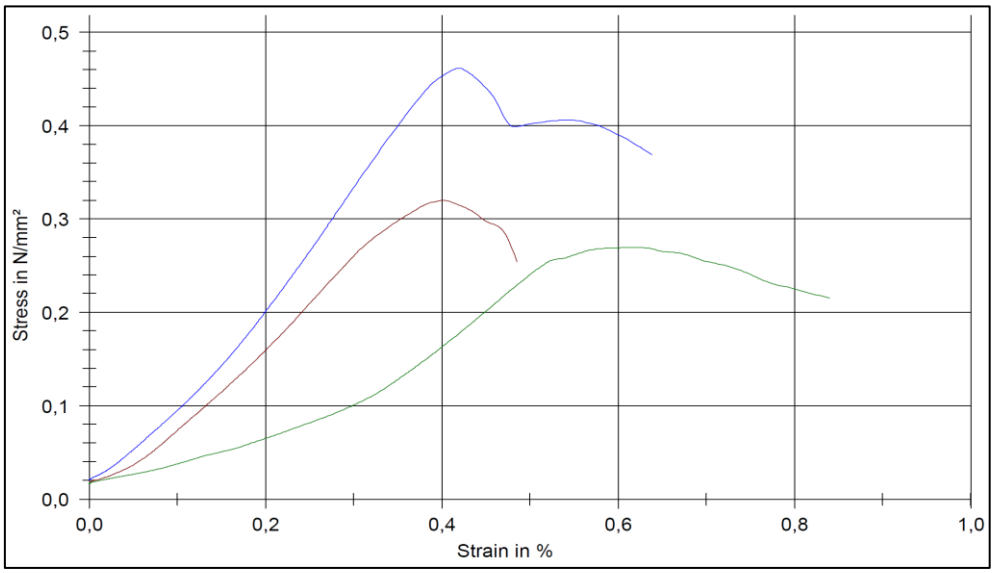

Fig. 19. The flexural strength at 700 °C.

Table 2 presents the results of the flexural tests conducted on HLM specimens subjected to varying temperatures. As observed from the data, there was a clear trend in the flexural strength of the mortar as the temperature increased. At lower temperatures (20 °C), the control specimens exhibited the highest flexural strength, gradually decreased with increasing temperature rises. This decline became more pronounced at higher temperatures, with a significant reduction observed at 400 °C and above. The average flexural strength across all the specimens followed a similar pattern, indicating a consistent response of the mortar to thermal exposure. These findings suggest that the HLMs experienced a decline in flexural strength as they underwent thermal stress, which has implications for their suitability for applications subjected to elevated temperatures (Table 2 and Fig. 20). In a similar manner, Pachta et al. (2018) concluded that the flexural strength of the lime-based mortars gradually decreases up to 800 °C, and at 1000 °C, it is minimized. Pachta and Stefanidou (2021) observed the flexural strengths of the lime- and cement-based mortars were reduced around 85–90% at 1000 °C.

Table 3 presents the energy absorption values obtained from the flexural tests conducted on HLM specimens exposed to varying temperatures. Flexural tests were performed to assess their ability to dissipate energy under different thermal conditions, providing insights into their structural integrity and performance. At temperatures ranging from 20 °C to 700 °C, the specimens exhibited varying levels of energy absorption, indicating a response to thermal stress of the material. Notably, as the temperature increased, discernible fluctuations were observed in the energy absorption values across the specimens. This decline in energy absorption could be attributed to the thermal degradation of HLMs, resulting in alterations to their microstructure and mechanical properties. Such changes might lead to compromised structural performance and durability, particularly under elevated-temperature conditions.

Table 2. Data obtained from flexural test results in N/mm² (MPa).

Specimen	Control (20 °C)	200 °C	300 °C	400 °C	500 °C	600 °C	700 °C
1	1.840	1.040	1.380	0.850	0.890	0.580	0.320
2	1.810	1.520	0.750	0.930	0.630	0.510	0.270
3	1.740	1.400	1.220	0.920	0.530	0.570	0.460
Average	1.797	1.320	1.117	0.900	0.683	0.553	0.350

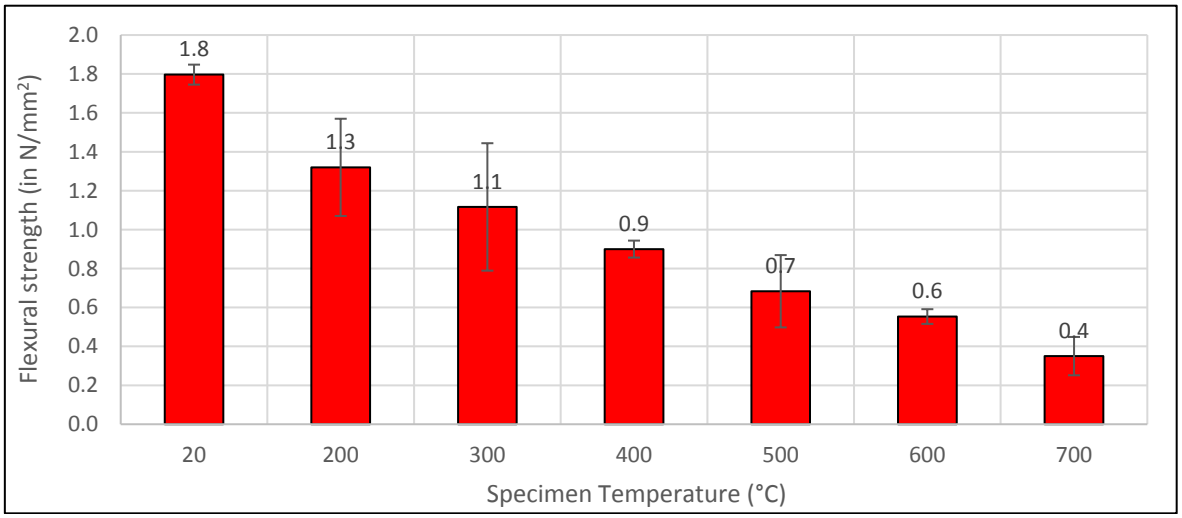

Fig. 20. Summary of flexural strength test results.

Table 3. Energy absorption of the specimens (Joule).

Specimen	Control (20 °C)	200 °C	300 °C	400 °C	500 °C	600 °C	700 °C
1	0.2406	0.3223	0.5590	0.2078	0.1467	0.1527	0.1835
2	0.4347	0.4154	0.2402	0.2564	0.3593	0.1458	0.0820
3	0.4865	0.4057	0.5290	0.2791	0.2291	0.1391	0.1353
Average	0.3873	0.3811	0.4427	0.2478	0.2450	0.1459	0.1336

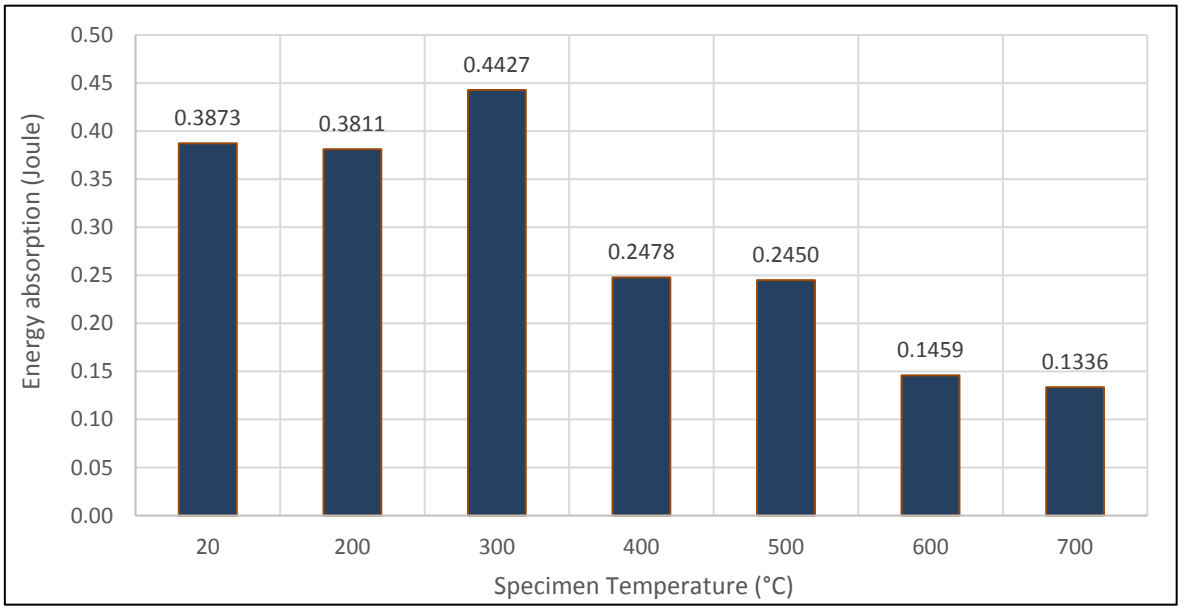

Fig. 21. Summary of energy absorption capacities.

5.2. Compression strength

Similarly, compression strength analysis revealed notable trends across various temperature ranges. Initially, up to 300 °C, the compressive strength remained relatively constant. However, a significant decrease was observed at 400 °C, where the strength decreased to 60% compared to ambient temperature conditions. This trend continued as temperature increased, with compression strength reaching a mere 30% of ambient levels at 700 °C. These findings suggest a critical temperature threshold, beyond which the structural integrity of the material is significantly compromised (Figs. 22–28).

In this study, the results showed that at lower temperatures (between 20 °C and 300 °C), the mortar generally exhibited higher compressive strength, indicating its structural integrity and stability under typical environmental conditions. However, as the temperature exceeded 300 °C, a significant reduction in compressive strength was observed in all specimens. This decline became particularly pronounced at temperatures exceeding 500 °C, indicating a critical threshold which the mechanical properties of the material were significantly compromised (Table 4 and Fig. 29). With an increase in temperature, a decrease in the mechanical properties and structural integrity of mortar and stones is supported in the literature. For example, Neto et al. (2022) reported that the deformability of masonry mortars increased significantly as the post-fire curing time and lime content of the mixture increased. Mortars with elevated lime content and extended post-fire curing periods displayed a more pliable nature. Karahan (2010) resulted that there is a significant decrease in compressive strength compared to the strength of the control reference mortar when temperature rise from 400 to 1000 °C. Bamonte et al. (2021) emphasized that for M15 class mortar, there is a slight increase in compressive strength at 200 °C with an increase. However, it is noted that as the temperature continued to increase, the compressive strength gradually decreased.

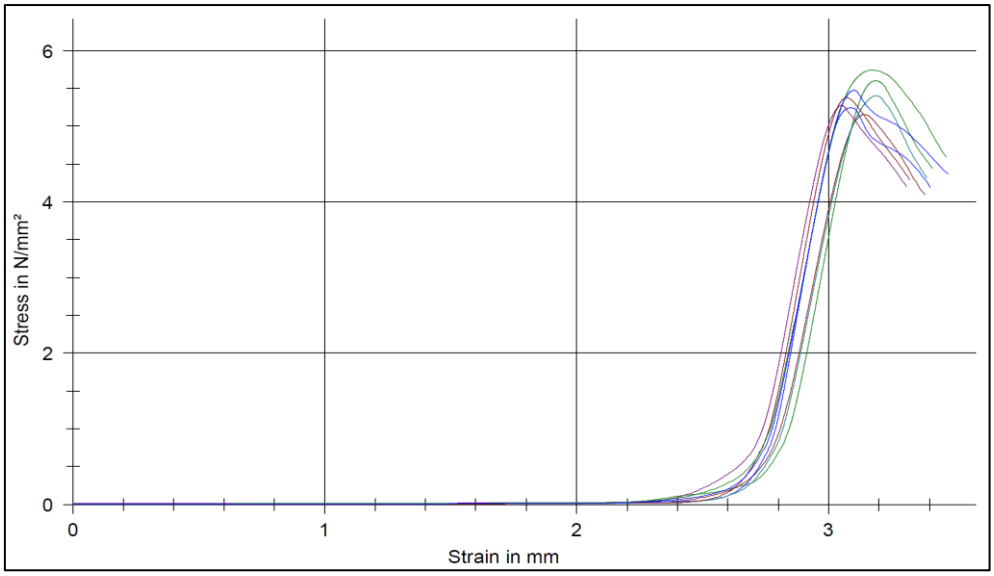

Fig. 22. The compressive strength at 20 °C.

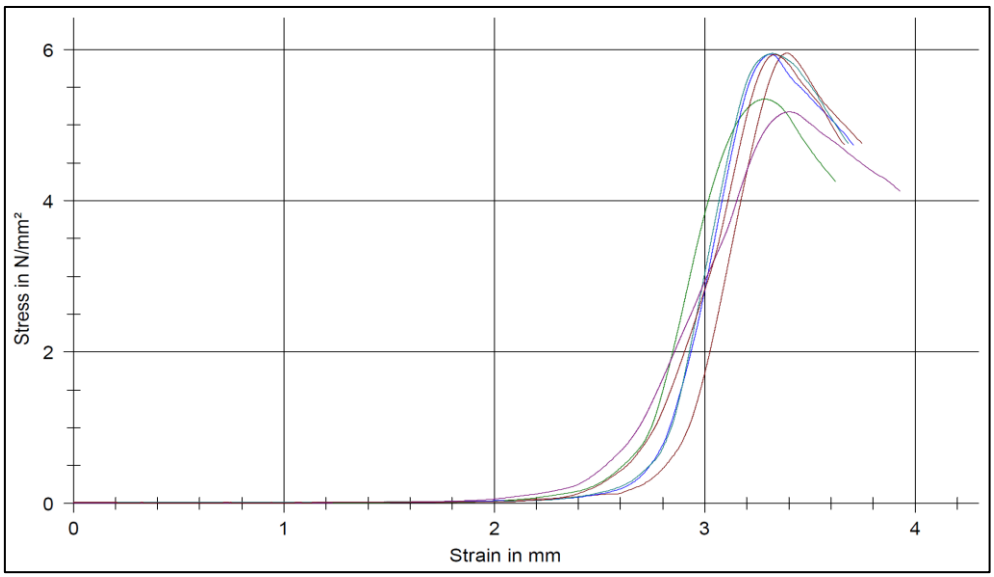

Fig. 23. The compressive strength at 200 °C.

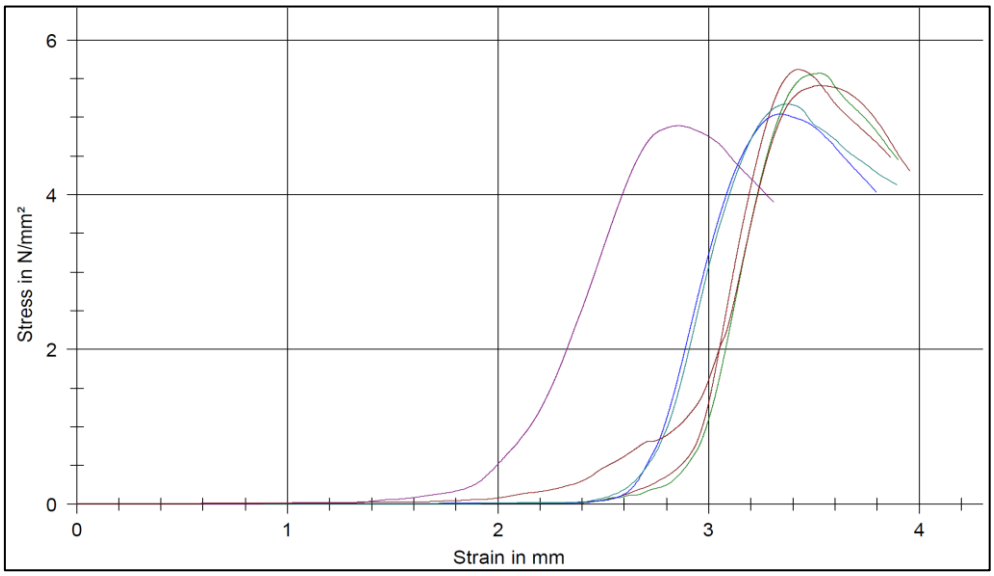

Fig. 24. The compressive strength at 300 °C.

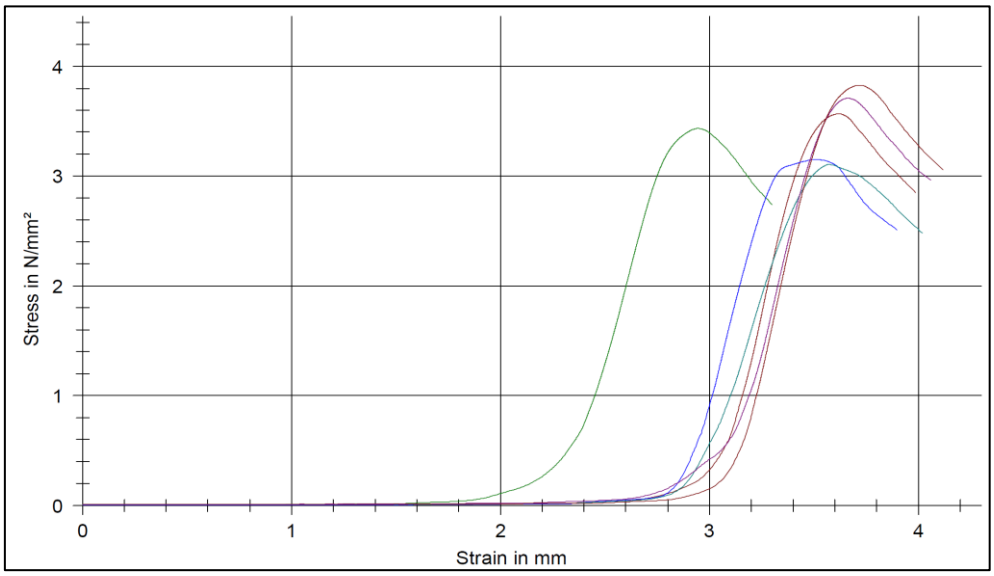

Fig. 25. The compressive strength at 400 °C.

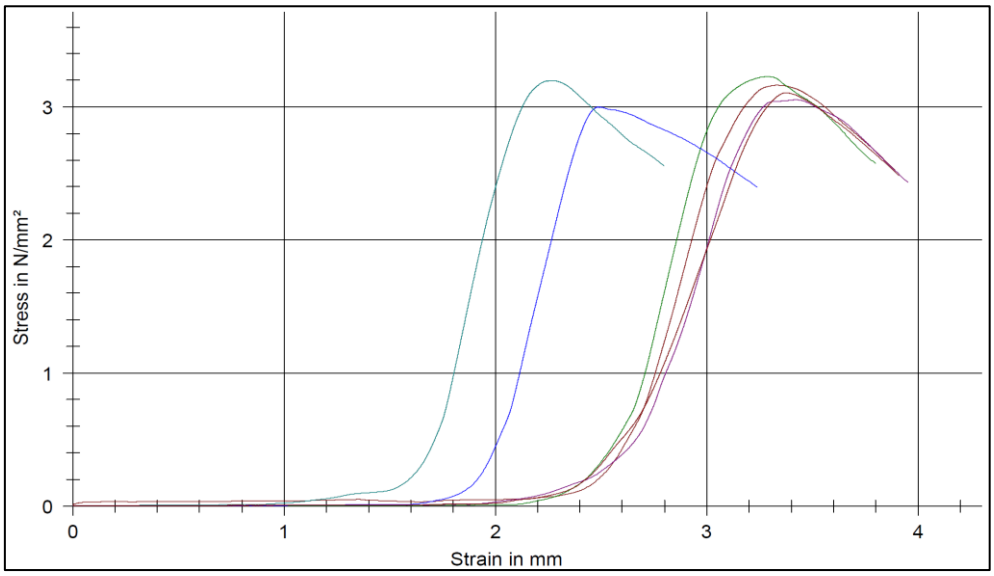

Fig. 26. The compressive strength at 500 °C.

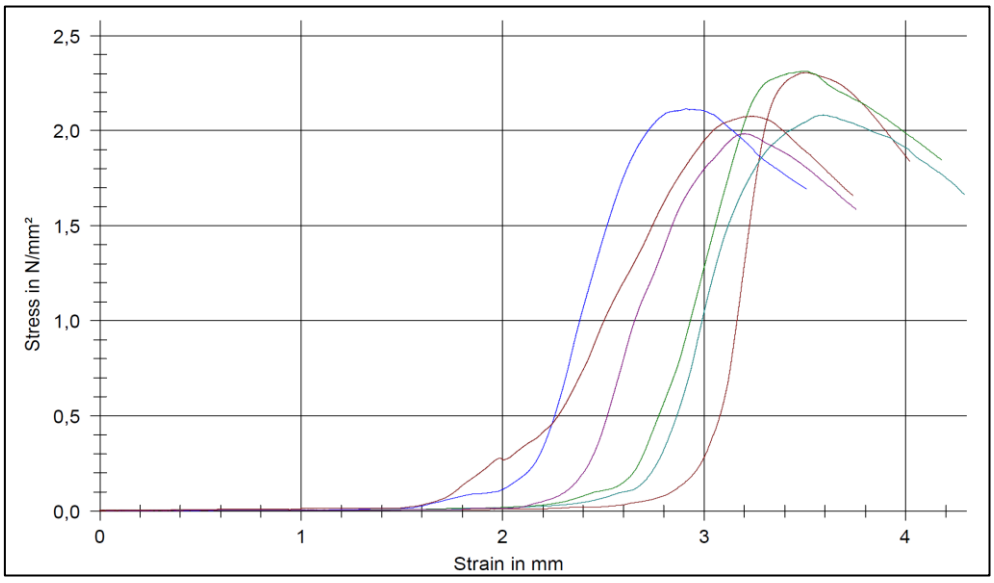

Fig. 27. The compressive strength at 600 °C.

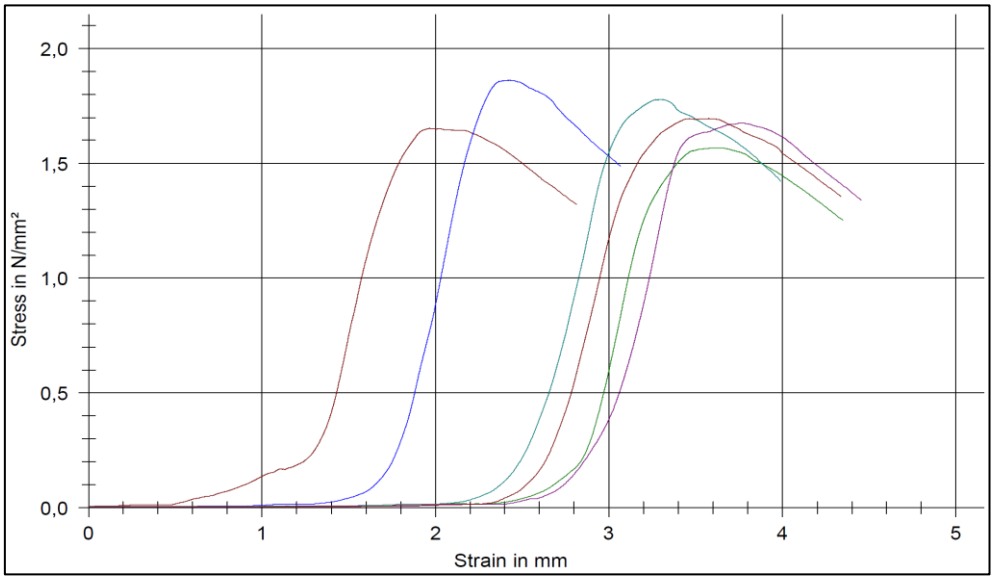

Fig. 28. The compressive strength at 700 °C.

Table 4. Data obtained from compression test results in N/mm² (MPa).

Specimen	Control (20 °C)	200 °C	300 °C	400 °C	500 °C	600 °C	700 °C
1	5,600	5,950	5,620	3,570	3,160	2,310	1,650
2	5,250	5,340	5,570	3,430	3,230	2,310	1,570
3	5,400	5,940	5,040	3,150	3,000	2,120	1,860
4	5,280	5,950	5,170	3,110	3,200	2,080	1,780
5	5,380	5,180	4,890	3,710	3,050	1,980	1,680
6	5,740	5,930	5,410	3,830	3,110	2,080	1,700
Average	5,442	5,715	5,283	3,467	3,125	2,147	1,707

The findings were compared with existing standards and codes, particularly Eurocode 6 and Turkish Seismic Code (TBDY-2018). It was observed that the Eurocode 6 assumption regarding the disappearance of strength values at 600 °C appeared conservative because the actual strength values at this temperature were higher than anticipated. Additionally, our results indicated alignment with class M1-2 as per TBDY-2018, highlighting the significance of considering the reduced material properties post-fire exposure for structural evaluation and safety.

In comparison to the assumption outlined in Eurocode 6, which suggests the disappearance of strength values at 600 °C, the actual compression strength at 600 °C diminishes to nearly 40% (2.1 MPa) of the ambient compression strength, whereas the flexural strength reduces to approximately 30% (0.6 MPa) of the flexural strength. This indicates that the Eurocode 6 assumption may have been overly conservative.

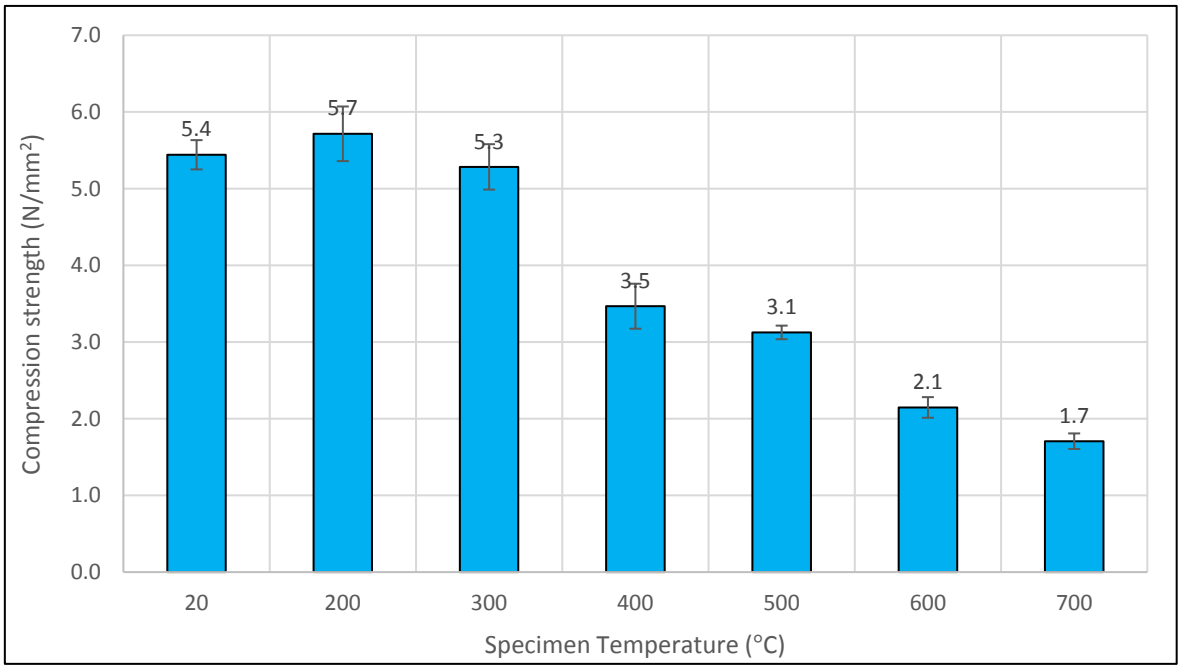

Fig. 29. Summary of compression strength test results.

6. Conclusions

From the moment historic masonry structures are erected, they face a myriad of challenges over time. These challenges inevitably result in damage, necessitating restoration and reinforcement endeavors. Among the materials employed in these efforts, HLMs stand out for their compatibility with the innate characteristics of historic construction. This research delves into assessing the fire resistance capabilities of HLMs.

In this study, HLMs were prepared in adherence to restoration standards followed by the crafting of prism specimens. These specimens were exposed to high temperatures ranging from 200 °C to 700 °C, after which bending and compression tests were carried out. A total of 27 specimens were meticulously prepared for ETTs, comprising three test specimens and one temperature-monitoring specimen for each temperature, along with three reference specimens. While the reference specimens were tested at room temperature, the remaining specimens were allowed to cool to room temperature post-fire exposure, following which they were tested under identical conditions to the reference specimens. In this study, the temperature monitoring specimens were solely utilized to track internal temperatures through embedded thermocouples; hence, no mechanical tests were conducted on them. The findings gleaned from these comprehensive experimental studies underscored that HLMs progressively lose their mechanical properties with escalating temperature. The flexural strength reduced to approximately 70% of the ambient value at 200 °C. Subsequently, from 200 °C onwards, there was a gradual decrease of approximately 10% until reaching 700 °C, resulting in a final flexural strength of approximately 20% of the ambient level. The compressive strength remains relatively stable at 300 °C. However, at 400 °C, it decreased to 60% of the compressive strength observed at ambient temperature. By the time it reached 700 °C, the compression strength had diminished to 1.7 N/mm^2, representing 30% of the strength recorded at ambient temperature. It is clearly seen that the compression strength experiences a slight decrease until reaching 300 °C. However, beyond this temperature, particularly after exposure to temperatures exceeding 300 °C, there was a significant decline in compressive strength, with values dropping by almost 30% compared to ambient conditions. Similarly, the flexural strength exhibits a gradually decreased up to 700 °C. However, even after exposure to temperatures as high as 700 °C, they still retained mechanical properties akin to those observed in lower-grade mortars. A compression value of 1.7 N/mm^2 at 700 °C exceeds the normal strength of masonry structures, suggesting that the Eurocode 6 assumption regarding strength loss at 600 °C is indeed conservative. Nevertheless, further evaluations, particularly those involving brick structural elements, are necessary to validate our conclusions. Despite the decline in strength, the compression strength at 700 °C (1.7 MPa) still retained considerable strength. Therefore, it can be inferred that it aligns with class M1-2, as per TBDY 2018.

Both energy absorption and compression strength of mortar declined significantly after 300 °C. Understanding how the mechanical strength of mortar varies with temperature is essential for designing structures that

can effectively withstand thermal fluctuations. The results obtained can be utilized for the purpose of conducting a detailed micro-modelling of masonry structures. Furthermore, they can be employed as input data for the mortar part of the structural elements after fire exposure (thermal analysis) at related elevated temperature.

Further analysis and modeling based on these test results can provide valuable insights into the behavior of HLM under different environmental conditions, aiding in the development of more resilient and durable construction materials. In the event of collapse of historical structural elements following fire exposure, it is imperative to conduct further assessments considering the reduced material properties post-fire exposure. Further assessments will be performed for the structural analysis of masonry arch structures at elevated temperatures in actual fire cases.

Acknowledgements

The authors are sincerely grateful to Mr. İsmail Yıldırım and Mr. Osman Aydoğdu for their collaboration in conducting laboratory compression and flexural testing at the Turkish Standards Institution.

Funding

The authors received no financial support for the research, authorship, and/or publication of this manuscript.

Conflict of Interest

The authors declared no potential conflicts of interest with respect to the research, authorship, and/or publication of this manuscript.

Author Contributions

All of the authors made substantial contributions to conception and design, or acquisition of data, or analysis and interpretation of data; were involved in drafting the manuscript or revising it critically for important intellectual content; and gave final approval of the version to be published.

Data Availability

The datasets created and/or analyzed during the current study are not publicly available, but are available from the corresponding author upon reasonable request.

REFERENCES

Aruntaş HY, Şahinöz M, Dayı M, (2021). Çimento hamur ve harçlarında kireç kullanımının incelenmesi. *Politeknik Dergisi,* 24(3), 1045–1054. (in Turkish)

Bamonte P, Gambarova PG, Sciarretta F (2021). Thermo-mechanical properties and stress-strain curves of ordinary cementitious mortars at elevated temperatures. *Construction and Building Materials*, 267, 121027.

Bompa DV, Elghazouli AY (2020). Compressive behaviour of fired-clay brick and lime mortar masonry components in dry and wet conditions. *Materials and Structures,* 53(3), 60.

Cakir F (2011). Assessment of Structural Integrity and Seismic Retrofit of Masonry Bridges Using Micropiles. *M.Sc. thesis,* Illinois Institute of Technology, USA.

EN 998-2 (2011). Specification for mortar for masonry - Part 2: Masonry mortar. European Committee for Standardization, Brussels, Belgium.

EN 1015-11 (2019). Methods of test for mortar for masonry - Part 11: Determination of flexural and compressive strength of hardened mortar. European Committee for Standardization, Brussels, Belgium.

EN 1363-1 (2020). Fire resistance tests General requirements. European Committee for Standardization, Brussels, Belgium.

EN 1996-1-2 (2005). Eurocode 6 - Design of masonry structures - Part 1-2: General rules - Structural fire design. European Committee for Standardization, Brussels, Belgium.

Horszczaruk E, Sikora P, Cendrowski K, Mijowska E (2017). The effect of elevated temperature on the properties of cement mortars containing nanosilica and heavyweight aggregates. *Construction and Building Materials,* 137, 420–431.

İsafça KT, Karakuzu K, Mardani A, Doğangün A (2022). Yüksek sıcaklığın polipropilen lif takviyeli Horasan harcının bazı özelliklerine etkisi. *Avrupa Bilim ve Teknoloji Dergisi,* (37), 96–101. (in Turkish)

ISO 834-1 (2014). Fire resistance tests. Elements of building construction Specific requirements for the assessment of fire protection to structural steel elements. International Organization for Standardization, Geneva, Switzerland.

Karahan O (2010). Residual compressive strength of fire-damaged mortar after post-fire-air-curing. *Fire and Materials,* 35(8), 561–567.

Neto JADF, Sombra TN, Haach VG, Corrêa MRS (2022). Effects of post-fire curing on the residual mechanical behavior of cement-lime masonry mortars. *Construction and Building Materials*, 327, 126613.

Pachta V, Stefanidou M (2021). Evaluation of the behaviour of lime and cement based mortars exposed at elevated temperatures. *12th International Conference on Structural Analysis of Historical Constructions.*

Pachta V, Triantafyllaki S, Stefanidou M (2018). Performance of lime-based mortars at elevated temperatures. *Construction and Building Materials,* 189, 576–584.

Pachta V, Tsardaka EC, Stefanidou M (2021). The role of flame retardants in cement mortars exposed at elevated temperatures. *Construction and Building Materials,* 273, 122029.

Pan Z, Tao Z, Murphy T, Wuhrer R (2017). High temperature performance of mortars containing fine glass powders. *Journal of Cleaner Production,* 162, 16–26.

Rais MS, Shariq M, Masood A, Umar A, Alam MM (2019). An experimental and analytical investigation into age-dependent strength of fly ash mortar at elevated temperature. *Construction and Building Materials,* 222, 300–311.

Sánchez IB (2007). Strengthening of Arched Masonry Structures with Composite Materials. *Ph.D. thesis,* University of Minho, Julho, Portugal

TBDY (2018). Turkish Building Earthquake Code. Disaster and Emergency Management Presidency (AFAD), Ankara, Türkiye.

Zhang P, Zheng Y, Wang K, Zhang J (2018). A review on properties of fresh and hardened geopolymer mortar. *Composites Part B: Engineering,* 152, 79–95.

Challenge Journal of Structural Mechanics

Research Article

Mechanical characterization of FDM-printed PLA: Role of infill geometry and build direction

Tevfik Oğuzhan Ergüder [a,*], Caner Bulut [b]

[a] *Department of Mechanical Engineering, Kafkas University, 36100 Kars, Türkiye*
[b] *Technical Sciences Vocational School, Iğdır University, 76000 Iğdır, Türkiye*

ABSTRACT

This study examines the mechanical behavior of polylactic acid (PLA) components produced via Fused Deposition Modeling (FDM), focusing on the effects of infill geometry and build orientation on tensile strength and deformation. Three infill patterns–Cubic Subdivision, Gyroid, and Tri-Hexagon–were combined with three build orientations (0°, 45°, and 90°) using an L9 Taguchi orthogonal array to systematically evaluate their influence and identify optimal configurations. ASTM D638 Type IV tensile specimens were fabricated and tested to assess performance. The results revealed that the Gyroid pattern at a 90° build orientation achieved the highest tensile strength (987.3 N), while the 45° build orientation exhibited the greatest ductility (3.39 mm), reflecting the anisotropic mechanical behavior inherent to FDM. The Tri-Hexagon pattern displayed brittle fracture characteristics, whereas the Cubic Subdivision offered intermediate performance. Analysis of variance (ANOVA) identified infill pattern as the most significant factor, accounting for 86.52% of the variation in mechanical properties, while build orientation contributed 6.29%. These findings emphasize that infill strategy plays a far more decisive role than build orientation in determining mechanical performance. Overall, the study provides practical insights into optimizing FDM-printed components by selecting appropriate infill patterns and build orientations to meet application-specific requirements, particularly where strength or energy absorption is critical. The results can serve as a reference for designers and engineers aiming to enhance the structural efficiency and reliability of 3D-printed PLA parts.

ARTICLE INFO

Article history:
Received – July 6, 2025
Revision requested – August 5, 2025
Revision received – August 11, 2025
Accepted – August 22, 2025

Keywords:
3D printing
Mechanical testing
Polylactic acid
Fused deposition

Citation: Ergüder TO, Bulut C (2025). Mechanical characterization of FDM-printed PLA: Role of infill geometry and build direction. *Challenge Journal of Structural Mechanics*, 11(4), 201–214.

1. Introduction

With the rapid evolution of modern technology and the accelerating transformation of industrial systems, significant progress has been achieved in both materials and manufacturing techniques to address the increasingly complex and diverse demands of industry. Among these innovations, additive manufacturing (AM) has gained widespread attention for its ability to produce three-dimensional components directly from computer-aided design (CAD) models, without the need for conventional molds or tooling. Unlike subtractive manufacturing methods that remove material to achieve the desired shape, AM builds parts layer by layer, offering significant advantages such as reduced material waste, enhanced design flexibility, and shortened production cycles (Huang et al. 2013; Zhou et al. 2024). These benefits have led to the rapid adoption of AM technologies across various sectors, including aerospace, automotive, biomedical engineering, architecture, and education, particularly in applications requiring complex geometries, rapid prototyping, and product customization.

* *Corresponding author*. E-mail address: oguzhan.erguder@kafkas.edu.tr (T. O. Ergüder)
ISSN: 2149-8024 / DOI: https://doi.org/10.20528/cjsmec.2025.04.003

Among AM techniques, Fused Deposition Modeling (FDM) has emerged as one of the most prevalent methods, particularly for the fabrication of polymer-based components. Its widespread adoption is largely attributed to its operational simplicity, cost-effectiveness, and accessibility across both industrial and desktop-scale platforms. In this process, a thermoplastic filament—commonly PLA or acrylonitrile butadiene styrene (ABS)—is fed into a heated nozzle, melted, and extruded in a controlled manner along a predefined toolpath. The material is deposited layer by layer onto a build platform, where it solidifies and bonds with preceding layers to form the final three-dimensional structure. FDM technology offers several advantages over traditional subtractive techniques, including reduced material waste, shortened production lead times, and the ability to fabricate components with complex geometries, hollow sections, and customized internal infill patterns (Rajpurohit and Dave 2018; Solomon et al. 2020; Le et al. 2022; Equbal et al. 2024). Other FDM advantage is the elimination of dies and molds, which is an investment that needs to be made whenever the designs are changed. This makes FDM or AM a useful technique when high customization is necessary. FDM is still a novel technology that produces parts with a quality that is not currently comparable to the injection molding parts (Alafaghani and Qattawi 2018). These attributes make FDM particularly well-suited for rapid prototyping and low-volume manufacturing. Furthermore, materials such as PLA are frequently preferred due to their biodegradability, low warping behavior, and favorable strength-to-weight ratio (Equbal et al. 2024).

However, despite its many advantages, the mechanical integrity of FDM-printed parts is highly sensitive to various process parameters, including layer thickness, nozzle temperature, printing speed, infill density, and build orientation. Among these, build orientation and raster angle are particularly critical due to the anisotropic nature of the layer-by-layer deposition process. When the applied load is aligned either parallel or perpendicular to the printed layers, significant variations in tensile strength, ductility, and failure behavior can occur—primarily resulting from differences in interlayer bonding and internal stress distribution. Numerous studies have demonstrated that even slight changes in build orientation or raster angle can lead to substantial differences in mechanical performance, including elastic modulus and fracture behavior (Casavola et al. 2016; Yao et al. 2019; Taşdemir 2024). This anisotropic response presents a major challenge in functional applications where uniform mechanical properties are essential under complex loading conditions. Therefore, understanding and optimizing these build orientation-related parameters is crucial for enhancing the structural reliability and overall performance of FDM-printed components (Alafaghani and Qattawi 2018; Ambade et al. 2023).

Several recent studies have systematically explored the influence of FDM process parameters, internal structures, and deposition strategies on the mechanical performance and consistency of printed parts. Dezaki and Ariffin (2020) showed that combining infill patterns like grid and honeycomb can significantly improve mechanical integrity compared to single-pattern designs. In terms of fracture behavior, Marşavina et al. (2022) demonstrated that crack propagation paths vary significantly with build orientation, highlighting the strong anisotropy induced by the layer-wise process. Similarly, Zhao et al. (2019) focused on how internal geometry and wall thickness affect stress distribution and found that optimized internal designs can delay failure and increase energy absorption. Akhoundi and Behravesh (2019) further reported that concentric infill patterns outperformed other patterns such as rectilinear or honeycomb in tensile and flexural tests, indicating a pattern-dependent load distribution mechanism. Le et al. (2022) emphasized the importance of balancing mechanical performance with production efficiency, demonstrating that specific combinations of infill density, nozzle diameter, and shell count can reduce build time without significantly compromising strength. Laureto and Pearce (2018) provided quantitative insight into anisotropic mechanical behavior, noting a nearly 48% reduction in tensile strength for vertically printed PLA specimens compared to horizontal ones. Vălean et al. (2020) investigated the effects of spatial printing directions (0°, 45°, 90°) and specimen thickness on tensile properties, finding that orientation strongly influences tensile strength but has a lesser impact on Young's modulus, and also showed that key FDM parameters such as infill density, layer thickness, and print speed significantly affect tensile strength of PET-G parts. Ambade et al. (2025) demonstrated that optimized build orientation combined with specific infill geometries can significantly enhance tensile performance without increasing print time. Zhou et al. (2024) highlighted the role of advanced infill architectures, such as triply periodic minimal surfaces, in improving both load distribution and energy absorption in lightweight structural applications. These studies demonstrate that ensuring directional strength and structural consistency in FDM requires process-aware and multivariable optimization approaches. While several studies have individually optimized infill pattern or build orientation to enhance the mechanical properties of FDM-printed components, comprehensive investigations that address the combined and simultaneous optimization of both parameters remain limited. This gap is particularly evident for PLA-based applications, where anisotropic behavior and load distribution mechanisms are strongly influenced by the interaction between internal geometry and build orientation. The present study addresses this gap through a systematic Taguchi-based approach.

In this study, the mechanical behavior of FDM-printed PLA components was systematically investigated with respect to infill pattern and build orientation—two key parameters known to affect part strength and anisotropy. Standard tensile specimens were produced using three distinct infill geometries (Cubic Subdivision, Gyroid, and Tri-Hexagon) at three different printing angles (0°, 45°, and 90°), in accordance with ASTM D638 standards. An L9 Taguchi orthogonal array design was employed to efficiently explore the influence of these parameters on tensile strength and deformation character-

istics. The objective is to identify optimal combinations of internal structure and build orientation that improve the mechanical performance of PLA-based FDM components. The findings of this study are expected to support parameter optimization in additive manufacturing processes, particularly for applications where dimensional accuracy, mechanical reliability, and load-bearing capacity are critical.

2. Experimental Methodology

This article analyzes the mechanical performance of parts manufactured using PLA as a filament. Table 1 shows the data provided by the manufacturer for the filament used. The additive manufacturing equipment to be used is the Creality Ender 3 V3 SE 3D printer using FDM technology (Fig. 1).

Table 1. Technical specifications of the filament used.

Material	Color	Tensile strength (MPa)	Elongation at break (%)	Tensile modulus (MPa)	Density (g/cm^3 at 21.5 °C)
PLA+	White	40–50	7–8	750–910	1.24 ±0.1

Fig. 1. FDM 3D printer used in the production of experimental samples.

The Creality Print software is used to transfer the 3D models of the samples to G-code. The basic technical specifications of the FDM printer are described in Table 2.

The samples used in this study to evaluate the dimensional accuracy, repeatability, and mechanical properties were modeled according to the American Society for Testing and Materials ASTM D638 type IV standards for plastic tensile testing. Fig. 2 shows the dimensions used to create the CAD model.

Fig. 3 presents schematic representations of three filling patterns of Gyroid, Cubic Subdivision and Tri-Hexagonal structures. Gyroid pattern, a continuous wave-like 3D surface without flat planes, providing isotropic load distribution and improved interlayer adhesion. Its smooth curvature minimizes stress concentrations, potentially enhancing both strength and ductility (Khaderi et al. 2014; Silva et al. 2021). Cubic subdivision, a lattice-like cubic structure subdivided into smaller cells, offering balanced rigidity and weight reduction, with load transfer primarily along straight struts (Jasim et al. 2022; Rahman et al. 2023). Tri-Hexagon, a planar pattern composed of interlinked triangular and hexagonal cells, forming a stiff and lightweight grid. While this design provides high rigidity, stress concentrations at the vertices may reduce ductility (Tandon et al. 2021, 2025; Abdullah and Abbas 2023). After printing, dimensional accuracy of the specimens was verified using a digital caliper with ±0.01 mm resolution. Measurements were taken on critical features defined by the ASTM D638 Type IV standard, including overall length, gauge length, and width. All printed specimens were within ±0.2 mm of the nominal CAD dimensions, ensuring compliance with the standard's dimensional tolerance requirements.

Table 2. Technical specifications of the FDM 3D printer.

Printing technology	Fused deposition modelling
Build volume (mm)	220×220×250
Printing speed (typical – max) (mm/s)	180–250
Acceleration (mm/s^2)	2500
Layer height (mm)	0.1–0.35
Extruder type	"Sprite" direct extruder
Nozzle temperature (°C)	≤ 260
Heatbed temperature (°C)	≤ 100
Nozzle diameter (mm)	0.4

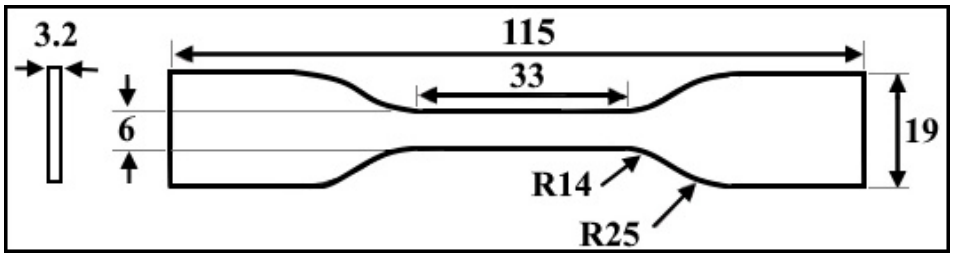

Fig 2. ASTM D638 type IV samples.

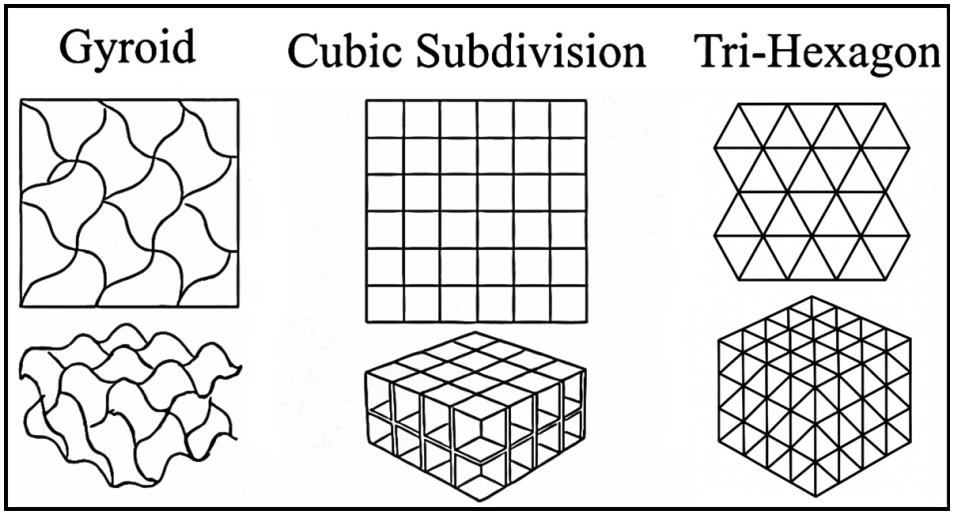

Fig. 3. The schematic representations of three filling patterns of Gyroid, Cubic Subdivision and Triple Hexagonal structures.

This 3D model was then transferred to the Creality Print slicing software to generate the appropriate G-code for printing, as illustrated in Fig. 4. After slicing, the printer settings were optimized. The fixed printing parameters were as follows: nozzle temperature (200 °C), heatbed temperature (60 °C), print speed (180 mm/s), layer height (0.2 mm), and nozzle diameter (0.4 mm). Variable parameters infill pattern and build orientation were selected as controllable factors in this study and are listed in Table 3. Each parameter was tested at multiple levels using a L9 orthogonal Taguchi Design of Experiments (DoE) approach to ensure robust statistical evaluation. The results were analyzed by signal-to-noise ratio (S/N), mean values and standard deviations. In addition, the statistical significance of the factors was evaluated by ANOVA. All statistical analyses were performed using Minitab® Statistical Software (version 21.1.1). Both the ANOVA and signal-to-noise (S/N) ratio calculations were conducted using parametric methods.

Prior to analysis, the Anderson–Darling test confirmed that residuals followed a normal distribution ($p>0.05$), and Levene's test verified homogeneity of variances ($p>0.05$), meeting the assumptions required for valid parametric inference. The Taguchi L9 orthogonal array was selected to evaluate the effects of two control factors—infill pattern (Cubic Subdivision, Gyroid, Tri-Hexagon) and build orientation (0°, 45°, 90°)—each at three levels. According to Taguchi design principles, an L9 array provides a balanced comparison of factor levels while reducing the total number of experiments from 27 (full factorial) to 9, thereby conserving material, time, and experimental resources without sacrificing statistical validity for main effects analysis. The choice of these two parameters was guided by prior literature identifying them as the most influential on the anisotropic tensile performance of FDM-printed PLA parts. Other process variables, including layer height, nozzle temperature, print speed, and infill density, were held constant to isolate the effects of the selected factors. The main limitation of this approach lies in its inability to fully capture higher-order interaction effects or responses under different environmental conditions. Furthermore, the analysis was restricted to PLA material and a specific set of geometries, which may limit direct generalization to other materials or process settings.

Table 3. Variable parameters for all specimens.

Process parameters	Level 1	Level 2	Level 3
Infill pattern	Cubic Subdivision	Gyroid	Tri-Hexagon
Build orientation	0°	45°	90°

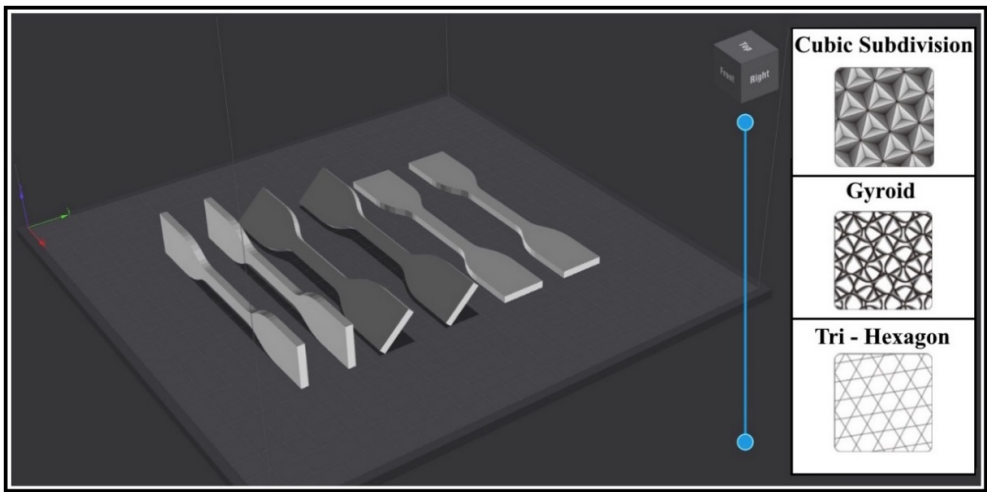

Fig. 4. Slicing in flash print software tensile model.

An experimental matrix consisting of nine test conditions was developed, incorporating three different build orientations (0°, 45°, and 90°) and three infill patterns (Cubic Subdivision, Gyroid, and Tri-Hexagon). As shown in Table 4, for each of the nine experimental conditions defined in the L9 Taguchi orthogonal array, two identical specimens were fabricated and tested to assess repeatability and minimize experimental error. The number of repetitions was limited to two to preserve the efficiency of the Taguchi design. Statistical analyses, including ANOVA and S/N ratio evaluation, were performed to verify the consistency of the results. Images of samples with different infill pattern after production are shows in Fig. 5.

Table 4. Taguchi experiment L9 matrix**.**

Exp. no.	Nomenclature samples	Infill pattern	Build orientation
1	C0	Cubic Subdivision	0°
2	C45	Cubic Subdivision	45°
3	C90	Cubic Subdivision	90°
4	G0	Gyroid	0°
5	G45	Gyroid	45°
6	G90	Gyroid	90°
7	T0	Tri-Hexagon	0°
8	T45	Tri-Hexagon	45°
9	T90	Tri-Hexagon	90°

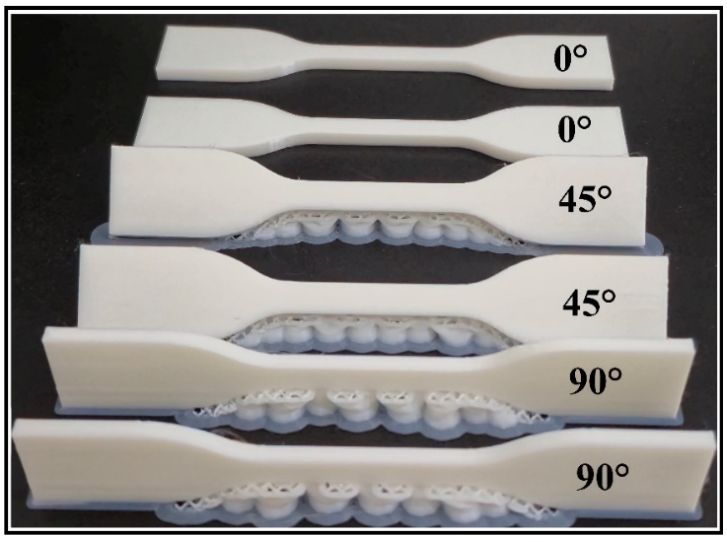

Fig. 5. Tensile test samples produced in different orientations.

After fabrication, the samples were subjected to tensile testing using an INSTRON 5982 universal testing machine to evaluate their mechanical performance tensile strength and elongation at break. As illustrated in Fig. 6, the tests were conducted at room temperature on a static testing machine with a constant crosshead speed of 5 mm/min, in accordance with ASTM D638 Type IV standards for FDM-fabricated specimens.

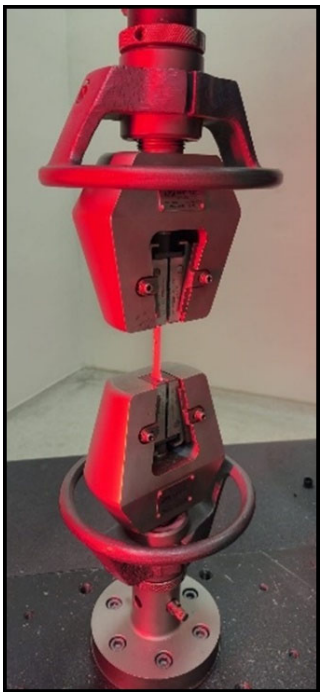

Fig. 6. The image of experimental samples in the tensile test device.

3. Results and Discussion

The Taguchi optimization technique, employed in process improvement, follows an eight-step methodology involving the design, execution, and evaluation of matrix experiments to determine the ranking and optimal levels of control factors (Arora et al. 2023). The Taguchi method was applied to systematically evaluate the effects of infill pattern and build orientation on the tensile strength and elongation at break of PLA-based FDM specimens. An L9 orthogonal array design was selected to reduce the number of experiments while maintaining statistical validity. The experimental results were then analyzed to determine the optimal levels of control factors and their relative influence on mechanical properties.

3.1. Analysis of experimental tensile tests

In this section, the results of all tensile tests are presented by systematically grouping the data according to constant infill patterns and build orientations. The mechanical performance of each group is evaluated under distinct headings to facilitate a clearer comparison of the effects of individual parameters. Fig. 7 presents the post-tensile test appearance of specimens fabricated via FDM using different infill patterns (Gyroid, Cubic Subdivision, Tri-Hexagon) and build orientations (0°, 45°, 90°). It is observed that fractures predominantly occurred in the central region, with fracture surfaces varying depending on the infill pattern and build orientation. Specimens printed at 90° exhibited greater deformation, indicating a more ductile fracture behavior, whereas those printed at 0° showed sharper and more brittle fracture characteristics. In the 45° oriented specimens, inclined and irregular fracture surfaces suggest that interlayer interactions had a significant influence on the failure behavior. The slight drop in force observed around 200 N in the all tensile curves can be attributed to early micro-failure at interlayer zones or void collapse in transition regions between outer shell and internal infill. Adragna et al. (2021) and Marșavina et al. (2022) reported similar behavior in PLA specimens with complex infill geometries, where local instabilities caused a momentary force reduction, followed by stress redistribution across the infill, allowing for a secondary rise in force prior to failure.

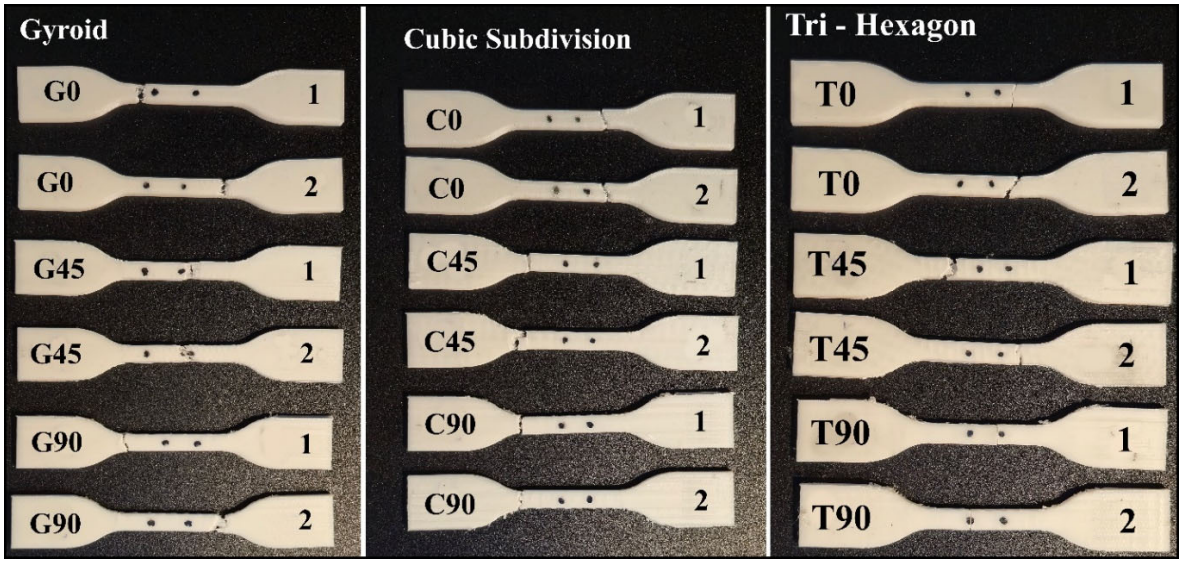

Fig. 7. Images of samples after tensile testing.

3.1.1. Effect of infill pattern on mechanical properties

The tensile graphs of different infill patterns, keeping the build orientation constant as 0°, are presented in Fig. 8. The maximum load and maximum elongation of the samples in different infill patterns of this figure were evaluated. The load-displacement curves obtained as a result of the tensile tests clearly reveal the effects of different internal structure patterns on mechanical performance. Samples with G0, T0 and C0 patterns were produced with the same build orientation (0°) and showed significant differences in terms of their load carrying capacities and ductility during deformation. The T 0 sample with the Tri-hexagon pattern reached the highest maximum load value of approximately 800 N, indicating that this pattern was the most advantageous structure in terms of strength. However, this sample exhibited a sudden load loss after reaching the peak point and fractured at a lower displacement; this situation suggests that the structure exhibited a relatively brittle behavior. On the other hand, the G0 sample with the Gyroid pattern reached a similar load level but showed a longer deformation zone before rupture. This situation reveals that the Gyroid structure has high ductility and energy absorption capacity. The cubic patterned C0 sample exhibited a moderate performance in terms of both maximum load and ductility.

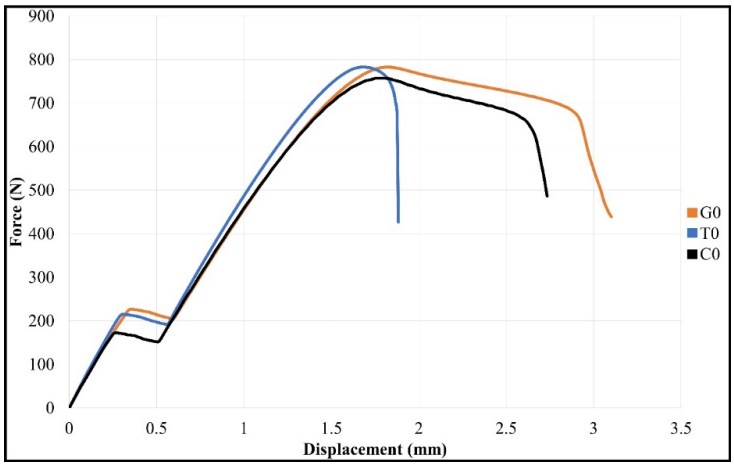

Fig. 8. Effect of infill geometry on tensile behavior at 0° orientation.

Fig. 9 shows the tensile force–displacement behavior of specimens manufactured with a Gyroid infill pattern under 45° build orientation. The load-displacement curves of the samples with 45° built-up orientation once again revealed the effect of infill patterns on the mechanical behavior. When the G45, T45 and C45 patterns were compared, the Gyroid structure had the highest maximum load capacity (~840 N) and the largest deformation area. This shows that the Gyroid pattern maintained its high ductility and toughness properties even at the 45° built-up orientation. The T45 and Cubic C45 patterns reached lower peak loads around 740–760 N and showed earlier fracture. Especially the T45 sample exhibited a relatively brittle behavior with a sudden load drop. The Cubic C45 patterned sample exhibited a more stable behavior, but was limited in terms of ductility. It is also understood that the 45° orientation changes the bond strength between layers and affects the direction of load transfer, thus differentiating the mechanical response. In this context, it is seen that the Gyroid pattern stands out with both its high load carrying capacity and its ability to absorb energy during the deformation process, and that it can maintain its structural integrity even in the 45° build orientation. Jasim et al. (2022) reported that the choice of infill pattern alone can change PLA tensile strength by more than 25% and that gyroscopic type patterns consistently outperform linear and honeycomb designs in terms of strength-to-weight ratio.

Fig. 10 shows the tensile force–displacement behavior of specimens manufactured with a Gyroid infill pattern under 90° build orientation. The load-displacement curves of the samples produced in 90° build orientation made the effect of infill patterns on mechanical performance more evident. The sample with G90 pattern reached the highest maximum load value of approximately 1000 N and maintained its superiority in terms of strength at this orientation angle. In addition, the G90 sample not only carried high loads but also showed a longer deformation until the point of failure. This shows that the Gyroid structure exhibits both ductile and tough behavior. The samples with Tri-hexagon T90 and Cubic C90 patterns reached a maximum load carrying capacity of approximately 850–880 N. These patterns showed higher strength at 90° compared to the previous orientations, but the deformation time was shorter compared to the Gyroid pattern. In particular, the T90 sample exhibited a more brittle fracture behavior characterized by a sudden drop. The Cubic patterned C90 sample has a relatively more balanced fracture profile and shows a more positive behavior in terms of ductility than T90. However, these results obtained along the 90° build orientation reveal that aligning the layers perpendicular to the load direction increases the load carrying capacity and especially the Gyroid pattern is the most advantageous structure mechanically under this orientation. Consistent with the present findings, recent work on TPMS-based gyroid structures confirmed their superior isotropic load distribution and higher specific strength compared to lattice or grid designs, particularly under multi-axial loading (Alemayehu and Todoh 2024).

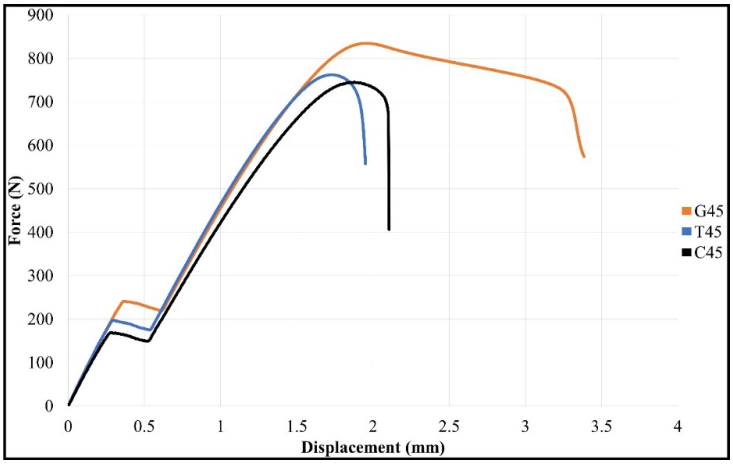

Fig. 9. Effect of infill geometry on tensile behavior at 45° orientation.

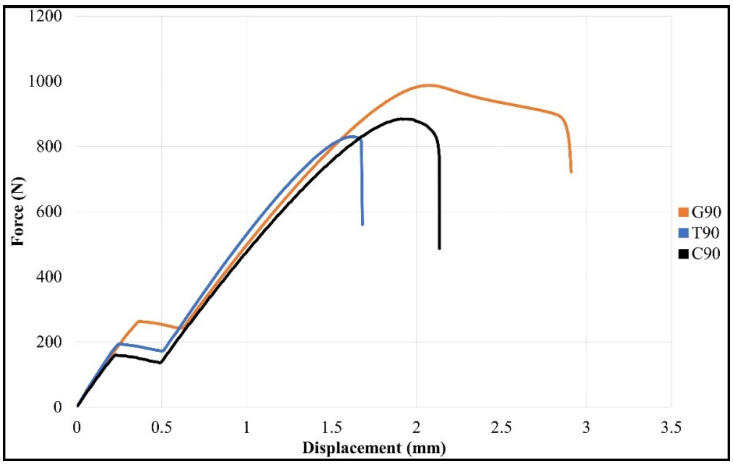

Fig. 10. Effect of infill geometry on tensile behavior at 90° orientation.

3.1.2. Effect of build orientations on mechanical properties

Fig. 11 shows the tensile force–displacement behavior of specimens manufactured with a Gyroid infill pattern under three different build orientations: 0°, 45°, and 90°. The results clearly demonstrate the significant influence of build orientation on mechanical performance. The G90 specimen exhibited the highest tensile strength, reaching approximately 1000 N, along with the greatest displacement before failure. This indicates a more ductile fracture behavior and suggests that aligning the printed layers parallel to the loading direction enhances interlayer adhesion and load transfer. In contrast, the G0 specimen, where the printed layers are perpendicular to the tensile axis, recorded the lowest maximum force (~780 N) and fractured with minimal elongation, exhibiting a brittle failure mode. The G45 specimen showed intermediate behavior in terms of both strength (~860 N) and ductility. These observations confirm the anisotropic nature of FDM-printed components and underscore the importance of build orientation in optimizing mechanical properties, even when using geometrically continuous infill patterns like Gyroid. Dawood and AlAmeen (2024), in their study on carbon fiber-reinforced PLA parts, similarly reported that the Gyroid infill pattern provided higher tensile strength and fatigue resistance compared to other infill types. They noted that, particularly at high infill densities, the Gyroid structure distributed the load more uniformly and delayed crack propagation, significantly increasing both the strength and fatigue life of the part. A similar orientation-dependent trend was reported by Vanaei et al. (2023), who found that changing the build orientation of FDM-printed PLA from 0° to 90° increased Young's modulus by approximately 40% and ductility by nearly 70%, with numerical simulations (Tsai–Hill, Tsai–Wu criteria) and FE models confirming the experimental results.

Fig. 12 illustrates the tensile force–displacement behavior of PLA specimens fabricated using the Cubic Subdivision infill pattern at three different build orientations: 0°, 45°, and 90°. The results demonstrate a clear orientation-dependent mechanical response, consistent with the anisotropic behavior commonly observed in FDM-printed parts. Among the tested samples, the C90° specimen exhibited the highest tensile strength, reaching approximately 900 N, along with the steepest force increase during loading. However, the displacement at fracture was relatively limited, suggesting a stiffer but more brittle failure mode. This behavior may be attributed to the alignment of the printed layers perpendicular to the tensile axis, where interlayer bonding

plays a dominant role in resisting the applied load. In contrast, the C0 specimen demonstrated a lower peak force (~770 N) but sustained deformation over a longer displacement range, indicating a more ductile fracture mode. Since the printed layers were aligned parallel to the tensile direction, the load was distributed more uniformly along the filament paths, which enhanced elongation prior to failure despite a moderate tensile strength. The C45 specimen showed intermediate performance, with a maximum force of approximately 750 N and moderate ductility. This result can be attributed to the oblique alignment of the filament layers, which introduces complex stress paths and partial shear contributions during loading.

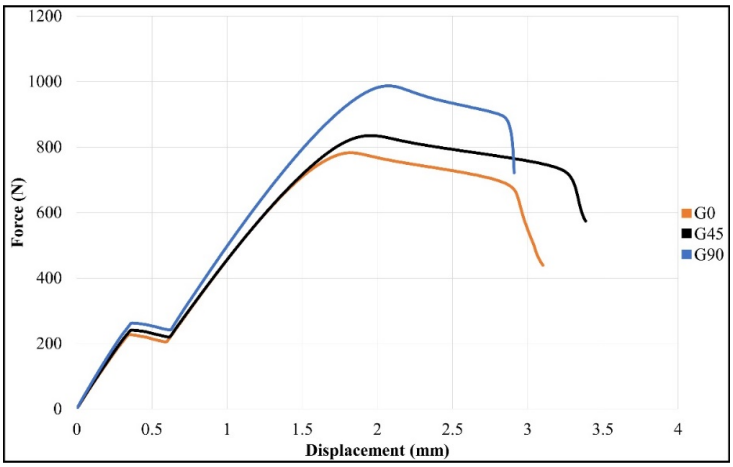

Fig. 11. Effect of Gyroid infill geometry on tensile behavior in 0° - 45° - 90° orientation.

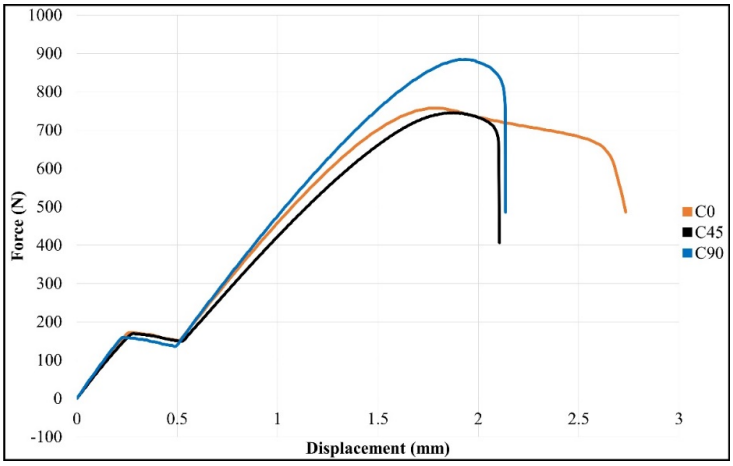

Fig. 12. Effect of Cubic Subdivision infill geometry on tensile behavior in 0° - 45° - 90° orientation.

Fig. 13 illustrates the tensile force–displacement curves for PLA specimens produced using the Tri-Hexagon infill pattern at three build orientations: 0°, 45°, and 90°. The results reveal a clear dependence of mechanical performance on build direction. Among the samples, T90 exhibited the highest tensile strength, reaching approximately 840 N, and also demonstrated the greatest elongation before failure. This indicates enhanced ductility and improved interlayer bonding when the print layers are oriented parallel to the applied load. Conversely, the T0 specimen, with layers-oriented perpendicular to the loading direction, showed a lower peak force (~780 N) and reduced displacement, suggesting a more brittle fracture mechanism. The T45 sample performed intermediately in both strength (~800 N) and ductility. Although the differences among the orientations are less dramatic compared to other infill patterns, the T90 orientation still offers measurable mechanical advantages. These findings confirm the anisotropic behavior of FDM-fabricated parts and highlight the importance of aligning the build orientation with the loading direction to optimize mechanical performance, even in complex infill structures like the Tri-Hexagon pattern.

3.1.3. Analyses of maximum force and maximum displacement

The effects of infill geometry and structure orientation (0°, 45° and 90°) on the maximum force and maximum displacement are presented in Fig. 14. Error bars in Fig. 14 indicate the mean ± standard deviation, providing a visual representation of variability across the two repeated tests for each configuration. When analyzing the maximum force, the highest value was observed for the Gyroid infill with 90° build orientation (G90: 987.3 N). This result suggests that the continuous, wave-like

three-dimensional geometry of the Gyroid structure, when aligned perpendicularly to the loading axis, allows for more efficient stress distribution and improved layer adhesion, resulting in enhanced load-bearing capacity. Additionally, G90 outperformed all other combinations, indicating that the synergistic effect of a complex infill geometry and optimized orientation contributes significantly to tensile strength. In comparison, the Tri-Hexagon infill exhibited lower maximum force values across all orientations. The T90 sample recorded a maximum force of 830.1 N, which is approximately 16% lower than G90. Although the Tri-Hexagon pattern offers rigidity due to its hexagonal grid, it may not align as effectively with the tensile load direction, leading to stress concentrations and earlier failure. Nevertheless, an increasing trend was observed with build orientation: T0 (783.5 N), T45 (762.8 N), and T90 (830.1 N), suggesting that higher build angles may contribute positively to interlayer strength and filament alignment. The Cubic Subdivision infill generally showed the lowest tensile strength in 0° and 45° orientations, with values of 757.7 N (C0) and 745.7 N (C45). However, a significant increase was observed at 90° orientation, reaching 884.2 N (C90). This improvement is likely due to the cubic cell structures being better aligned with the tensile axis at 90°, facilitating improved load transfer. Nevertheless, even C90 remained approximately 10% lower in strength than G90, indicating the superior mechanical response of the Gyroid pattern under optimized orientation. Le et al. (2022) demonstrated that specific combinations of infill density, nozzle diameter, and shell count can significantly reduce print time while maintaining over 90% of the original tensile strength, stated the potential for balancing manufacturing efficiency with mechanical performance.

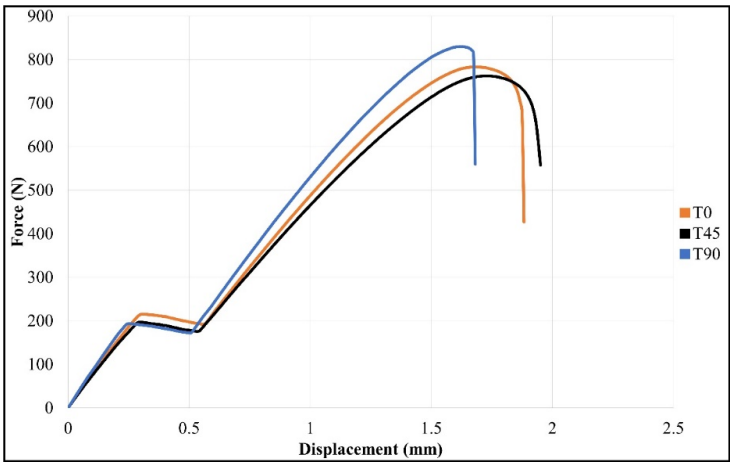

Fig. 13. Effect of Tri – Hexagon infill geometry on tensile behavior in 0° - 45° - 90° orientation.

In terms of maximum displacement, a different trend was observed. The Gyroid infill exhibited the highest deformation capacity, with G45 reaching 3.39 mm, followed by G0 (3.10 mm) and G90 (2.91 mm). This demonstrates the ductile nature of the Gyroid pattern, which can undergo larger elastic deformation due to its isotropic and smoothly interconnected geometry. Such characteristics are beneficial for energy-absorbing or impact-resilient applications. In contrast, the Tri-Hexagon infill resulted in the lowest displacement values among all patterns, with T0 (1.88 mm), T45 (1.95 mm), and T90 (1.68 mm). These findings reflect the more rigid and brittle mechanical response of this infill type, possibly due to its limited ability to distribute stress evenly under tensile loading. This behavior may be suitable for applications requiring dimensional stability but not for that demanding ductility. The Cubic Subdivision infill showed moderate displacement values, with C0 at 2.73 mm, C45 at 2.11 mm, and C90 at 2.14 mm. These results suggest that the Cubic structure offers a balance between rigidity and deformation, behaving less ductile than Gyroid but more flexible than Tri-Hexagon. Overall, the results confirm that the mechanical performance of FDM-printed PLA+ parts is strongly dependent on the interaction between infill geometry and build orientation. The Gyroid infill provided the most favorable performance, offering both high strength and high deformation capacity, particularly in the 90° orientation. The Cubic Subdivision pattern, while less effective than Gyroid, benefitted significantly from increased build orientation, especially in terms of strength. The Tri-Hexagon infill, on the other hand, demonstrated the most rigid and brittle behavior, making it more suitable for applications where dimensional precision and low deflection are prioritized over toughness. These findings emphasize the importance of selecting appropriate infill strategies and orientation settings based on the intended functional requirements of the printed part.

The effects of infill pattern (Gyroid, Tri-Hexagon, Cubic Subdivision) and structure direction (0°, 45°, 90°) on mechanical performance were investigated with Taguchi L9 experimental design. The obtained results are presented in Table 5 and S/N, Means and Std. Dev graph is presented in Fig.15, showing that both factors have different levels of influence on performance.

Fig. 15a shows that the infill pattern factor (Delta: 4.627) has a significant dominant effect on performance compared to the build orientation (Delta: 1.227). Especially, the Gyroid (G) infill pattern provided the highest performance in terms of both mean values and S/N ratios. The Tri-Hexagon (T) infill pattern had a negative effect on performance, while the Cubic (C) pattern had a

moderate effect. In the graphical analysis of the S/N ratios, the delta (difference) value of the infill pattern factor was higher than the build orientation. This reveals that the infill pattern plays a key role in improving the mechanical properties. When the average values are examined (Fig. 15b), the Delta value of the infill pattern (38.8) is lower than the build orientation (62.8). In this case, the effect of the build orientation becomes more prominent compared to the average values. The increased standard deviation observed for specimens printed at 90° orientation suggests a notably higher degree of performance variability compared to the 0° and 45° orientations (Fig. 15c). This variability can affect the reliability and repeatability of FDM-printed parts, especially in critical applications where consistent mechanical behavior is essential. This effect may be due to the increased sensitivity of interlayer bonding when the printed layers are aligned parallel to the loading direction. Minor variations in extrusion temperature, filament feed, or local void distribution could disproportionately affect tensile strength in these orientations. Zhou et al. (2020) Megersa et al. (2024) reported that vertically oriented specimens exhibited a significantly wider distribution in tensile metrics compared to flatly oriented specimens in their study using Taguchi methods. From a practical standpoint, although the 90° orientation yields higher mean tensile strength, ensuring consistent part performance under this orientation necessitates enhanced process control and robust quality assurance protocols—such as tighter thermal regulation, optimized filament flow, and increased replicate testing—to manage variability effectively.

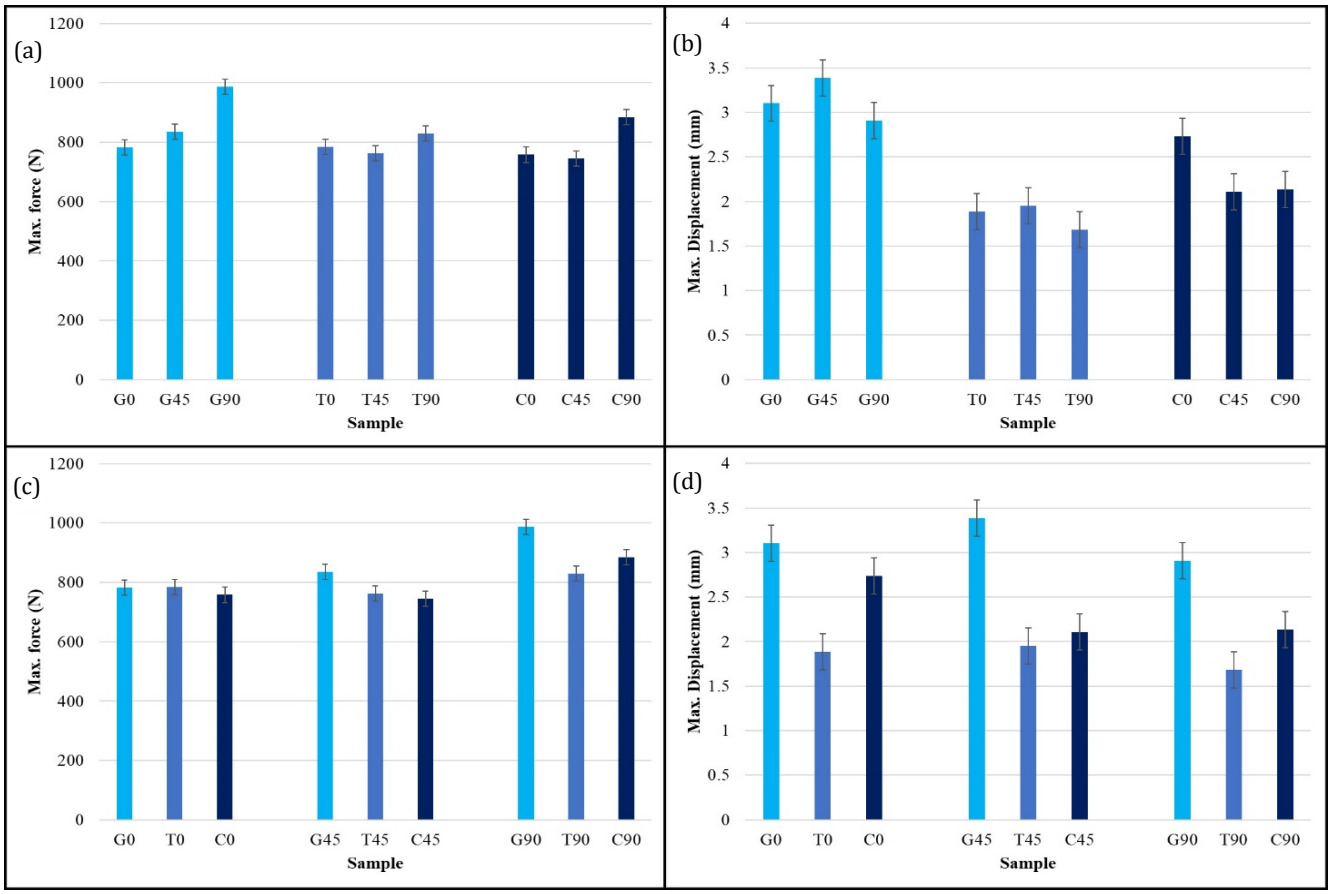

Fig. 14. Effects of infill geometry and build orientation on:
(a, c) Maximum tensile force; (b, d) Maximum displacement.

Table 5. Response table for S/N, means and std. deviations (larger is better).

Level	S/N		Means		Standard deviations	
	Infill pattern	Build orientation	Infill pattern	Build orientation	Infill pattern	Build orientation
1	12.910	11.031	435.8	388.6	611.9	546.0
2	8.283	10.632	397.0	391.9	558.8	550.7
3	10.275	9.805	399.1	451.4	561.1	635.2
Delta	4.627	1.227	38.8	62.8	53.0	89.2
Rank	1	2	2	1	2	1

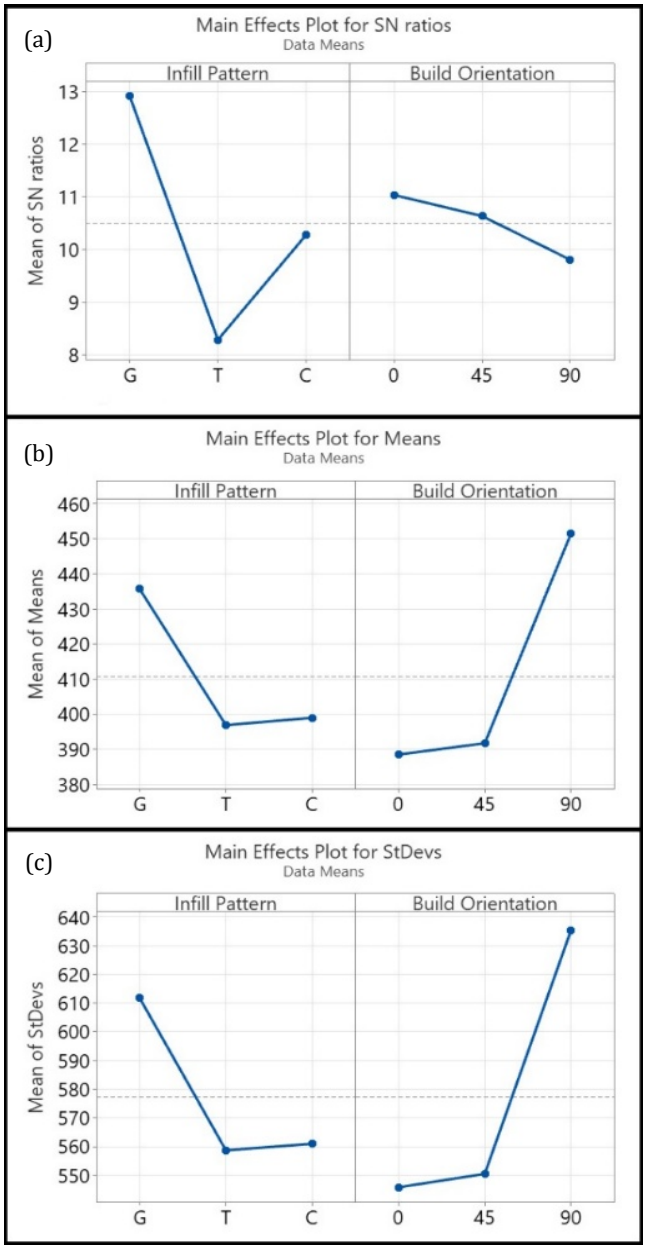

Fig. 15. Main effect plot for:
(a) S/N; (b) Means; (c) Standard deviation.

According to the results of the ANOVA presented in Table 6, the infill pattern explained 86.52% of the total variance (p=0.006) and confirmed its statistical significance; while the contribution of the build orientation remained limited to 6.29% (p=0.285). Standard deviation analyses and related graphs show that the variation increased depending on the build orientation and the standard deviation value increased especially in the 90° orientation. This finding suggests that orientation changes may lead to greater performance differences between parts.

The regression model results are presented in Table 7 and show that there is a high agreement between the experimental data and the obtained values (R^2=92.81%). In the model, it is confirmed that the Gyroid infill pattern has a positive effect on the mechanical performance, while the Tri-Hexagon pattern has a negative effect. As a result, the findings show that the infill pattern has a decisive effect on the mechanical properties, while the build orientation affects the performance variation more. Graphical analysis also shows that the Gyroid infill pattern stands out and the 90° build orientation creates a significant difference in terms of both mean and variation.

The findings show that the infill pattern has a decisive effect on the mechanical properties, while the build orientation affects the performance variation more. Graphical analysis also shows that the Gyroid infill pattern stands out and the 90° build orientation creates a significant difference in terms of both mean and variation.

4. Conclusions

In this study, the effects of different infill patterns (Gyroid, Tri-Hexagon, Cubic Subdivision) and build orientations (0°, 45°, 90°) on the mechanical performance of parts manufactured with PLA material using the FDM method were systematically investigated using the Taguchi L9 experimental design. The findings show that both factors affect the mechanical performance to different extents, and the detailed results are presented below:

Table 6. Analysis of variance.

Source	DF	Seq SS	Contribution	Adj SS	Adj MS	F-value	P-value
Infill pattern	2	32.320	86.52%	32.320	16.1600	24.07	0.006
Build orientation	2	2.349	6.29%	2.349	1.1743	1.75	0.285
Error	4	2.685	7.19%	2.685	0.6713	–	–
Total	8	37.354	100.00%	–	–	–	–

Table 7. Model summary

S	R-sq	R-sq (adj)	PRESS	R-sq (pred)	AICc	BIC
0.819330	92.81%	85.62%	13.5939	63.61%	68.66	27.84

- The Gyroid infill pattern exhibited superior mechanical properties, achieving the highest tensile strength (987.3 N) at 90° build orientation, while the 45° orientation provided the highest ductility (3.39 mm). This reflects the anisotropic behavior of FDM-printed parts and highlights a trade-off between strength and deformation capacity.
- The Tri-Hexagon pattern showed the lowest performance, with brittle fracture behavior, while the Cubic Subdivision pattern demonstrated intermediate results.
- A 90° build orientation consistently enhanced tensile strength across all infill patterns, particularly for Gyroid, due to improved interlayer adhesion and alignment with the load direction.
- Specimens printed at 0° and 45° displayed lower strength and varied fracture modes, highlighting the anisotropic nature of FDM-printed parts.
- ANOVA revealed that the infill pattern accounted for 86.52% of the variance in mechanical performance, confirming its dominant role.
- Build orientation contributed only 6.29%, though its interaction with infill geometry influenced ductility and failure modes.
- The Gyroid infill pattern at 90° orientation demonstrated the highest tensile strength together with notable ductility, making it a promising choice for lightweight structural components in aerospace applications and for automotive parts, including interior trim components.
- The superior energy absorption capacity of the Gyroid structure also indicates its potential use in biomedical implants, medical splints, and protective devices where controlled deformation is advantageous.

This study is limited to a single polymer material (PLA+) and a specific set of infill patterns. Future research should investigate other materials, including biocompatible and high-performance polymers, explore a broader range of infill strategies and densities, and evaluate performance under varied environmental conditions (e.g., temperature, humidity) and loading scenarios (e.g., fatigue, impact). Such studies would help establish a more comprehensive understanding of the applicability of these findings in diverse engineering contexts.

Acknowledgements

The authors would like to thank YÜTAM from Erzurum Technical University because of providing access to their devices and laboratory facilities for this study.

Funding

The authors received no financial support for the research, authorship, and/or publication of this manuscript.

Conflict of Interest

The authors declared no potential conflicts of interest with respect to the research, authorship, and/or publication of this manuscript.

Author Contributions

All of the authors made substantial contributions to conception and design, or acquisition of data, or analysis and interpretation of data; were involved in drafting the manuscript or revising it critically for important intellectual content; and gave final approval of the version to be published.

Data Availability

The datasets created and/or analyzed during the current study are not publicly available, but are available from the corresponding author upon reasonable request.

REFERENCES

Abdullah MA, Abbas TF (2023). Investigation and prediction of the impact of FDM process parameters on mechanical properties of PLA prints. *Engineering and Technology Journal*, 41(12), 1465-1473.

Adragna PA, Giraud-Moreau L, Madugula SK (2021). Continuous extrusion printing: Influence of the FDM printing trajectory on thin-walled 3D printed part performance. *Journal of Material Sciences & Engineering*, 10(7), 1-4.

Akhoundi B, Behravesh AH (2019). Effect of filling pattern on the tensile and flexural mechanical properties of FDM 3D printed products. *Experimental Mechanics*, 59(6), 883-897.

Alafaghani A, Qattawi A (2018). Investigating the effect of fused deposition modeling processing parameters using Taguchi design of experiment method. *Journal of Manufacturing Processes*, 36, 164-174.

Alemayehu DB, Todoh M (2024). Enhanced energy absorption with bioinspired composite triply periodic minimal surface gyroid lattices fabricated via fused filament fabrication (FFF). *Journal of Manufacturing and Materials Processing*, 8(3), 86.

Ambade V, Rajurkar S, Awari G, Yelamasetti B, Shelare S (2023). Influence of FDM process parameters on tensile strength of parts printed by PLA material. *International Journal on Interactive Design and Manufacturing*, 19, 573-584.

Arora PK, Shrivastava Y, Kumar H (2023). Optimising FDM printing parameters for improved tensile properties in 3D printed ASTM D638 standard samples. *Australian Journal of Mechanical Engineering*, 23(2), 277-290.

Casavola C, Cazzato A, Moramarco V, Pappalettere C (2016). Orthotropic mechanical properties of fused deposition modelling parts described by classical laminate theory. *Materials & Design*, 90, 453-458.

Dawood LL, AlAmeen ES (2024). Influence of infill patterns and densities on the fatigue performance and fracture behavior of 3D-printed carbon fiber-reinforced PLA composites. *AIMS Materials Science*, 11(5), 833-857.

Dezaki ML, Mohd Ariffin MKA (2020). The effects of combined infill patterns on mechanical properties in FDM process. *Polymers*, 12(12), 1-20.

Equbal A, Murmu R, Kumar V, Equbal MA (2024). A recent review on advancements in dimensional accuracy in fused deposition modeling (FDM) 3D printing. *AIMS Materials Science*, 11(5), 950-990.

Huang SH, Liu P, Mokasdar A, Hou L (2013). Additive manufacturing and its societal impact: A literature review. *International Journal of Advanced Manufacturing Technology*, 67(5), 1191-1203.

Jasim MF, Abbas TF, Huayier AF (2022). The effect of infill pattern on tensile strength of PLA material in fused deposition modeling (FDM) process. *Engineering and Technology Journal*, 40(12), 1723-1730.

Khaderi SN, Deshpande VS, Fleck NA (2014). The stiffness and strength of the gyroid lattice. *International Journal of Solids and Structures*, 51(23), 3866-3877.

Laureto JJ, Pearce JM (2018). Anisotropic mechanical property variance between ASTM D638-14 type I and type IV fused filament fabricated specimens. *Polymer Testing*, 68, 294-301.

Le L, Rabsatt MA, Eisazadeh H, Torabizadeh M (2022). Reducing print time while minimizing loss in mechanical properties in consumer FDM parts. *International Journal of Lightweight Materials and Manufacture*, 5(2), 197-212.

Marşavina L, Vălean C, Mărghitaş M, Linul E, Razavi N, Berto F, Brighenti R (2022). Effect of the manufacturing parameters on the tensile and fracture properties of FDM 3D-printed PLA specimens. *Engineering Fracture Mechanics*, 274, 108766.

Megersa GK, Sitek W, Nowak AJ, Tomašić N (2024). Investigation of the influence of fused deposition modeling 3D printing process parameters on tensile properties of polylactic acid parts using the Taguchi method. *Materials*, 17(23), 5951.

Rahman MM, Sultana J, Rayhan SB, Ahmed A (2023). Optimization of FDM manufacturing parameters for the compressive behavior of cubic lattice cores: An experimental approach by Taguchi method. *International Journal of Advanced Manufacturing Technology*, 129(3), 1329-1343.

Rajpurohit SR, Dave HK (2018). Effect of process parameters on tensile strength of FDM printed PLA part. *Rapid Prototyping Journal*, 24(8), 1317-1324.

Silva C, Pais AI, Caldas G, Gouveia BPPA, Alves JL, Belinha J (2021). Study on 3D printing of gyroid-based structures for superior structural behaviour. *Progress in Additive Manufacturing*, 6(4), 689-703.

Solomon IJ, Sevvel P, Gunasekaran J (2020). A review on the various processing parameters in FDM. *Materials Today: Proceedings*, 37(2), 509-514.

Tandon S, Kacker R, Sudhakar KG (2021). Quantitative strength analysis for 3D-printed specimens in a tri-hexagon pattern. *Proceedings of the Institution of Mechanical Engineers, Part C: Journal of Mechanical Engineering Science*, 235(24), 7685-7698.

Tandon S, Kacker R, Singh SK, Gautam SS, Tamang SK (2025). Multi-objective optimization of mechanical properties of additively manufactured tri-hexagon pattern specimens using machine learning algorithms. *Progress in Additive Manufacturing*, 10(5), 3659-3672.

Taşdemir V (2024). Investigation of the effects of the number of shells, raster angle, extrusion ratio, and path width on printed polylactic acid parts with fused deposition modeling 3D printer. *Journal of Materials Engineering and Performance*, 33, 11888-11898.

Vălean C, Marşavina L, Mărghitaş M, Linul E, Razavi J, Berto F (2020). Effect of manufacturing parameters on tensile properties of FDM printed specimens. *Procedia Structural Integrity*, 26, 313-320.

Vanaei S, Rastak M, El Magri A, Vanaei HR, Raissi K, Tcharkhtchi A (2023). Orientation-dependent mechanical behavior of 3D printed polylactic acid parts: An experimental–numerical study. *Machines*, 11(12), 1086.

Yao T, Deng Z, Zhang K, Li S (2019). A method to predict the ultimate tensile strength of 3D printing polylactic acid (PLA) materials with different printing orientations. *Composites Part B: Engineering*, 163, 393-402.

Zhao Y, Chen Y, Zhou Y (2019). Novel mechanical models of tensile strength and elastic property of FDM AM PLA materials: Experimental and theoretical analyses. *Materials & Design*, 181, 108089.

Zhou L, Miller J, Vezza J, Mayster M, Raffay M, Justice Q, Al Tamimi Z, Hansotte G, Sunkara LD, Bernat J (2024). Additive manufacturing: A comprehensive review. *Sensors*, 24(9), 2668.

Challenge Journal of Structural Mechanics

Research Article

Performance investigation of a mixed slab building with beam and ribbed slabs

Burak Yüksek [a], Recep Tuğrul Erdem [a], Tolga Yılmaz [b], Hasan Selim Şengel [c,*]

[a] *Department of Civil Engineering, Manisa Celal Bayar University, 45140 Manisa, Türkiye*
[b] *Department of Civil Engineering, Konya Technical University, 42250 Konya, Türkiye*
[c] *Department of Civil Engineering, Eskişehir Osmangazi University, 26480 Eskişehir, Türkiye*

ABSTRACT

Over time deterioration in material properties, unauthorized modifications, or construction defects can negatively affect the seismic behavior of structural members. Therefore, the in-situ identification and performance analysis of reinforced concrete elements, carried out to ensure the safety of the existing building stock, have become a fundamental part of examining structural characteristics and developing disaster risk reduction strategies. In this study, the structural performance analysis of an existing reinforced concrete building with a mixed slab system was conducted by using the STA4CAD V13.1 software. For this purpose, nonlinear pushover analysis was performed for each seismic direction. As the existing reinforced concrete building did not satisfy the requirements for the single-mode method prescribed in TBDY (2018), a multi-mode pushover analysis was conducted for the structure. Based on the results of nonlinear multi-mode pushover analysis, the damage states of the structural members were determined, and the performance level of the structure was evaluated. The targeted performance level of controlled damage, as defined in the Turkish Building Earthquake Code-2018 TBEC (2018), could not be achieved for the analyzed residential-type reinforced concrete building. However, the collapse prevention performance level was determined due to the damage occurrence in the structural elements.

ARTICLE INFO

Article history:
Received – July 21, 2025
Revision requested – August 18, 2025
Revision received – August 26, 2025
Accepted – September 8, 2025

Keywords:
Earthquake
Existing building
Mixed slab
Non-linear analysis
Structural system safety

Citation: Yüksek B, Erdem RT, Yılmaz T, Şengel HS (2025). Performance investigation of a mixed slab building with beam and ribbed slabs. *Challenge Journal of Structural Mechanics*, 11(4), 215–228.

1. Introduction

Due to its geological location, Türkiye is situated on the Alpine-Himalayan earthquake belt, one of the most active seismic zones in the world. This condition exposes the country to significant seismic hazards. Numerous active fault lines are distributed across the country, with major seismic sources such as the North Anatolian Fault, East Anatolian Fault, and active fault systems in Western Anatolia capable of generating earthquakes that can cause widespread damage. These fault lines have historically produced destructive earthquakes, resulting in severe loss of life and property. The fact that a large portion of Türkiye's settlements are located in close proximity to active fault zones further increases the seismic risk and renders structural safety a top priority. In order to mitigate the impacts of earthquakes, one of the leading natural disasters causing significant loss of life and property, it is of great importance not only to design new buildings in earthquake-prone regions such as Türkiye to be earthquake-resistant but also to assess the structural safety of existing buildings. Therefore, in the context of addressing seismic hazards, the condition of the existing building stock, urban planning policies, and disaster management strategies must be addressed through an integrated and comprehensive approach.

* *Corresponding author*. Tel.: +90-222-239-3750 ; Fax: +90-222-229-0535 ; E-mail address: ssengel@ogu.edu.tr (H. S. Şengel)
ISSN: 2149-8024 / DOI: https://doi.org/10.20528/cjsmec.2025.04.004

Earthquakes that have occurred during both the historical and instrumental periods clearly reveal the severity of Türkiye's seismic characteristics. This reality has necessitated the revision of seismic codes in line with scientific data. In particular, the 1999 Marmara Earthquake exposed serious structural deficiencies and led to significant regulatory changes through the issuance of the 2007 Earthquake Code for Buildings to be Constructed in Seismic Zones. In the following years, considering advances in scientific research, engineering practices, and the increasing availability of seismic records, the existing code was comprehensively revised, resulting in the Turkish Building Earthquake Code-2018 TBEC (2018), which came into effect on January 1, 2019. The new code incorporates the performance-based design approach and includes detailed provisions not only for the design of new buildings but also for the evaluation and, when necessary, retrofitting of existing structures. It is regarded as a significant step toward enhancing earthquake safety. Additionally, the Türkiye Earthquake Hazard Map, which expresses the seismic hazard of a given location in terms of peak ground acceleration based on geographical coordinates, was issued separately and implemented on a different date.

Structures subjected to seismic effects are exposed to sudden and significant lateral forces. The compliance and load-bearing capacities of existing reinforced concrete elements, particularly columns, beams, and slabs, with current seismic codes play a decisive role in the seismic performance of buildings. Reinforced concrete structural elements are the fundamental components responsible for safely transferring a building's vertical and horizontal loads to the ground. Elements such as columns, beams, slabs, and shear walls work together to ensure the strength and stiffness of the structure. The load transfer between these elements forms the basis of the structural design, improper load transmission can lead to significant deficiencies in structural performance. Therefore, the sizing of reinforced concrete elements, reinforcement detailing, and the design of connection regions must be carried out in accordance with current codes and standards. A properly designed structural system contributes to maintaining the integrity of the building not only under service loads but also under extreme loading conditions such as earthquakes. Compliance with design principles is essential for the construction of structures that are both safe and economically efficient.

Reinforced concrete slabs are an integral part of the structural system, ensuring the safe transfer of loads to vertical load-bearing elements such as beams and columns. They also contribute to the horizontal stiffness of the structure, significantly influencing its behavior under lateral loads such as those generated by earthquakes. Designing slabs with adequate thickness and proper reinforcement is critical for effective load transfer and for ensuring the integral action of the structural system. Within the scope of TBEC (2018), irregularities in plan, specifically type A2 irregularities referred to as slab discontinuities, are associated with the presence of openings or voids that may compromise the validity of the rigid diaphragm assumption in the slab plane TBEC (2018). Such discontinuities can lead to uncertainties in horizontal load transfer and reduced structural performance. Therefore, these effects must be taken into account during slab design, and the seismic safety of the structure should be thoroughly evaluated. Researchers have investigated the effects of voids on the slab behavior in the literature (Kalib 2021; Khajehdehi and Panahshahi 2016; Özbayrak 2021).

Structural performance refers to whether a building's behavior under a given level of loading remains within acceptable limits, and it is particularly evaluated in terms of meeting the performance level targets defined in seismic design codes. In the assessment of the seismic safety of buildings, nonlinear analysis methods are preferred as they provide more realistic results (Erdem 2016; Ricci et al. 2018; Ozkul et al. 2019; Lin and Chuang 2023; Kuria and Kegyes-Brassai 2023; Gupta and Gupta 2024; Ergin and Seçer 2025). One such method, nonlinear pushover analysis, enables the identification of the structure's lateral load capacity and collapse mechanism by revealing plastic hinge formations and displacement capacities. Therefore, nonlinear pushover analysis has become widely used in recent years for the performance evaluation of existing buildings, due to its practicality in engineering applications and its compatibility with code-based requirements (Golghate et al. 2013; Joyner and Sasani 2020; Bento and Simões 2021; Sullivan et al. 2021; Erdem and Karal 2022; Erdem and Uyan 2025).

A mixed slab system refers to a structural configuration in which different types of slabs such as one-way ribbed, flat, waffle, or conventional beam-supported slabs are used within the same building. These systems are often encountered in residential buildings where architectural design plays a prominent role. Due to the varying stiffness, mass, and load transfer characteristics of different slab types, the overall structural behavior becomes more complex and difficult to accurately represent using conventional analysis methods. This complexity hinders the reliable assessment of the overall performance of the load-bearing system. Therefore, in existing buildings with mixed slab systems, nonlinear analysis methods are preferred, as they offer a more realistic and reliable representation of structural behavior under seismic effects (Eşki et al. 2020; Mene and Nilawar 2022; Hulke and Solanke 2023; Shende et al. 2024).

In this study, the structural safety of an existing residential type reinforced concrete building with a mixed slab system was investigated. The STA4CAD V13.1 (2023) software was utilized to assess the seismic performance of the structure. As the analysis method, nonlinear incremental pushover analysis was applied to the building. Initially, a single-mode pushover analysis was performed. However, according to TBEC (2018), the mass participation ratio of the dominant vibration mode in the direction considered must exceed 0.70 for the single-mode pushover method to be valid. The analysis results showed that the mass participation ratio remained below 0.70. Furthermore, the torsional irregularity coefficient must be less than 1.40, as stipulated by the code. In the examined building, neither of these two conditions was satisfied. Therefore, a multi-mode pushover analysis was applied. Based on the performance analysis conducted for each seismic direction, the damage states of

the structural members were identified, and the seismic performance level of the existing building was subsequently determined. Within the scope of this study, both the investigation of a reinforced concrete building with a mixed slab system and the implementation of multi-mode pushover analysis are considered to offer valuable contributions to the literature.

2. Materials and Method

As part of this study, the existing building whose seismic performance was investigated is a six-story residential reinforced concrete structure constructed in 1995. The building has a total floor area of 274.17 m^2 and includes one partial basement floor, one ground floor, three typical floors, and one roof floor. The story heights are 250 cm in the basement, 302 cm on the ground floor, 270 cm on the first and second floors, 302 cm on the third floor, and 260 cm in the roof floor. Based on the geotechnical investigation conducted for the building, the local soil class was identified as ZC, corresponding to very dense sand, gravel, and stiff clay layers. Examination of the slab system revealed the use of a mixed slab system. Ribbed (hollow block) slabs were used on the ground and third floors, while beam-and-slab systems were employed on the other floors. The front elevation of the building is shown in Fig. 1.

Following the on-site verification of the building's structural drawings, core sampling was carried out to determine the concrete compressive strength. For this purpose, a total of 13 core samples were extracted from the building. Three samples were taken from the ground floor, while two samples were taken from each of the remaining floors. Laboratory results were obtained from axial compression tests conducted on the core samples. The test results for each sample are presented in Table 1. In the table, the value F_d represents the correction factor for core diameter, and F_{kd} indicates the corrected compressive strength of the core sample.

Fig. 1. Front elevation of the residential building.

Table 1. Experimental results of concrete samples.

Sample no	Floor	Element no	Diameter and height of the sample (mm)	Test result (MPa)	F_d (MPa)	F_{kd} (MPa)
1	Basement	S107	94/94	11.01	1.03	11.3
2	Basement	P104	94/94	10.16	1.03	10.5
3	Ground	S217	94/94	9.66	1.03	9.9
4	Ground	S228	94/94	7.81	1.03	8.0
5	Ground	1S222	94/94	8.06	1.03	8.3
6	1. Floor	S317	94/94	9.88	1.03	10.2
7	1. Floor	S318	94/94	13.58	1.03	14.0
8	2. Floor	S417	94/94	16.06	1.03	16.5
9	2. Floor	S418	94/94	13.05	1.03	13.4
10	3. Floor	S517	94/94	8.25	1.03	8.5
11	3. Floor	S518	94/94	13.24	1.03	13.6
12	4. Floor	S617	94/94	8.48	1.03	8.7
13	4. Floor	S618	94/94	12.81	1.03	13.2

According to the laboratory test results conducted on identical core samples, as detailed in Table 1, the average compressive strength was calculated as 11.50 MPa, with a standard deviation of 2.70 MPa. The difference between these two values is 8.80 MPa. By applying a reduction factor of 0.85 to the average compressive strength, the final value was determined to be 9.80 MPa. In accordance with Article 15.2.5.3 of TBEC (2018), the concrete compressive strength to be used in the structural analysis software for all load-bearing elements was defined as C10 (10 MPa).

Following the determination of the compressive strength of concrete, a reinforcement detection study was conducted to identify the existing reinforcement. As an example, the rebar exposure process performed on one beam and one column is presented in Fig 2.

Fig. 2. Exposure of rebars.

The column dimensions used in the structural system are 25×50 cm, 25×60 cm, 30×60 cm, 25×100 cm, and 25×125 cm. The dimensions of columns S06, S07, S08, and S18 vary on the roof floor. Shear walls are present as vertical load-bearing elements in the basement floors and around the stairwell. Additionally, two shear walls are located around the elevator shaft. The dimensions of these elements are 25×200 cm and 20×290 cm. Columns with varying cross-sectional dimensions and their reinforcement layouts are presented in Fig. 3.

To determine the cross-sectional loss in the reinforcement of reinforced concrete columns, rebar exposure tests were conducted. As an example, the structural elements on the ground floor where reinforcement investigation was performed are marked in Fig. 4. Based on the investigation, the column reinforcements were identified as S420 ribbed reinforcement steel. Additionally, no signs of corrosion were observed in the column reinforcements.

The longitudinal reinforcement details of the reinforced concrete columns are presented in Table 2. Double-legged vertical stirrups were used as transverse reinforcement in the columns. The stirrups have a diameter of 8 mm and are spaced at 20 cm intervals. Additionally, it was determined that the stirrups do not have 135-degree hooks; instead, the hooks are implemented at 90 degrees.

After determining the column dimensions and reinforcement, the characteristics of the beams in the building were evaluated. According to the existing project, longitudinal reinforcement in the beams consists of 2Φ12 bars on floors with slab systems and 3Φ12, 4Φ12, or 5Φ12 bars on floors with hollow block slab systems. It was observed that the stirrup hooks used as transverse reinforcement were implemented at 90 degrees. Additionally, no stirrup confinement was provided at the beam end regions. One beam per floor was subjected to rebar exposure, and no signs of corrosion were detected in these beams' reinforcement. However, differences were noted between the beam reinforcement shown in the project and the reinforcement observed during the rebar exposure tests. The details of the beams subjected to rebar exposure are presented in Table 3. Additionally, as an example, the reinforcement layout of three beams located at grid line 6 on the ground floor is shown in Fig. 5.

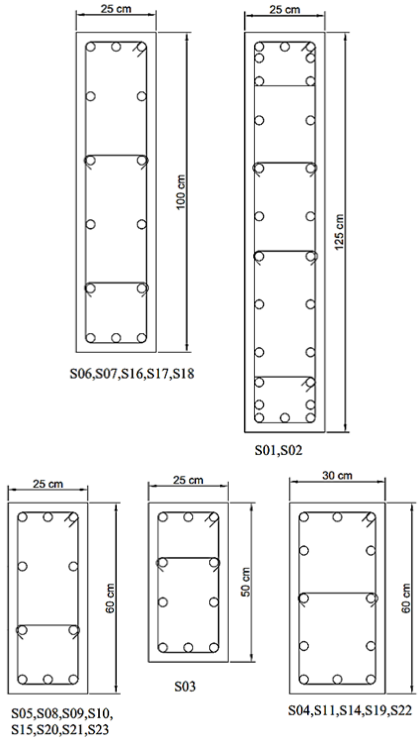

Fig. 3. Column sections.

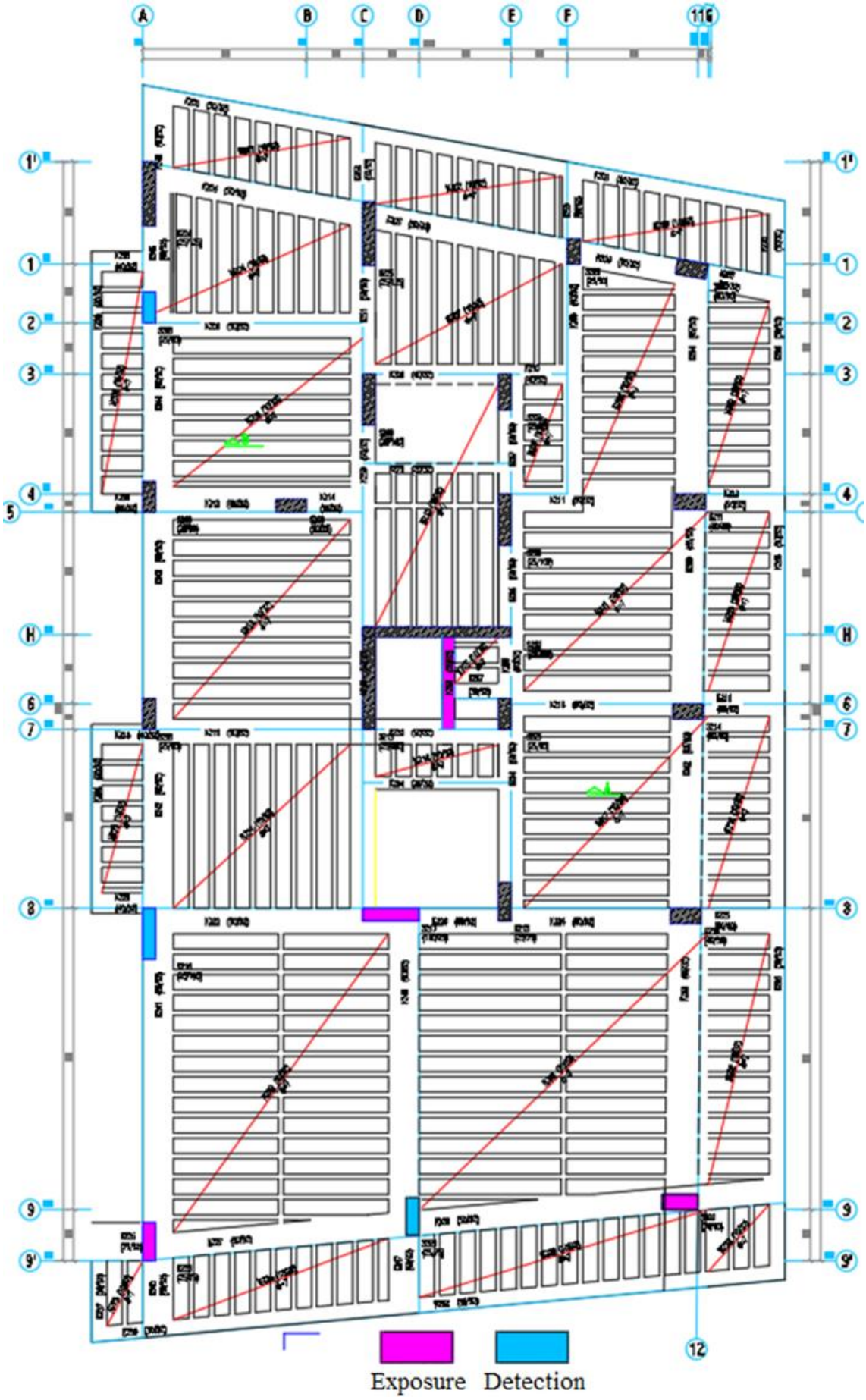

Fig. 4. Exposure and detection of rebars in ground floor.

Table 2. Dimension and reinforcement details of the columns.

Column no	Dimensions (cm)	Longitudinal reinforcement
Basement columns		
SB05, SB08, SB09, SB15	25×60	10Φ14
SB06	25×100	14Φ16
SB01, SB02	25×125	6Φ14 + 12Φ12
Ground floor columns		
SZ03	25×50	10Φ14
SZ05, SZ08, SZ09, SZ10, SZ15, SZ20, SZ21, SZ23	25×60	10Φ14
SZ04, SZ11, SZ14, SZ19, SZ22	30×60	12Φ14
SZ06, SZ07, SZ16, SZ17, SZ18	25×100	14Φ16
SZ01, SZ02	25×125	6Φ14 + 12Φ12
Roof floor columns		
SZ08	25×50	10Φ14
SZ06, SZ07, SZ18, SZ10, SZ15, SZ23	25×60	10Φ14
SZ14	30×60	12Φ14
SZ16, SZ17	25×100	14Φ16

Table 3. Dimension and reinforcement details of the beams.

No	Floor	Beam	Beam dimensions (cm)	Existing reinforcement (S420)			Project reinforcement (S420)		
				Longitudinal reinforcement (S420)		Stirrups (cm)	Longitudinal reinforcement (S420)		Stirrups (cm)
1	Basement	K101	20×50	Bottom	3Φ14	8Φ19	Top Bottom	1Φ12 2Φ14	Φ8/20/10
2	Ground	K253	25×32	Bottom	3Φ12	8Φ14	Top Bottom	2Φ12 3Φ12	Φ8/20/10
3	1. Floor	K314	20×50	Bottom	8Φ17	8Φ17	Top Bottom	1Φ12 2Φ14	Φ8/20/10
4	2. Floor	K414	25×40	Bottom	8Φ12	8Φ12	Top Bottom	2Φ12 2Φ12	Φ8/16/8
5	3. Floor	K514	20×60	Bottom	8Φ25	8Φ25	Top Bottom	2Φ12 2Φ12	Φ8/16/8

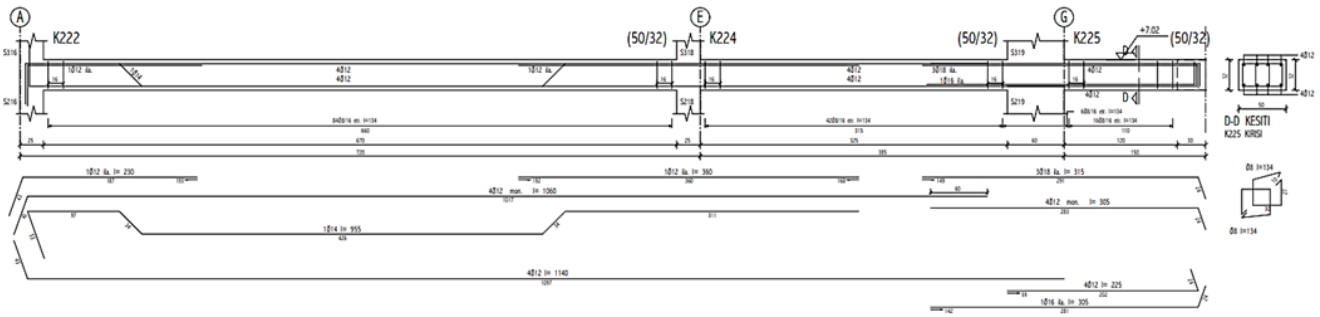

Fig. 5. Reinforcement details of K222, K224, and K225 beams.

An examination of the reinforced concrete beam-and-slab floor thickness revealed that the slab thickness is 12 cm on all floors and 15 cm on the roof floor. The hollow block slabs on the ground and third floors have a thickness of 7 cm, with rib heights measuring 32 cm. The live load value for the slabs was taken as 2.00 kN/m^2 (TS-498 1997). Additionally, exterior walls were modeled as 20 cm thick and interior walls as 10 cm thick in the structural analysis software. The beam-and-slab and ribbed slab systems used in the existing building are illustrated on the floor formwork plans shown in Figs. 6 and 7.

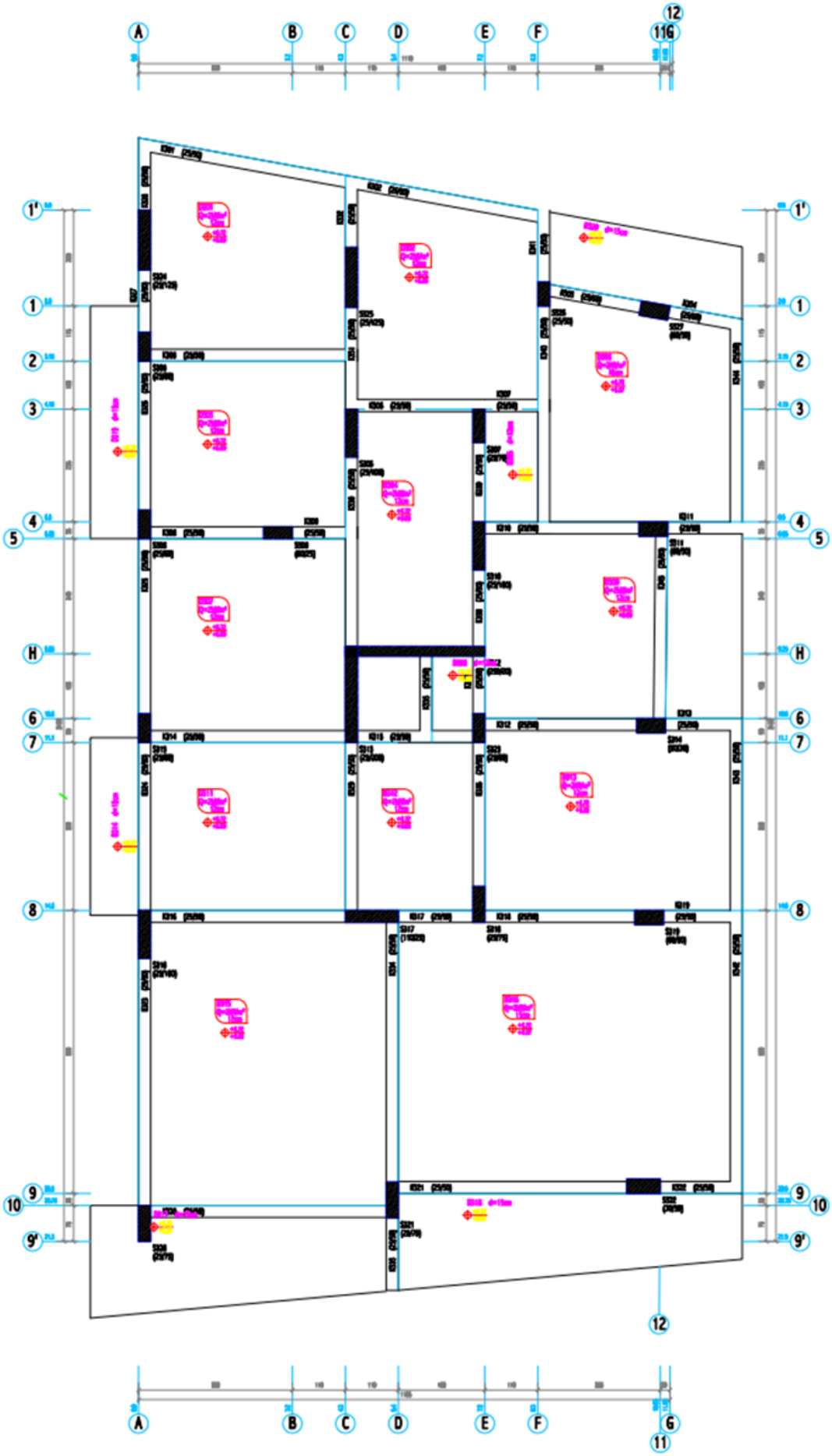

Fig. 6. Formwork plan of 1st floor.

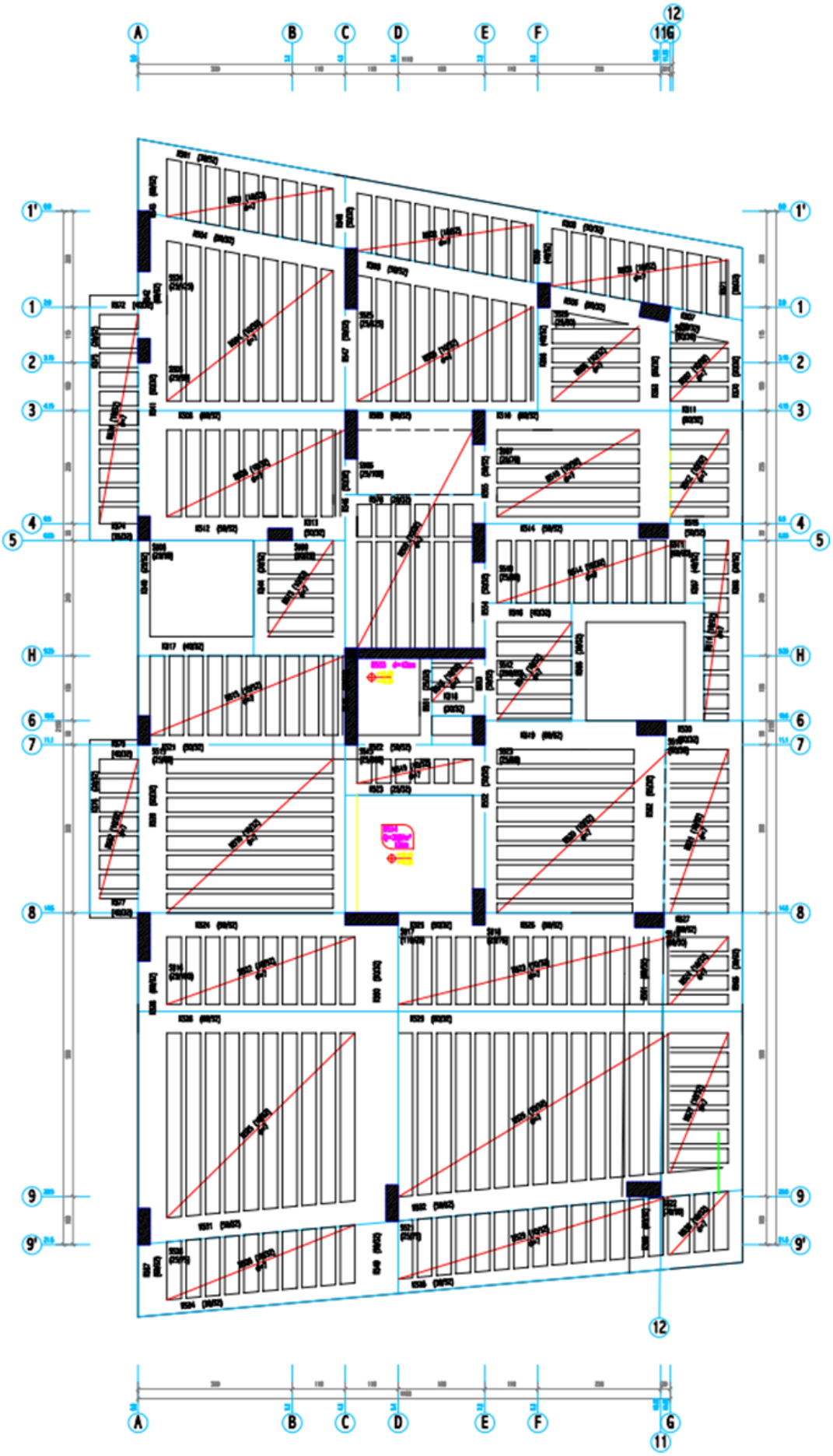

Fig. 7. Formwork plan of 3rd floor.

3. Performance Analysis

In this section, the structural performance analysis of the existing reinforced concrete building was conducted in accordance with TBEC (2018). The building was first modeled digitally using the STA4CAD V13.1 (2023) software. The beam elements and the three-dimensional solid model of the building are shown in Fig. 8.

Using the Türkiye Seismic Hazard Map application prepared for TBEC (2018), the building's location information, including latitude and longitude details, seismic ground motion level, and local soil classification were defined. The seismic ground motion level was applied as "DD2", corresponding to a 10% probability of exceedance in 50 years (return period of 475 years).

Following the modeling process, the building's location, soil, and seismic level data were entered into the system using the TDTH application, and the values obtained for the DD2 earthquake level from the interactive web application are presented in Table 4.

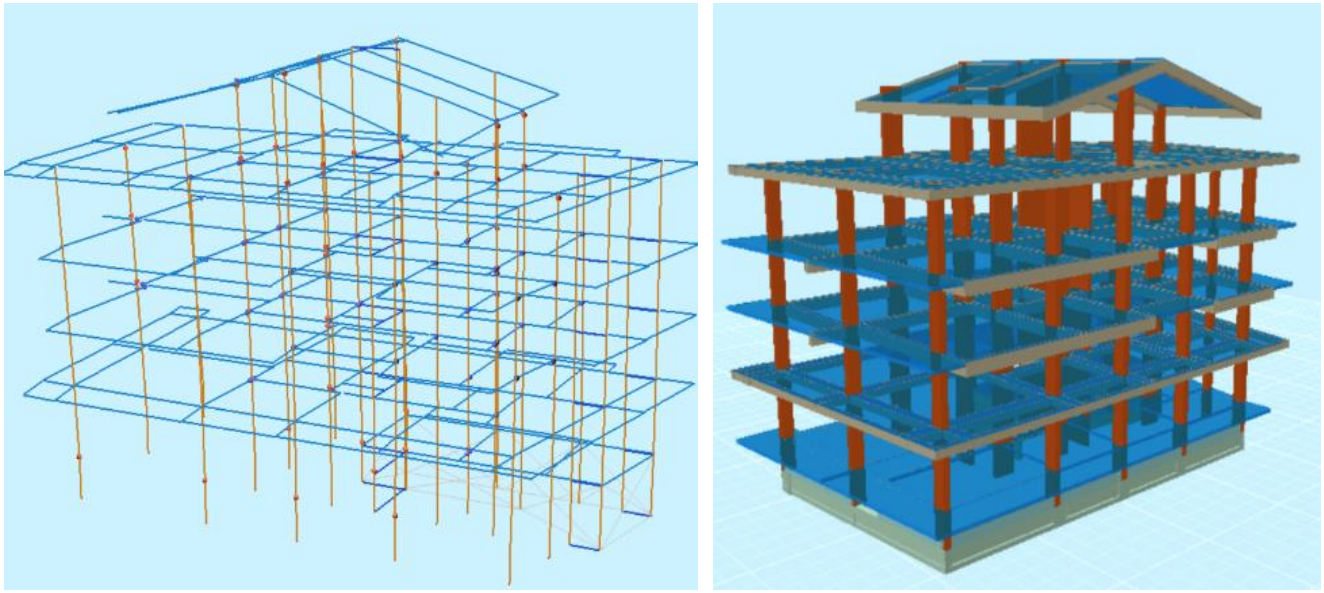

Fig. 8. Existing building model.

Table 4. Spectral parameters.

Parameter	Value
Maximum ground acceleration, PGA	0.409
Maximum ground velocity, PGV (cm/s)	23.102
Short-period spectral acceleration coefficient, S_s	0.977
Spectral acceleration coefficient for 1.0 s period, S_1	0.234
Short-period design spectral acceleration coefficient, S_{ds}	1.172
Design spectral acceleration coefficient for 1.0 s period, S_{d1}	0.351

Since the existing building is used for residential purposes, it falls under the "other buildings" category according to TBEC (2018). Therefore, the building use class was assigned as 3, and the building importance factor was taken as 1.0. The fundamental periods of the building were determined as 0.88 seconds and 0.71 seconds in the x and y directions, respectively. For the building's performance analysis, a deformation-based assessment and design approach was applied, requiring the achievement of the controlled damage performance objective for the DD2 earthquake level.

The global performance limits of are determined based on the damage levels observed in structural elements as a result of nonlinear pushover analysis, and these limits are largely consistent across various seismic design codes. As illustrated in Fig. 9, these performance limits defined within the internal force–deformation relationship are categorized as Immediate Occupancy (IO), Life Safety (LS), and Collapse Prevention (CP). At the Immediate Occupancy level, minor cracking may be observed in structural elements, yet the overall integrity and functionality of the structure are preserved. The Life Safety limit is characterized by more extensive damage, with certain elements exhibiting significant deformation within designated damage zones, yet structural collapse is still avoided. The Collapse Prevention limit represents a near-collapse condition, where severe damage compromises the structural system's capacity to resist further loading. Exceeding this threshold results in global structural collapse TBEC (2018).

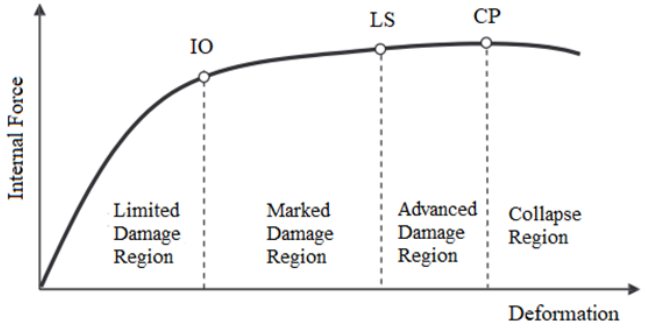

Fig. 9. Damage regions.

Recent studies in earthquake engineering have revealed the limitations of traditional force-based design approaches, leading to an increasing shift toward displacement-based design methods. This approach provides a more appropriate framework for evaluating the realistic responses of structures to seismic demands. Particularly in determining the seismic performance of newly designed or existing reinforced concrete buildings, nonlinear static or dynamic analysis methods which yield more reliable results compared to linear analysis techniques have become prominent. However, nonlinear static analysis methods are more frequently preferred in practical engineering applications due to their ease of implementation, reduced computational effort, and compatibility with widely used engineering software. This preference highlights the prominence of static methods in performance-based assessments of existing structures.

The nonlinear incremental pushover analysis is a widely used method in performance-based seismic evaluation of structures. In this approach, lateral loads are incrementally applied to a structural model until a target displacement is reached, allowing the assessment of the structure's behavior beyond the elastic range. The analysis captures the sequence of yielding in structural elements and provides insight into damage progression and failure mechanisms.

One of the main advantages of the nonlinear pushover analysis is its relative simplicity compared to fully nonlinear dynamic analyses, while still offering valuable information about global and local performance levels. It enables engineers to estimate the capacity curve of the structure, determine the target performance points, and evaluate the distribution of possible damage regions, making it an effective and practical tool for the seismic assessment of both new and existing buildings. The modal capacity diagram is obtained using the coordinate transformation defined in TBEC (2018). As shown in Fig. 10, the modal capacity diagram is plotted together with the earthquake spectrum.

Nonlinear pushover analyses were performed in both directions of the existing building for the relevant seismic level. Target displacement values were determined as 7.9 cm and 6.6 cm for the *x* and *y* directions, respectively. The damage states of the structural system elements were evaluated as the building was pushed up to the defined performance points. The base shear force–roof displacement curves for the building are presented in Figs. 11 and 12.

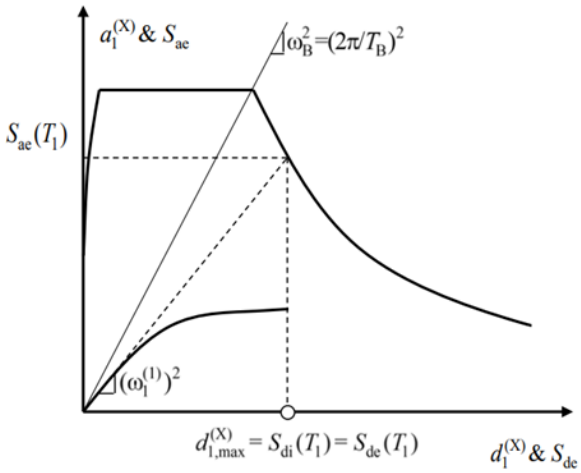

Fig. 10. Modal capacity diagram.

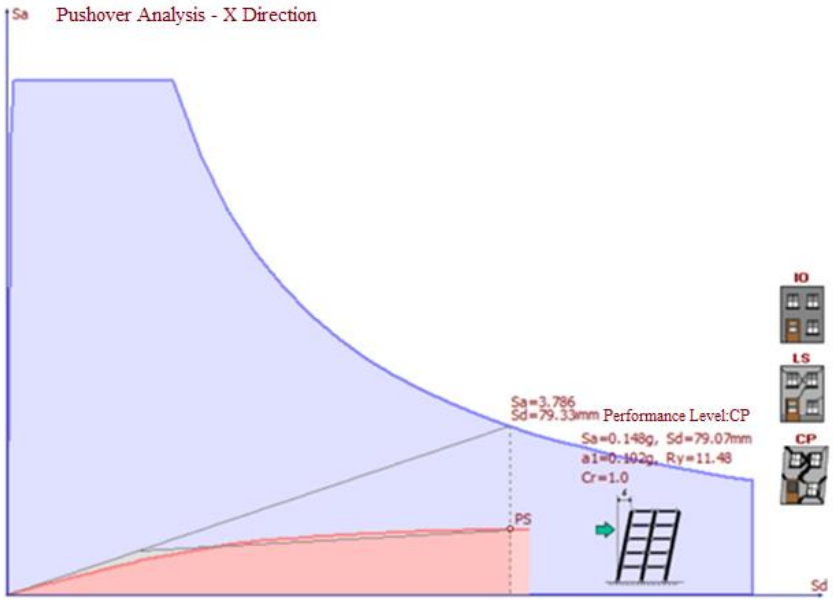

Fig. 11. Pushover curve in *x* direction.

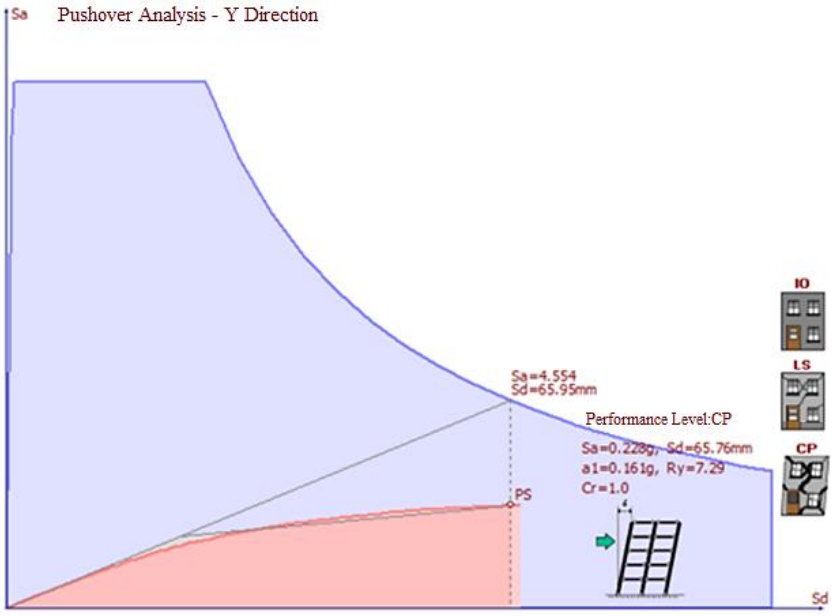

Fig. 12. Pushover curve in *y* direction.

The mass participation ratios were calculated as 66.9% and 69.4% in the x and y directions, respectively. These values fall below the 70% threshold. Additionally, the torsional irregularity coefficient was found to be 1.45, exceeding the limit of 1.40. Since the conditions for applying the single-mode pushover method were not met according to TBEC (2018), a multi-mode pushover analysis was conducted on the building. In this method, the structure is incrementally pushed using a generalized load vector until a specific story reaches its target inter-story drift ratio.

As a result of the multi-mode pushover analyses performed for each earthquake direction, the damage regions in the structural system elements were identified. The damage states for each floor are presented in Tables 5 and 6. Columns and shear wall elements are referred to as vertical elements in these tables.

Table 5. Damage regions in *x* direction.

Element	Floor	LDR	MDR	MDR	CR
Vertical	Basement	11	3	0	0
	Ground	8	15	0	0
	1. Floor	11	12	0	0
	2. Floor	8	15	0	0
	3. Floor	16	7	0	0
	4. Floor	4	6	0	1
Beam	Basement	3	0	0	0
	Ground	36	0	0	0
	1. Floor	18	4	0	0
	2. Floor	19	3	0	0
	3. Floor	39	2	0	0
	4. Floor	6	2	2	0

Table 6. Damage regions in *y* direction.

Element	Floor	LDR	MDR	MDR	CR
Vertical	Basement	10	4	0	0
	Ground	4	19	0	0
	1. Floor	5	18	0	0
	2. Floor	7	16	0	0
	3. Floor	17	6	0	0
	4. Floor	1	10	0	0
Beam	Basement	0	0	0	0
	Ground	32	2	0	0
	1. Floor	8	15	0	0
	2. Floor	9	14	0	0
	3. Floor	32	3	0	0
	4. Floor	7	5	0	0

To visually present the damage states occurring in each direction, the percentage distribution of damage regions for the structural system elements on each floor is shown in Figs. 13–16.

The structural safety of the existing reinforced concrete building is determined based on the damage states of its vertical and horizontal load-bearing elements. As a result of the analyses, the fourth floor i.e., the roof level, where the lowest stiffness is observed and changes in column dimensions occur, has been identified as the most critical story in terms of performance level. For the Design Earthquake Level 2 (DD2), the building is expected to meet the performance target of life safety. This performance level corresponds to a state where the structural elements sustain damage that is not excessively severe and, in most cases, repairable. According to

the analysis results, it has been determined that the building does not meet the targeted performance level and remains at the "collapse prevention" performance level.

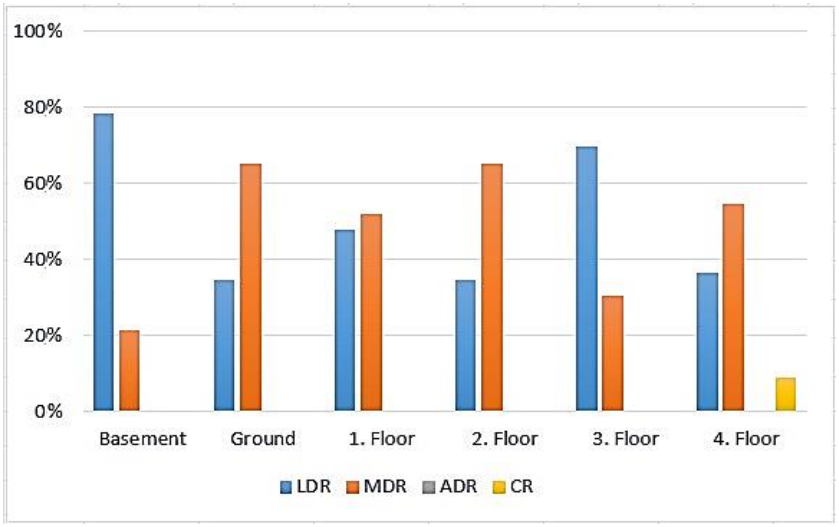

Fig. 13. Damage distributions of vertical elements in *x* direction.

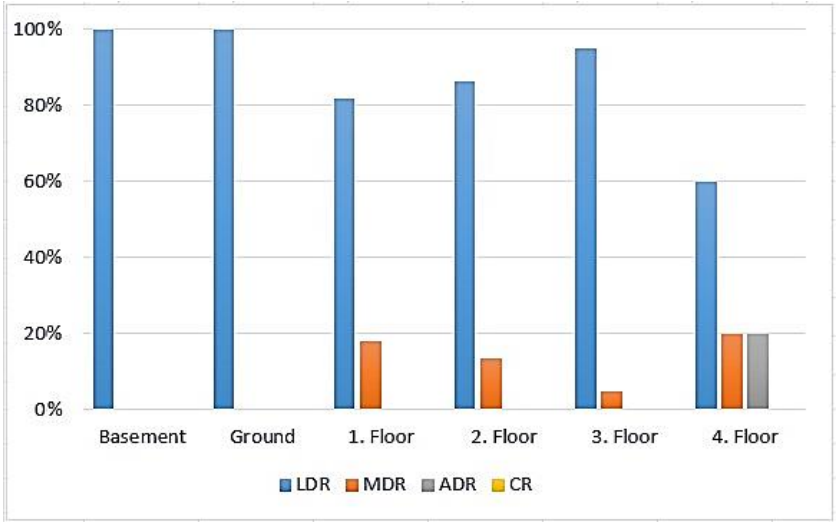

Fig. 14. Damage distributions of beams in *x* direction.

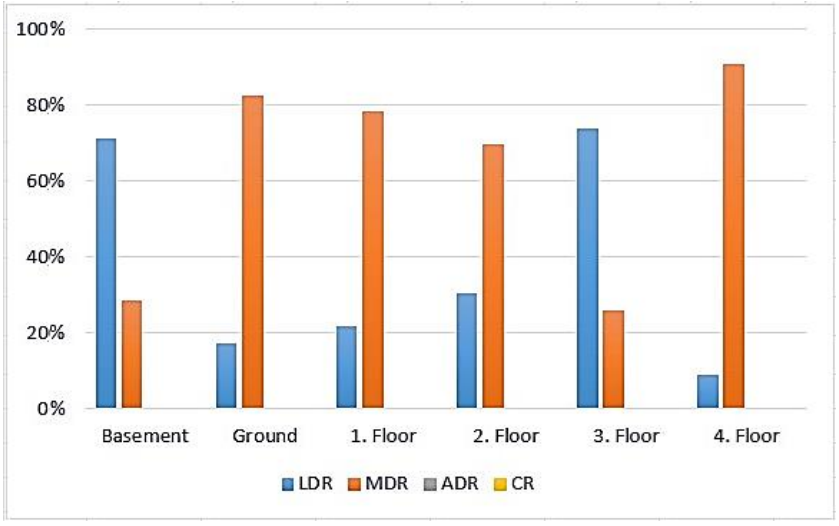

Fig. 15. Damage distributions of vertical elements in y direction.

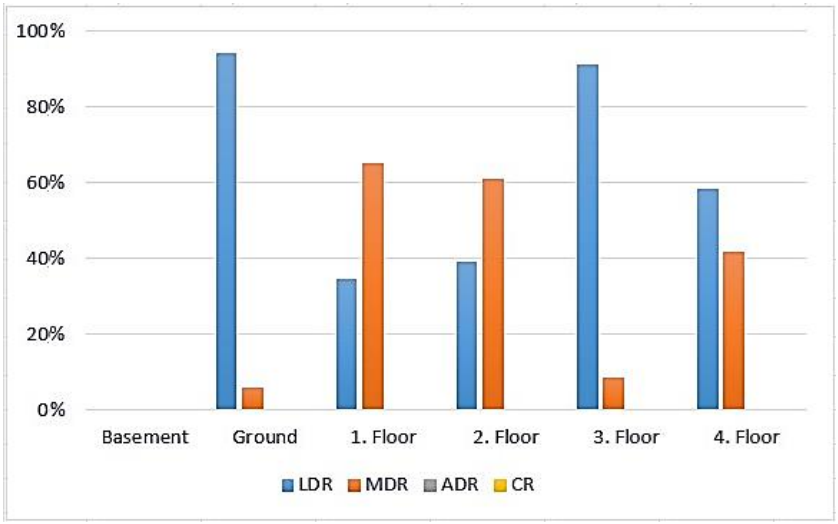

Fig. 16. Damage distributions of beams in *y* direction.

4. Conclusions

In this study, the seismic performance of an existing residential reinforced concrete building with a mixed slab system was investigated. Initially, in-situ inspections of the structural system elements were conducted. Subsequently, the soil classification of the site was determined. The compressive strength of the concrete was calculated based on the results of core sample tests. Through surface stripping and rebar scanning studies performed on the structural elements, the longitudinal and transverse reinforcement layout was identified. As a result, the concrete class of the building was determined to be C10, and the reinforcement steel was classified as S420 ribbed bars.

The building was modeled in the computer environment via STA4CAD V13.1 (2023) software. As a result of the analysis, since the obtained mass participation ratio and torsional irregularity coefficient were outside the limits permitted by the Turkish Building Earthquake Code TBEC (2018), a multi-mode nonlinear analysis was conducted instead of a single-mode analysis. For each earthquake direction, target displacement values were determined for the DD2 earthquake level. The damage states of all vertical and horizontal structural elements on each floor were identified. Based on the obtained damage ratios, the seismic performance of the existing building was evaluated.

Since the examined building is a residential structure, it is expected to meet the life safety performance level under the relevant earthquake scenario. The damage conditions of the reinforced concrete beams, columns, and shear walls in the building were investigated. Despite the presence of a partial basement floor, low concrete compressive strength, variations in column cross-section dimensions between floors, insufficient stirrup confinement, and the improper implementation of 135-degree stirrup hook angles, these factors have nonetheless contributed positively to the building's overall performance. Except for one column located in the collapse region of the critical story, no other vertical load-bearing element was found within the collapse zones. Additionally, two beams were observed to fall within the severe damage region on the critical floor. However, due to the presence of a vertical structural element within the collapse region, the life safety performance level targeted for the DD2 earthquake level could not be achieved.

The seismic performance of existing reinforced concrete buildings can be assessed using linear and nonlinear methods. In this study, a nonlinear pushover analysis was applied to the building to achieve a more realistic evaluation. Since the conditions permitted by TBEC (2018) were not met, the analysis was conducted in a multi-mode framework. It is considered that the findings obtained from this study will guide future research on the design and performance evaluation of buildings with mixed slab systems and contribute to the literature in the field of earthquake engineering.

Acknowledgements

None declared.

Funding

The authors received no financial support for the research, authorship, and/or publication of this manuscript.

Conflict of Interest

The authors declared no potential conflicts of interest with respect to the research, authorship, and/or publication of this manuscript.

Author Contributions

All of the authors made substantial contributions to conception and design, or acquisition of data, or analysis and interpretation of data; were involved in drafting the manuscript or revising it critically for important intellectual content; and gave final approval of the version to be published.

Data Availability

The datasets created and/or analyzed during the current study are not publicly available, but are available from the corresponding author upon reasonable request.

REFERENCES

Bento S, Simões A (2021). Seismic performance assessment of buildings. *Buildings*, 11(10), 440.

Erdem RT (2016). Performance evaluation of reinforced concrete buildings with softer ground floors. *Gradevinar*, 68(1), 39–49.

Erdem RT, Karal K (2022). Performance evaluation and strengthening of reinforced concrete buildings. *Revista de la Construcción,* 21(1), 459–475.

Erdem RT, Uyan B (2025). Evaluation of irregular reinforced concrete buildings according to different soil classes. *Revista de la Construcción*, 24(1), 184–195.

Ergin İ, Seçer M (2025). Structural evaluation of selected reinforced concrete buildings within the scope of urban renewal in Izmir province. *Journal of BAUN Institute of Science and Technology*, 27(1), 110–125.

Eşki H, Sayın B, Güneş B (2020). The effect on structural behavior of different slab types for RC buildings. *Journal of Structural Engineering & Applied Mechanics*, 3(1), 41–48.

Golghate K, Vijay B, Amit S (2013). Pushover analysis of 4 storey's reinforced concrete building. *International Journal of Latest Trends in Engineering and Technology*, 2, 80–84.

Gupta P, Gupta C (2024). Seismic performance evaluation of reinforced concrete flat slab buildings using ETABS. *Asian Journal of Civil Engineering*, 25(7), 4995–5007.

Hulke P, Solanke SS (2023). Comparative study of different types of slab for same structural condition. *Smart and Sustainable Technologies for Disaster Resilient Infrastructure*, online, 012001.

Joyner MD, Sasani M (2020). Building performance for earthquake resilience. *Engineering Structures*, 210, 110371.

Kalib ES (2021). Response of the flat reinforced concrete floor slab with openings under lateral loads. *Advances in Civil Engineering*, 2021, 2503475.

Khajehdehi R, Panahshahi N (2016). Effect of openings on in-plane structural behavior of reinforced concrete floor slabs. *Journal of Building Engineering*, 7, 1–11.

Kuria KK, Kegyes-Brassai OK (2023). Nonlinear static analysis for seismic evaluation of existing RC hospital building. *Applied Sciences*, 13(21), 11626.

Lin JL, Chuang MC (2023). Simplified nonlinear modeling for estimating the seismic response of buildings. *Engineering Structures*, 279, 115590.

Mene P, Nilawar AP (2022). Comparative study of different types of slab structures. In: Mahajan V, Chowdhury A, Padhy NP, Lezama F, editors. *Sustainable Technology and Advanced Computing in Electrical Engineering*. Springer, Singapore, 695–703.

Özbayrak A (2021). Numerical investigation of the effect of beam slab openings in RC structures on seismic behavior. *Ingeniería de Construcción*, 36(3), 512–526.

Ozkul TA, Kurtbeyoglu A, Borekci M, Zengin B, Kocak A (2019). Effect of shear wall on seismic performance of RC frame buildings. *Engineering Failure Analysis*, 100, 60-75.

Ricci P, Manfredi V, Noto F, Terrenzi M, Petrone C, Celano F, Verderame GM (2018). Modeling and seismic response analysis of Italian code-conforming reinforced concrete buildings. *Journal of Earthquake Engineering*, 22(2), 105–139.

Shende SR, Sawai G, Bodane M (2024). Comparative assessment of different types of slabs by using software. *International Journal of Research Publication and Reviews*, 5(5), 12805–12811.

STA4CAD (2023). STA4CAD V13.1 Structural Analysis and Design Software [Computer software]. STA4CAD Engineering Software Inc., İstanbul, Türkiye.

Sullivan TJ, Saborio-Romano D, O'Reilly GJ, Welch DP, Landi L (2021). Simplified pushover analysis of moment resisting frame structures. *Journal of Earthquake Engineering*, 25(4), 621–648.

TBEC-2018 (2018). Türkiye Building Earthquake Code: Specifications for design of buildings under seismic effects. Disaster and Emergency Management Authority, Ankara, Türkiye.

TS-498 (1997). Design loads for buildings. Turkish Standards Institution, Ankara, Türkiye.

Challenge Journal of Structural Mechanics

Research Article

A discrete element method for evaluating the seismic performance of concrete gravity dam-reservoir systems under main shock-aftershock events

Berat Feyza Soysal [a,*]

[a] *Department of Civil Engineering, Çankaya University, 06815 Ankara, Türkiye*

ABSTRACT

Dams are crucial for water supply, flood prevention, and hydroelectric power generation. Often located in seismically active regions, they are vulnerable to main shock-aftershock (MS-AS) sequences, which can compromise structural integrity and hydraulic safety. Critical aspects of dam response to MS–AS events remain unclear, particularly the required rest time between successive events and threshold AS-to-MS intensity measure ratios that could serve as predictors of additional damage. This study addresses these gaps by analyzing concrete gravity dam–reservoir systems of three heights (50 m, 100 m, and 150 m) using the developed discrete element–based approach coupled with displacement/pressure-based mixed finite elements for the reservoir. Empirical rest time equations were derived from 124 as-recorded ground motions, while seismic performance under varying intensity levels was evaluated using 14 as-recorded MS–AS sequences. Damage was quantified using discrete indices of base crack length, maximum base crack width, and maximum total upstream crack width. Results indicate that AS primarily propagate existing cracks at lower intensities, whereas higher intensities generate new cracks along the upstream face, increasing crack widths by 25–30% on average. The 50 m high dam remained within the mild damage category, while taller dams occasionally reached moderate levels, posing potential seepage risks. Threshold AS-to-MS ratios for four different intensity measures were identified. These findings provide mechanistic insight into crack propagation under MS-AS events, providing practical guidance for post-earthquake dam safety assessment, inspection prioritization, and incorporating sequential seismic effects into design and emergency planning.

ARTICLE INFO

Article history:
Received – July 2, 2025
Revision requested – August 19, 2025
Revision received – September 12, 2025
Accepted – September 24, 2025

Keywords:
Concrete gravity dam-reservoir system
Crack width
Discrete element modeling
Main shock-aftershock sequence
Seismic intensity measure

Citation: Soysal BF (2025). A discrete element method for evaluating the seismic performance of concrete gravity dam-reservoir systems under main shock-aftershock events. *Challenge Journal of Structural Mechanics*, 11(4), 229–244.

1. Introduction

Dams are crucial structures constructed for water storage. The stored water in the reservoir is used to supply water, prevent floods, and generate hydroelectric power. The Jawa Dam, located in Jordan and constructed around 3000 BC, is recognized as the earliest known dam (Fahlbusch 2009). As of 2023, the global count of dams exceeds 62000 (ICOLD 2023). Given their frequent construction in active seismic zones (SRC n.d.), dams necessitate seismic performance evaluations (Hacıefendioğlu et al. 2015; Akköse et al. 2016) due to the potential for catastrophic loss of life and severe property damage upon failure.

Earthquakes consist of foreshocks, main shocks, and aftershocks. While foreshocks can indicate an impending earthquake, their typically smaller magnitudes (Mignan 2014) preclude significant structural damage.

* *Corresponding author*. Tel.: +90-312-233-1402 ; E-mail address: fsoysal@cankaya.edu.tr (B. F. Soysal)
ISSN: 2149-8024 / DOI: https://doi.org/10.20528/cjsmec.2025.04.005

However, historical earthquake events have demonstrated that aftershocks can exhibit magnitudes comparable to main shocks (Risk Management Solutions 2008; Wen et al. 2009; USGS 2015). If a structure is already damaged by a main shock, a subsequent strong aftershock can intensify the structural damage, potentially leading to collapse (Alliard and Leger 2008; Hariri-Ardebili and Kianoush 2014; Pang et al. 2019; Sadeghi and Moradloo 2022). Many studies have confirmed this effect. Analyses of single-degree-of-freedom (SDOF) systems revealed increased damage accumulation under seismic sequences (Amadio et al. 2003; Hatzigeorgiou and Beskos 2009; Hatzigeorgiou 2010). Investigations of steel frames (Amadio et al. 2003; Fragiacomo et al. 2004) and concrete frames (Faisal et al. 2013) demonstrated that aftershocks substantially increased damage. Similarly, Guo et al. (2020) proposed a fragility function including aftershocks and showed that strong aftershocks increased bridge collapse probabilities.

Concrete dams are also vulnerable to main shock-aftershock (MS–AS) sequences. Alliard and Leger (2008) analyzed a gravity dam considering reduced drainage efficiency after main shocks and found that aftershocks could induce additional damage and sliding displacements. The seismic performance of the Koyna Gravity Dam under MS–AS sequences has been investigated extensively (Zhang et al. 2013; Wang et al. 2017, 2020; Sadeghi and Moradloo 2022; Ashna et al. 2024). Reported damage measures included local and global damage indices (Zhang et al. 2013; Wang et al. 2017; Ashna et al. 2024), crest displacement (Wang et al. 2017, 2020), damage patterns (Wang et al. 2020), and sliding of the top block (Sadeghi and Moradloo 2022). These studies consistently showed that the dam's neck region was particularly susceptible to aftershocks, with strong aftershocks leading to greater damage accumulation. Similar findings were reported for other gravity dam–foundation systems (Zhang et al. 2019, 2021; Zhai et al. 2022) and for arch (Hariri-Ardebili and Kianoush 2014) and CFRD dams (Pang et al. 2019). More recently, Akpinar et al. (2023) investigated post-seismic effects without explicitly applying aftershocks and found increased damage in concrete gravity dams.

A crucial aspect of successive seismic analyses is determining the appropriate time interval between the main shock and aftershocks, ensuring the structure returns to a resting state before the subsequent seismic event. For SDOF and steel frames, Pirooz et al. (2021) proposed formulations to estimate this interval. However, no comprehensive rest time study exists for dams. Previous research employed intervals ranging from 10 seconds (Pang et al. 2019; Wang et al. 2017, 2020; Zhang et al. 2019, 2021; Zhai et al. 2022; Ashna et al. 2024) to 100 seconds (Zhang et al. 2013).

Although prior studies have confirmed the damaging potential of aftershocks, several key issues remain unresolved. No empirical data are available on the required rest time between consecutive seismic events for dam–reservoir systems. Threshold values of aftershock-to-main shock intensity measure ratios that can serve as predictors of damaging aftershocks have not been established. Moreover, most existing analyses considered only a single dam height and a limited number of MS–AS sequences, while relying mainly on finite element methods that cannot directly compute discrete damage indices such as crack widths.

This study introduces a discrete element–based framework developed by the author to directly model crack initiation and propagation in dam–reservoir systems of varying heights. The novelty lies in (i) developing empirical rest time equations for dam–reservoir systems of different heights, and (ii) identifying threshold aftershock-to-main shock intensity measure ratios that can serve as predictors of damaging aftershocks. These contributions provide practical indicators directly linked to discrete damage indices such as base crack length, maximum base crack width, and maximum total crack width on the upstream face, the latter being particularly relevant for seepage risks.

The manuscript is organized as follows: Section 2 presents the theoretical formulation of the MAEM and the displacement/pressure-based mixed finite element reservoir model. Section 3 provides validation of these models using three different benchmark cases. Section 4 describes the dam–reservoir models and input ground motions. Section 5 presents the proposed rest time equations. Section 6 evaluates the seismic performance of dam systems by means of discrete damage indices for various seismicity levels and examines the influence of ground motion parameters, and Section 7 summarizes the conclusions.

2. Theory and Formulation

2.1. Modified applied element method

The Applied Element Method (AEM) is a discrete element-based approach where a structure is discretized into rigid elements interconnected by normal and shear spring pairs (Meguro and Tagel-Din 2000). This method is modified (MAEM) by incorporating two additional diagonal springs between elements to accurately model Poisson's effect (Fig. 1(a)). The stiffness values for the normal (k_n), shear (k_s), and diagonal, (k_{nd}) springs, which represent the macroscopic material properties of Young's modulus (E) and Poisson's ratio (ν), are calculated based on the Cauchy-Born rule and hyper-elastic theory (Eq. 1). The details of the formulation of MAEM can be found in Soysal et al. (2023).

$$k_n = \frac{Et}{(1+\nu)s} \quad k_n = \frac{Et}{(1+\nu)s} \quad k_{nd} = \frac{Et\nu}{(1-\nu^2)} \tag{1}$$

In Eq. (1), t denotes the thickness of the structure, and s represents the number of normal-shear spring pairs connecting the elements.

The nonlinear behavior of concrete, specifically tensile cracking, is modeled by implementing the Maekawa tension softening material model (Maekawa et al. 2003) (Fig. 1(b) and Eq. (2)). Mesh independence is achieved by incorporating fracture energy into the system (Soysal et al. 2023).

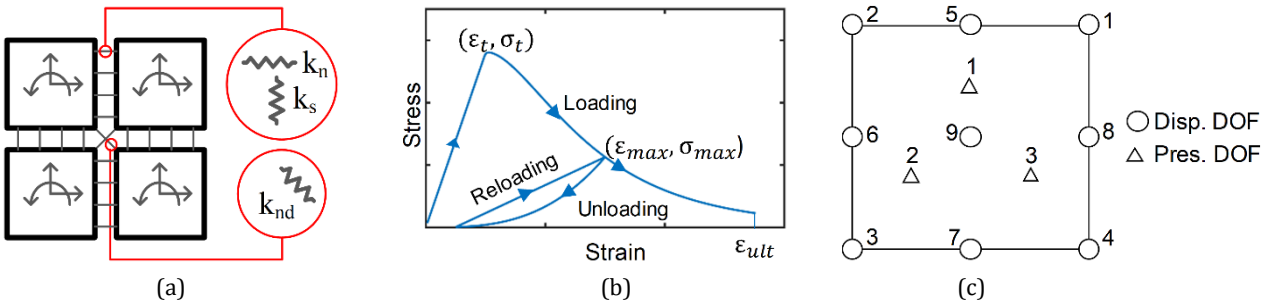

(a) (b) (c)

Fig. 1. Modified Applied Element Method and the reservoir element: (a) Modified applied elements; (b) Tension softening model; (c) Displacement/pressure-based mixed finite element.

Loading: $\varepsilon > \varepsilon_{\max}$

$$\sigma = \begin{cases} \frac{\sigma_t}{\varepsilon_t}\varepsilon & \text{if } \varepsilon \le \varepsilon_t \\ \sigma_t \left(\frac{\varepsilon_t}{\varepsilon}\right)^c & \text{if } \varepsilon_t < \varepsilon < \varepsilon_{\text{ult}} \\ 0 & \text{if } \varepsilon \ge \varepsilon_{\text{ult}} \end{cases}$$

Unloading: $\varepsilon \le \varepsilon_{\max}$ and $\varepsilon \le \varepsilon_0$

$$\sigma = E_{\text{ul}} \cdot \varepsilon \cdot \alpha$$

$$E_{ul} = \frac{\sigma_{\max}}{\varepsilon_{\max}} \text{ and } \alpha = \left(\frac{\sigma_0}{E_{\text{ul}}\varepsilon}\right)\left(\frac{\varepsilon}{\varepsilon_0}\right)^3$$

Reloading: $\varepsilon \le \varepsilon_{\max}$ and $\varepsilon > \varepsilon_0$

$$\sigma = \sigma_{\max} - (\sigma_{\max} - \sigma_0)\left(\frac{\varepsilon_{\max} - \varepsilon}{\varepsilon_{\max} - \varepsilon_0}\right) \quad (2)$$

Here, ε represents the tensile strain of concrete, σ is the corresponding tensile stress, σ_t is the uniaxial concrete tensile strength, and ε_t is the corresponding tensile cracking strain. c is the softening parameter that defines the post-peak behavior. $\varepsilon_{\max}$ and $\sigma_{\max}$ denote the maximum tensile strain experienced and its corresponding tensile stress, respectively. The current strain and stress are denoted as ε_0 and σ_0, respectively. The unloading stiffness is computed as $E_{\text{ul}}\alpha$, where α is the stiffness parameter.

For all springs, compressive behavior is assumed to be linear. Conversely, the shear springs exhibit brittle behavior. Once the normal spring pair enters the nonlinear loading regime (i.e., $\varepsilon \ge \varepsilon_t$), the corresponding shear spring pair loses its capacity to carry force or contribute to the system's stiffness.

2.2. Displacement/pressure-based mixed finite element

In this study, the dam-reservoir interaction is accounted for by coupling the modified applied elements with the displacement/pressure-based mixed finite elements proposed by Wang and Bathe (1997). The implemented finite element possesses nine displacement and three pressure degrees of freedom (Fig. 1(c)). The matrix formulation of the finite element is presented in Eq. (3).

$$\begin{bmatrix} \mathbf{M} & \mathbf{0} \\ \mathbf{0} & \mathbf{0} \end{bmatrix} \begin{bmatrix} \ddot{\widehat{\boldsymbol{U}}} \\ \ddot{\widehat{\boldsymbol{P}}} \end{bmatrix} + \begin{bmatrix} \mathbf{K}_{uu} & \mathbf{K}_{up} \\ \mathbf{K}_{pu} & \mathbf{K}_{pp} \end{bmatrix} \begin{bmatrix} \widehat{\boldsymbol{U}} \\ \widehat{\boldsymbol{P}} \end{bmatrix} = \begin{bmatrix} \boldsymbol{R} \\ \mathbf{0} \end{bmatrix} \quad (3)$$

In this equation, $\mathbf{M}$ denotes the mass term of the element, $\widehat{\boldsymbol{U}}$ and $\widehat{\boldsymbol{P}}$ are the displacement and pressure solution vectors, respectively, and $\mathbf{K}_{uu}$, $\mathbf{K}_{up}$, $\mathbf{K}_{pu}$, and $\mathbf{K}_{pp}$ represent the corresponding stiffness sub-matrices. The pressure unknowns can be statically condensed for a finite bulk modulus, simplifying the solution to Eq. (4).

$$\mathbf{M}\ddot{\widehat{\boldsymbol{U}}} + \left(-\mathbf{K}_{up}\,\mathbf{K}_{pp}^{-1}\,\mathbf{K}_{pu}\right)\widehat{\boldsymbol{U}} = \boldsymbol{R} \quad (4)$$

For almost incompressible materials, the displacement/pressure-based mixed formulation satisfies the inf-sup conditions, thereby eliminating spurious zero-energy modes (Wang and Bathe 1997).

The Sommerfeld radiation boundary condition (Sommerfeld 1949) is applied at the far end of the reservoir to account for radiating waves.

3. Validation Studies

Several validation studies, including pure tension, splitting tension, push-over loading of a scaled concrete dam, tensile testing of double-edged notched specimens, and the cracking response of the Koyna Dam-reservoir system, have been conducted to verify the MAEM and its coupling with fluid finite elements (Soysal Albostan 2021; Soysal et al. 2023). Further validation (Soysal and Arici 2024) was carried out by simulating the variability in concrete properties utilizing the random field theory (Wei et al. 2024). The direct tension test (Gopalaratnam and Shah 1985) and the push-over loading of a scaled concrete dam (Carpinteri et al. 1992) were modeled with five random samples, and the corresponding load-displacement and cracking behaviors were obtained. For brevity, this manuscript presents the cracking response of the Koyna Dam-reservoir system under nonlinear dynamic analysis, along with the aforementioned random field results. Detailed information on these validations can be found in the works of Soysal Albostan (2021), Soysal et al. (2023), and Soysal and Arici (2024).

The simulated damage in the Koyna Dam-reservoir system is compared with the observed damage in Fig. 2(a). The model successfully reproduced the localized cracking at the heel and neck of the dam. Additional cracks appeared on the downstream face, likely due to mesh discretization and localized stress concentrations. Overall, the simulated cracking pattern is compatible with the actual damage observed in the Koyna Dam.

The random field results for the direct tension test exhibited a similar distribution of load-displacement values around the experimental result. The crack patterns obtained were also consistent with the experimental findings (Fig. 2(b)). The robustness of the methodology was further demonstrated in the push-over test, where the load-CMOD response closely matched the experimental data. The resulting fracture patterns followed essentially the same crack path and agreed well with the experimental result (Fig. 2(c)).

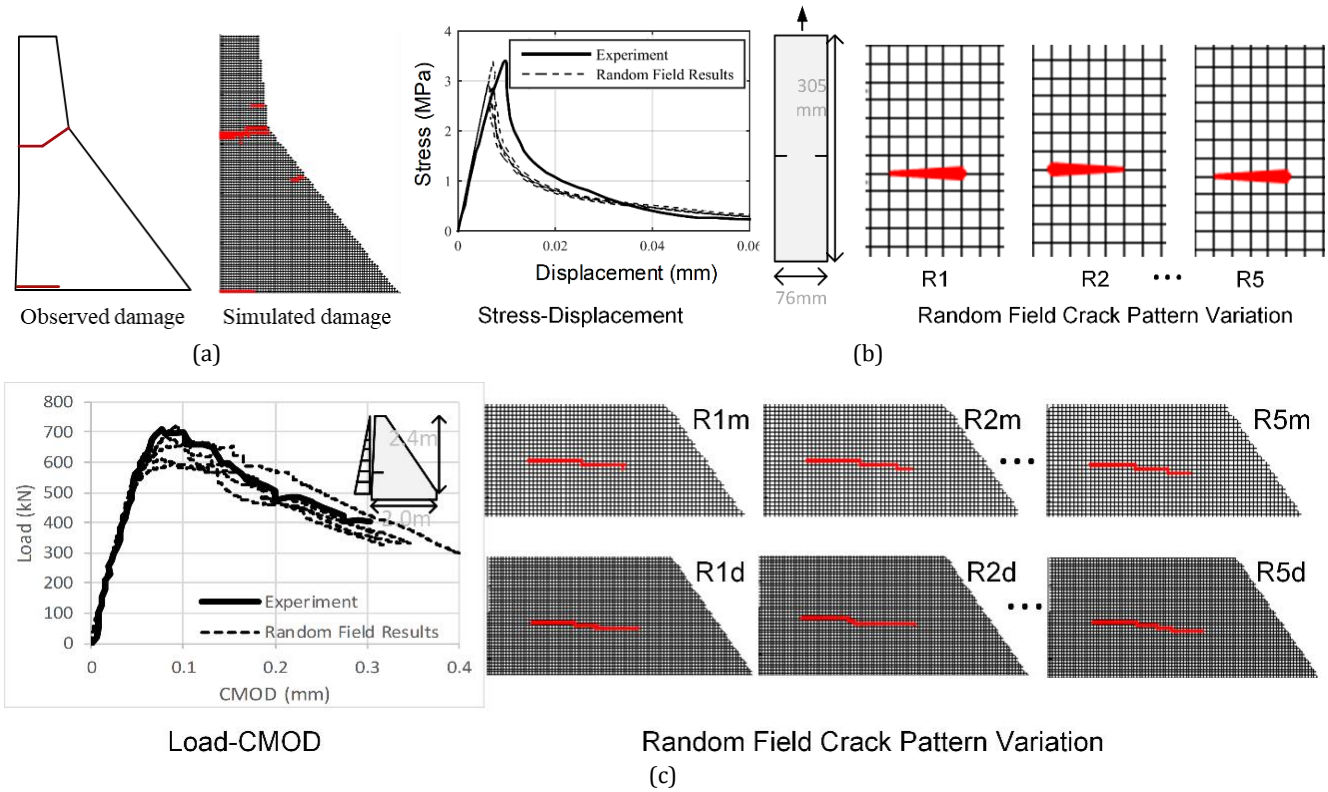

Fig. 2. Verification results: (a) Damage of Koyna Dam-reservoir system; (b) Random field results for direct tension test (Gopalaratnam and Shah 1985); (c) Random field results for push-over test (Carpinteri et al. 1992).

4. Dam Systems and Ground Motions

4.1. Coupled MAEM – Finite element models

The seismic performance of concrete gravity dam-reservoir systems under main shock-aftershock events was evaluated by considering three distinct concrete gravity dam sections: 50 m (Model I), 100 m (Model II), and 150 m in height (Model III) (Fig. 3). The cross-sectional properties of the dams were selected based on the "standard" dam cross-section (Chopra 1978; Lokke and Chopra 2013), featuring a vertical upstream face and a 0.8/1 downstream slope. The reservoir height was assumed to be 2 m lower than the dam height, and its length was three times the dam height. The dam body was discretized into 1m x 1m modified applied elements, while the reservoir mesh consisted of 2m x 8m finite elements. The Young's modulus, Poisson's ratio, tensile strength, and fracture energy of the concrete dams were assumed to be 28 GPa, 0.2, 2.4 MPa, and 200 N/m, respectively. The acoustic wave speed, Poisson's ratio, and water density for the reservoir were 1438.66 m/s, 0.4999, and 1000 kg/m^3, respectively. These material properties are within the typical range for concrete gravity dam-reservoir systems reported in the literature (Leger and Leclerc 1996; Hariri-Ardebili and Saouma 2016; Chen et al. 2019; Ghallab 2020), ensuring realistic material representation for a generic dam model where specific site data are unavailable. The first three frequencies of the systems are presented in Table 1. A 5% Rayleigh damping ratio, applied at the first and third modes of the systems, was utilized in the nonlinear transient analyses.

4.2. Selected earthquake ground motions

The required time interval between main shocks and aftershocks was estimated using 124 acceleration records from 21 different events, sourced from the PEER NGA-West2 (http://ngawest2.berkeley.edu) ground motion database and COSMOS strong motion virtual data center (https://www.strongmotioncenter.org/) (Table A1). These records had fault distances (R) of 0-85 km, magnitudes (M) of 5.3-7.6, and shear wave velocity ($V_{s,30}$) above 203 m/s, with the minimum value corresponding to stiff soil according to NEHRP soil classification. The dataset was compiled from prior studies on seismic analyses of concrete gravity dams (Lokke and Chopra 2013; Zhang et al. 2013; Huang 2014; Toikka et al. 2019; Wang et al. 2017), and assessments of various structures under main shock-aftershock events (Li et al. 2014; Khanal 2019; Mangalathu et al. 2019).

Seismic performance of concrete gravity dams was evaluated using 14 selected main shock-aftershock events (Table A2), with main shock fault distances (R) of 0–19.5 km and magnitudes (M) of 6.0–7.6, and corresponding aftershock distances (R) of 3.4–25 km and magnitudes (M) of 5.3–6.2. Shear wave velocities ($V_{s,30}$) were greater than 382 m/s, with the minimum value corresponding to very dense soil/soft rock per NEHRP soil classification.

Table 1. The first three frequencies of dam-reservoir systems.

	Model I	Model II	Model III
f_1 (Hz)	6.1	3.1	2.1
f_2 (Hz)	13.8	7.5	5.3
f_3 (Hz)	19.6	11.1	7.6

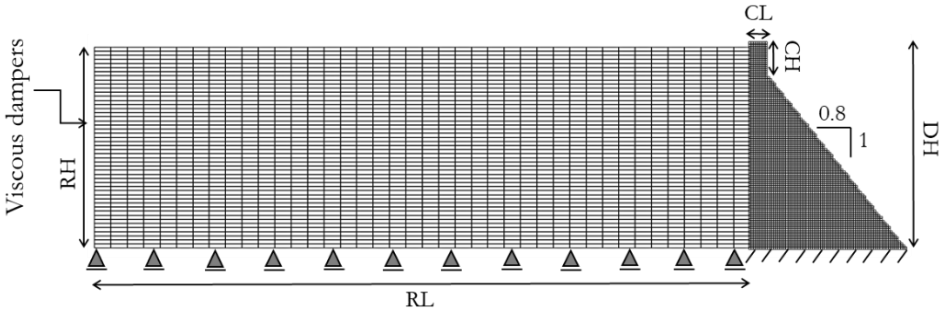

	Model I	Model II	Model III
DH (m)	50	100	150
CL (m)	4	8	12
CH (m)	8	15	20
RL (m)	160	320	456
RH (m)	48	98	148

Fig. 3. Coupled dam-reservoir systems.

5. The Estimation of the Required Time Interval Between Main Shocks and Aftershocks for Concrete Gravity Dams

Many aftershocks occur after a main shock, causing further damage to structures, especially if the damage is not repaired. These aftershocks typically occur after a time interval, allowing the structure to come to rest before the subsequent seismic event. Consequently, in numerical modeling, it is crucial to apply aftershocks once the structure has returned to a stable, resting state. This requires defining an appropriate time interval between successive seismic events. For dams, this time interval has been assumed as fixed values, ranging from 10 seconds (Pang et al. 2019; Wang et al. 2017, 2020; Zhang et al. 2019, 2021; Zhai et al. 2022; Ashna et al. 2024) to 100 seconds (Zhang et al. 2013).

This section proposes empirical rest time equations between main shocks and aftershocks specifically for concrete gravity dam-reservoir systems to reduce computational analysis time in numerical simulations, while ensuring the structure is at rest before the subsequent event. To this end, the three dam-reservoir systems shown in Fig. 3 were subjected to the 124 as-recorded ground motions (Table A1). After each motion, a zero-acceleration period was introduced to determine the time required for the dams to return to a resting state. Following Pirooz et al. (2021), the dams are considered at rest when the free vibration velocity of their crest is ≤0.1% of the maximum free vibration velocity.

Fig. 4 presents the horizontal PGA component versus the normalized rest time (NRT), defined as the estimated rest time divided by the corresponding horizontal PGA component of the ground motion, for the three dam-reservoir systems. A clear nonlinear correlation between NRT and PGA is evident for all models, with Model I (50 m height) showing the lowest NRT, and Model III (150 m height) showing the highest. The natural frequency decreases as the dam height increases, leading to longer rest times. For Models I and III, the rest times ranged from 2.2-3.5 s and 4.6-6.7 s, respectively.

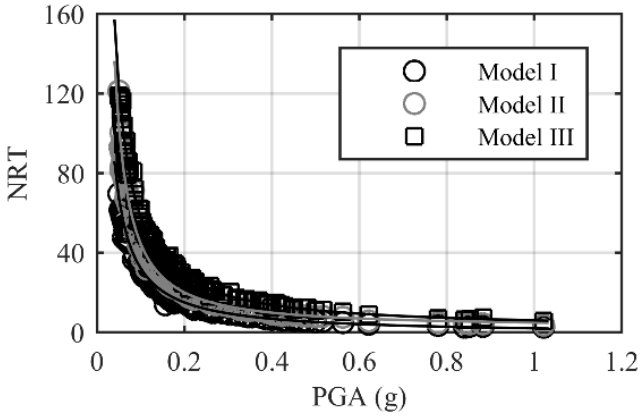

Fig. 4. Normalized rest time (NRT) for concrete gravity dam-reservoir systems.

For the scatter data presented in Fig. 4, a nonlinear curve of the form $y = ax^b + c$ was fitted using the nonlinear least squares method (indicated by solid lines in Fig. 4). The proposed equations for the required time interval between main shock and aftershocks, denoted as NRT_{fitted}, are given in Eqs. (5–7), for Models I-III, respectively.

$$NRT_{\text{fitted,Model I}} = 2.9358PGA^{-1.0502} - 0.9129 \quad (5)$$

$$NRT_{\text{fitted,Model II}} = 2.2684PGA^{-1.2651} + 2.6195 \quad (6)$$

$$NRT_{\text{fitted,Model III}} = 4.3935PGA^{-1.1066} + 1.6151 \quad (7)$$

It should be noted that these equations are based on empirical regression of 124 as-recorded ground motions, specifically derived for concrete gravity dam-reservoir systems with PGAs ranging from 0.05g to 1.02g and dam heights of 50–150 m, with 5% Rayleigh damping. They may not be generalized to other dam types, geometries, or damping ratios without further validation.

6. Seismic Performance Evaluation of Concrete Gravity Dam-Reservoir Systems under Main Shock-Aftershock Events

This section investigates the seismic performances of three concrete gravity dam-reservoir systems with varying heights (Model I – 50 m, Model II – 100 m, Model III – 150 m) under 14 as-recorded main shock-aftershock (MS-AS) earthquake sequences (Table A2). It also evaluates the influence of MS-AS ground motion properties on structural damage to identify the characteristics of damaging AS on concrete gravity dams. The time interval between each sequence was determined using Eqs. (5–7) for the three models. The discrete modeling of the dam body enabled damage assessment through three discrete damage measures: base crack length, maximum base crack width, and maximum total crack width on the upstream (U/S) face.

Four analysis sets were performed. In the first, the Peak Ground Acceleration (PGA) of MS was scaled to 0.5g to ensure nonlinear behavior (Wang et al. 2020), and the same scaling factor was subsequently applied to the corresponding AS. Scaling factors ranged from 0.6 to 4.1 and were uniformly applied to both horizontal and vertical components. In the subsequent sets, the MS PGA was fixed at 0.5g, while the AS PGA was varied at 0.3g, 0.4g, and 0.5g to reflect the observed variability of aftershock intensities in real events (Wang et al. 2017; Guo et al. 2020).

6.1. Damage to concrete gravity dam-reservoir systems for the same scaling factor

Damage indices were computed directly as ratios of MS-AS to MS-only results for each earthquake record (EQ#1 to EQ#14), with a value above 1.0 indicating additional damage due to aftershocks (Table 2).

In most cases, AS did not significantly increase base crack length or width, except Model I, which showed an 11% increase in base crack length for EQ#13 and a 22% increase in base crack width. For Model I, damage was most pronounced at the base, while upstream cracking remained limited. Increases in maximum total crack width on the U/S face ranged from 4% (Model I–EQ#12: from 14.3 mm to 14.9 mm) to 31% (Model II–EQ#14: from 39 mm to 51.2 mm), as illustrated in Table 2 and Fig. 5.

Table 2. Damage measure ratios of MS-AS to MS-only for the same scaling factor of MS-AS.

Model I														
	EQ#1	EQ#2	EQ#3	EQ#4	EQ#5	EQ#6	EQ#7	EQ#8	EQ#9	EQ#10	EQ#11	EQ#12	EQ#13	EQ#14
Base Cr. Length	1.00	1.00	1.00	1.00	1.00	1.00	1.00	1.00	1.00	1.00	1.00	1.00	1.11	1.00
Base Cr. Width	1.00	1.00	1.00	1.00	1.00	1.00	1.00	1.00	1.00	1.00	1.00	1.00	1.22	1.00
U/S Crack Width	1.00	1.00	1.00	1.00	1.00	1.00	1.00	1.00	1.00	1.00	1.01	1.04	1.12	1.06
Model II														
	EQ#1	EQ#2	EQ#3	EQ#4	EQ#5	EQ#6	EQ#7	EQ#8	EQ#9	EQ#10	EQ#11	EQ#12	EQ#13	EQ#14
Base Cr. Length	1.00	1.00	1.00	1.00	1.00	1.00	1.00	1.00	1.00	1.00	1.00	1.00	1.00	1.00
Base Cr. Width	1.00	1.00	1.00	1.00	1.00	1.00	1.00	1.00	1.00	1.00	1.00	1.00	1.00	1.00
U/S Crack Width	1.00	1.00	1.00	1.00	1.00	1.00	1.00	1.00	1.00	1.00	1.01	1.04	1.10	1.31
Model III														
	EQ#1	EQ#2	EQ#3	EQ#4	EQ#5	EQ#6	EQ#7	EQ#8	EQ#9	EQ#10	EQ#11	EQ#12	EQ#13	EQ#14
Base Cr. Length	1.00	1.00	1.00	1.00	1.00	1.00	1.00	1.00	1.00	1.00	1.00	1.03	1.00	1.00
Base Cr. Width	1.00	1.00	1.00	1.00	1.00	1.00	1.00	1.00	1.00	1.00	1.00	1.00	1.00	1.00
U/S Crack Width	1.00	1.00	1.00	1.00	1.00	1.00	1.00	1.00	1.00	1.00	1.10	1.07	1.01	1.00

A closer inspection of crack evolution reveals the mechanical basis of the damage patterns. Aftershocks primarily propagated existing cracks, facilitated by stress concentrations formed at the crack tips during the main shock. The arrival of aftershock seismic waves intensified these stresses at vulnerable zones, further widening and extending the cracks. This effect was most pronounced in Model I, where base cracks exhibited the greatest widening in zones of maximum tensile stress.

While propagation was the dominant mechanism, some new cracks also formed. In Models II and III, several new cracks at the neck and along the upstream face, below the neck region, developed. This indicates that taller dams, influenced by higher vibration modes and reservoir hydrodynamic pressures, can experience crack initiation at multiple elevations, resulting in a more complex damage pattern (Wang et al. 2018).

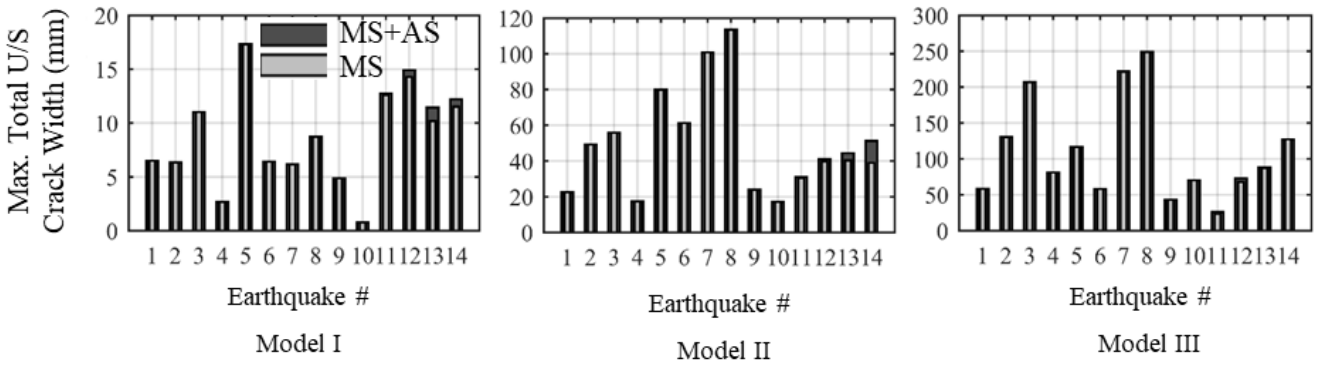

Fig. 5. Maximum total U/S crack width results of dam-reservoir systems under MS-only and MS-AS sequence.

6.2. Damage to concrete gravity dam-reservoir systems under different seismicity levels

Extending the previous analyses, the seismic performance of the three dam-reservoir systems was further evaluated by keeping the main shock (MS) PGA constant at 0.5g while varying the aftershock (AS) PGA to 0.3g, 0.4g, and 0.5g. This approach enabled assessment of crack initiation and propagation while also addressing seepage-related implications for hydraulic safety and dam operation across different AS scenarios. In addition to evaluating overall damage measure ratios, the maximum opening of base cracks and individual U/S cracks was examined for each earthquake record to more precisely assess structural severity and hydraulic implications. The severity of simulated cracks was quantified using the RILEM TC 104 (1991) classification for non-reinforced concrete, in which crack widths are categorized as very mild (<1 mm), mild (1–10 mm), moderate (10–20 mm), and severe (20–25 mm).

The ratios of MS-AS to MS-only damage measure indices are presented in Tables 3-5 for Models I-III, respectively. At 0.3g–0.4g AS intensities, aftershocks generally widened existing U/S cracks or initiated new ones, with limited extension of base cracks. For instance, in Model I, the maximum total crack width on the U/S face increased by 29% at 0.4g (EQ#2: from 6.3 mm to 8.1 mm, Table 3). In Model II, it increased by 20% for EQ#2 (from 45.8 mm to 55.1 mm) and by 30% for EQ#14 (from 39.0 mm to 50.7 mm) (Table 4). In Model III, the maximum total crack width on the U/S face increased by 67% at 0.4g (EQ#11: from 23.6 mm to 39.5 mm, Table 5). A notable case was observed in Model I (EQ#10 at 0.4g) for the base cracks: here, the maximum base crack width increased by 96%, and the crack length extended by 50%. This occurred because the MS produced only a single crack at the base, while the AS both extended it and initiated new cracks at the neck, resulting in a substantial increase in all damage measures.

At 0.5g, new upstream cracks became more frequent, particularly in taller dams. For Model I (EQ#2), the maximum total crack width on the U/S face doubled (from 6.3 mm to 12.7 mm), entirely from the propagation of existing cracks. In Model II, the width increased by 78% (from 45.8 mm to 81.5 mm) due to both new crack formation and propagation of existing cracks. EQ#11 in Model III showed a 2.4-fold increase (from 23.6 mm to 56.8 mm), mainly from new cracks below the neck. The evolution of U/S crack widths with increasing AS intensity is illustrated in Fig. 6. On average, excluding outliers, the maximum total crack width on the U/S face increased by approximately 25–30% at 0.5g AS PGA across all models.

Overall, at 0.3–0.4g AS intensities, aftershocks primarily propagated existing U/S cracks, with occasional base crack extension. At 0.5g, they initiated new cracks at different elevations, creating a more complex damage pattern, especially in taller dams, consistent with the findings of the previous section. Model I highlights neck cracks as critical vulnerabilities. Models II and III show that taller dams are more susceptible to complex AS-induced responses driven by higher modes and reservoir hydrodynamic pressures, which create new tensile stress fields beyond the initial crack zones (Wang et al. 2018).

Applying the RILEM TC 104 (1991) classification, due to the maximum opening of a single crack, Model I consistently remained in the mild category, suggesting a robust safety margin. Models II and III exhibited similar responses: mild damage was dominant for many events, while several records produced moderate cracks both at the base and U/S regions, indicating higher sensitivity to seismic effects. These findings emphasize practical implications for dam operations and safety. Smaller dams maintain stable performance with minimal risk to dam functionality. In contrast, taller dams (Models II and III) are more vulnerable to U/S cracking and seepage, often accompanied by more distributed damage patterns. Because cracks in the upstream face are in direct contact with reservoir water, they may compromise hydraulic safety by facilitating seepage, which can accelerate internal erosion or induce localized instability (Pekau and Zhu 2008). Even moderate U/S crack widths may therefore have significant implications for dam safety and operational management, necessitating careful monitoring, possible mitigation measures, and explicit consideration of aftershocks in design checks and emergency operation planning.

6.3. The effect of ground motion properties on the damage to concrete gravity dam-reservoir systems

Following the findings in the preceding section, it is evident that aftershocks can significantly increase damage to dam-reservoir systems, ranging from minor per-

centages to over 200%. To better understand this phenomenon, a comprehensive study explored how specific ground motion characteristics contribute to additional damage. Although over 25 intensity measures (IMs) were examined, this section presents only the results for Arias Intensity, sustained maximum acceleration, effective design acceleration (EDA), and damage index to maintain conciseness.

Table 3. Damage measure ratios of MS-AS to MS-only under different seismicity levels for Model I.

MS PGA: 0.5g – AS PGA: 0.3g														
	EQ#1	EQ#2	EQ#3	EQ#4	EQ#5	EQ#6	EQ#7	EQ#8	EQ#9	EQ#10	EQ#11	EQ#12	EQ#13	EQ#14
Base Cr. Length	1.00	1.00	1.00	1.00	1.00	1.00	1.00	1.00	1.00	1.07	1.00	1.00	1.00	1.00
Base Cr. Width	1.00	1.00	1.00	1.00	1.00	1.00	1.00	1.00	1.00	1.18	1.00	1.00	1.00	1.00
U/S Crack Width	1.00	1.00	1.00	1.00	1.00	1.00	1.00	1.00	1.00	5.80	1.01	1.00	1.00	1.00
MS PGA: 0.5g – AS PGA: 0.4g														
	EQ#1	EQ#2	EQ#3	EQ#4	EQ#5	EQ#6	EQ#7	EQ#8	EQ#9	EQ#10	EQ#11	EQ#12	EQ#13	EQ#14
Base Cr. Length	1.00	1.25	1.00	1.00	1.00	1.00	1.13	1.00	1.00	1.50	1.00	1.00	1.00	1.00
Base Cr. Width	1.00	1.07	1.00	1.00	1.00	1.00	1.00	1.00	1.00	1.96	1.00	1.00	1.00	1.00
U/S Crack Width	1.00	1.29	1.00	1.00	1.00	1.00	1.07	1.00	1.09	8.99	1.06	1.03	1.00	1.05
MS PGA: 0.5g – AS PGA: 0.5g														
	EQ#1	EQ#2	EQ#3	EQ#4	EQ#5	EQ#6	EQ#7	EQ#8	EQ#9	EQ#10	EQ#11	EQ#12	EQ#13	EQ#14
Base Cr. Length	1.00	1.73	1.06	1.00	1.03	1.04	1.13	1.02	1.02	2.00	1.00	1.00	1.03	1.07
Base Cr. Width	1.00	2.81	1.03	1.16	1.00	1.00	1.00	1.06	1.00	3.00	1.00	1.00	1.00	1.00
U/S Crack Width	1.00	2.01	1.13	1.23	1.04	1.03	1.95	1.02	1.32	14.48	1.17	1.07	1.00	1.10

Table 4. Damage measure ratios of MS-AS to MS-only under different seismicity levels for Model II.

MS PGA: 0.5g – AS PGA: 0.3g														
	EQ#1	EQ#2	EQ#3	EQ#4	EQ#5	EQ#6	EQ#7	EQ#8	EQ#9	EQ#10	EQ#11	EQ#12	EQ#13	EQ#14
Base Cr. Length	1.00	1.00	1.00	1.00	1.00	1.00	1.00	1.00	1.00	1.00	1.00	1.00	1.00	1.00
Base Cr. Width	1.00	1.00	1.00	1.00	1.00	1.00	1.00	1.00	1.00	1.00	1.00	1.00	1.00	1.00
U/S Crack Width	1.00	1.04	1.00	1.00	1.00	1.00	1.00	1.00	1.00	1.00	1.02	1.00	1.00	1.00
MS PGA: 0.5g – AS PGA: 0.4g														
	EQ#1	EQ#2	EQ#3	EQ#4	EQ#5	EQ#6	EQ#7	EQ#8	EQ#9	EQ#10	EQ#11	EQ#12	EQ#13	EQ#14
Base Cr. Length	1.00	1.02	1.00	1.03	1.00	1.00	1.00	1.00	1.00	1.10	1.05	1.00	1.00	1.00
Base Cr. Width	1.00	1.13	1.00	1.00	1.00	1.00	1.00	1.00	1.00	1.25	1.00	1.00	1.00	1.00
U/S Crack Width	1.00	1.20	1.05	1.10	1.01	1.03	1.00	1.02	1.21	1.26	1.06	1.01	1.00	1.30
MS PGA: 0.5g – AS PGA: 0.5g														
	EQ#1	EQ#2	EQ#3	EQ#4	EQ#5	EQ#6	EQ#7	EQ#8	EQ#9	EQ#10	EQ#11	EQ#12	EQ#13	EQ#14
Base Cr. Length	1.00	1.19	1.00	1.10	1.00	1.02	1.00	1.00	1.00	1.19	1.19	1.00	1.00	1.00
Base Cr. Width	1.00	1.10	1.00	1.00	1.00	1.00	1.00	1.00	1.00	1.49	1.18	1.00	1.00	1.00
U/S Crack Width	1.02	1.78	1.16	1.72	1.03	1.10	1.02	1.04	1.54	2.15	1.17	1.10	1.00	1.45

Table 5. Damage measure ratios of MS-AS to MS-only under different seismicity levels for Model III.

	EQ#1	EQ#2	EQ#3	EQ#4	EQ#5	EQ#6	EQ#7	EQ#8	EQ#9	EQ#10	EQ#11	EQ#12	EQ#13	EQ#14
MS PGA: 0.5g – AS PGA: 0.3g														
Base Cr. Length	1.00	1.01	1.00	1.01	1.00	1.00	1.00	1.00	1.00	1.00	1.00	1.00	1.00	1.00
Base Cr. Width	1.00	1.00	1.00	1.00	1.00	1.00	1.00	1.00	1.00	1.00	1.00	1.00	1.00	1.00
U/S Crack Width	1.00	1.02	1.00	1.05	1.00	1.00	1.03	1.00	1.02	1.00	1.10	1.02	1.00	1.00
MS PGA: 0.5g – AS PGA: 0.4g														
	EQ#1	EQ#2	EQ#3	EQ#4	EQ#5	EQ#6	EQ#7	EQ#8	EQ#9	EQ#10	EQ#11	EQ#12	EQ#13	EQ#14
Base Cr. Length	1.00	1.12	1.00	1.10	1.00	1.00	1.00	1.00	1.02	1.02	1.00	1.01	1.00	1.00
Base Cr. Width	1.00	1.18	1.00	1.06	1.00	1.00	1.00	1.00	1.00	1.00	1.00	1.00	1.00	1.00
U/S Crack Width	1.00	1.25	1.00	1.28	1.00	1.00	1.09	1.00	1.38	1.18	1.67	1.06	1.00	1.00
MS PGA: 0.5g – AS PGA: 0.5g														
	EQ#1	EQ#2	EQ#3	EQ#4	EQ#5	EQ#6	EQ#7	EQ#8	EQ#9	EQ#10	EQ#11	EQ#12	EQ#13	EQ#14
Base Cr. Length	1.00	1.22	1.00	1.23	1.00	1.04	1.00	1.00	1.09	1.08	1.04	1.07	1.00	1.00
Base Cr. Width	1.00	1.35	1.00	1.31	1.00	1.00	1.00	1.00	1.03	1.00	1.01	1.09	1.00	1.00
U/S Crack Width	1.00	1.61	1.02	1.71	1.01	1.01	1.26	1.01	1.76	1.56	2.41	1.18	1.01	1.00

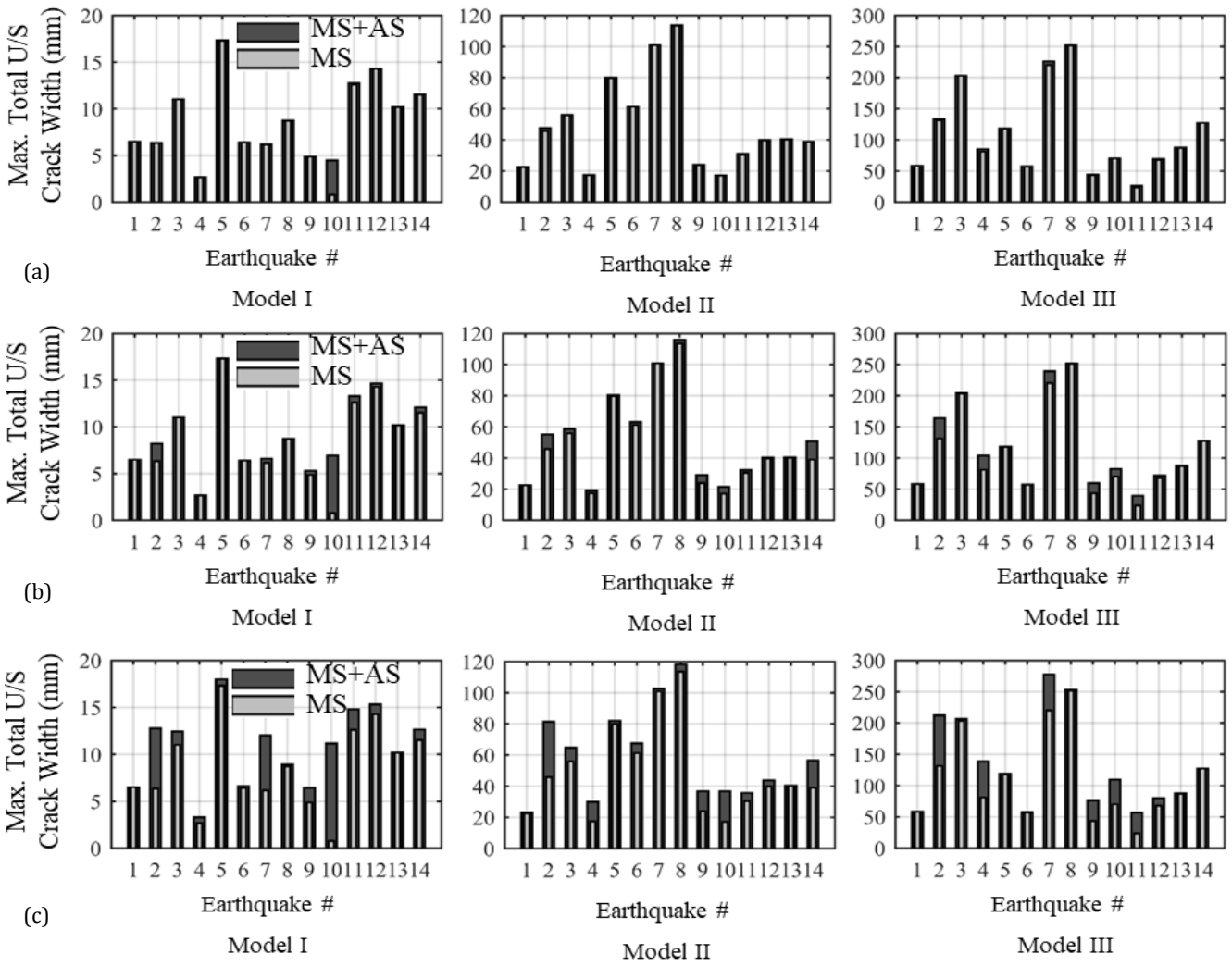

Fig. 6. Maximum total U/S crack width results of dam-reservoir systems under MS-only and under different seismicity levels of MS-AS sequence: (a) MS PGA: 0.5g – AS PGA: 0.3g; (b) MS PGA: 0.5g – AS PGA: 0.4g; (c) MS PGA: 0.5g – AS PGA: 0.5g.

Fig. 7 illustrates the influence of selected ground motion IMs on the increase of the maximum total crack width on the U/S face for the 0.5g AS case. In this figure, the horizontal axis represents the ratio of AS-to-MS intensity measures, while the vertical axis shows the ratio of maximum total crack width on the U/S face for MS–AS sequences to that for MS-only events. A ratio above 1.0 on the y-axis indicates that the aftershock caused additional damage in terms of U/S crack width. Outlier data from EQ#10 in Model I are excluded from the plots to reveal the overall trends better.

For Arias Intensity (Fig. 7(a)), in Model I, AS increased U/S crack widths when the AS-to-MS intensity measure ratio exceeded 0.34. This threshold was lower for Models II and III, at 0.28. In total, 39 out of 42 sequences across all models showed further damage when the Arias Intensity ratio exceeded 0.27.

Sustained maximum acceleration (Fig. 7(b)) showed a similar pattern. For Model I, U/S cracks widened further when the AS-to-MS intensity measure ratio exceeded 0.46; for Models II and III, this threshold was lower at 0.38. Again, 39 of the 42 MS-AS sequences across the three models resulted in additional U/S damage when the sustained maximum acceleration ratio exceeded 0.37.

In the case of effective design acceleration (EDA) (Fig. 7(c)), the threshold for increased U/S crack widths in Model I was an AS-to-MS intensity measure ratio of 0.95. For Models II and III, the thresholds were 0.86. When the EDA ratio exceeded 0.85, further U/S cracking was observed in 39 of the 42 earthquake sequences.

Lastly, for the damage index (Fig. 7(d)), the threshold AS-to-MS intensity measure ratio across all dam models was 0.28. As with the other IMs, 39 of the 42 sequences led to increased U/S crack widths when the damage index ratio exceeded 0.26.

The uncertainty of the reported threshold values was quantified by applying a non-parametric bootstrapping method (Mooney and Duval 1993). Using 10000 resamples with replacement, the 95% Confidence Intervals for Arias Intensity, sustained maximum acceleration, EDA, and damage index were computed as [0.27-0.45], [0.37-0.73], [0.85-0.96], and [0.26-0.40], respectively. These damage thresholds are intended for use with concrete gravity dams 50–150 m in height, under MS–AS sequences where both PGAs are scaled to 0.5g with 5% Rayleigh damping. They may not be directly extended to other dam types, geometries, damping ratios, or seismic intensity ranges without further validation. Given the small sample size (14 cases), these values should be regarded as empirical indicators, with larger datasets needed for rigorous statistical inference.

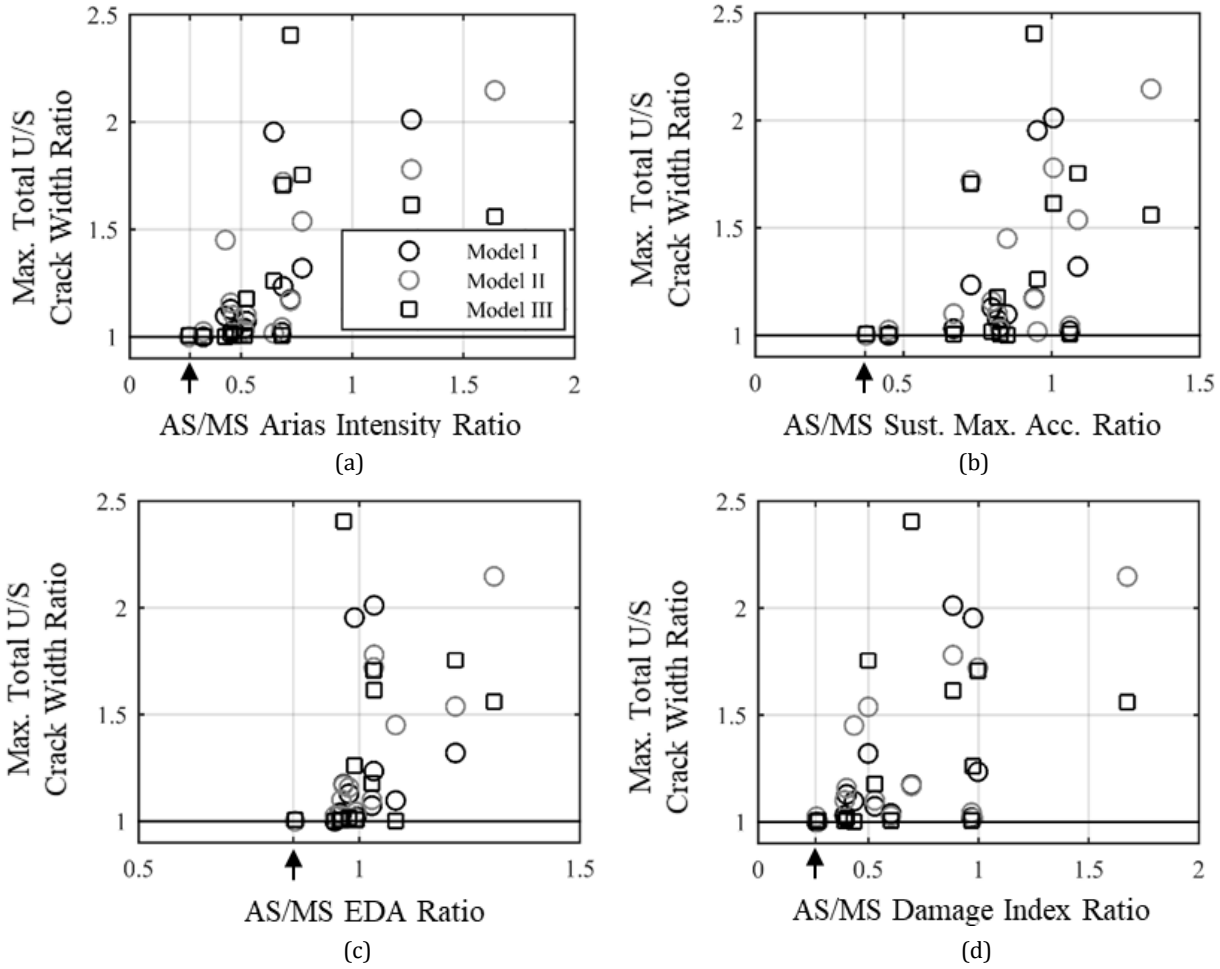

Fig. 7. Ground motion intensity measures on the damage to concrete gravity dam-reservoir systems for 0.5g scaled AS PGA: (a) Arias Intensity; (b) Sustained maximum acceleration; (c) Effective design acceleration; (d) Damage index.

7. Conclusions

This study investigated the seismic performance of three concrete gravity dam-reservoir systems (Model I – 50 m, Model II – 100 m, Model III – 150 m) under as-recorded main shock–aftershock (MS–AS) earthquake sequences using the Modified Applied Element Method (MAEM). Horizontal and vertical components of ground motions were applied in nonlinear transient analyses, and damage was quantified using discrete measures of base crack length, maximum base crack width, and maximum total crack width on the upstream (U/S) face. The use of MAEM provided mechanistic insight into how aftershocks influenced crack patterns and damage accumulation in concrete gravity dams, thereby addressing dam safety.

The results obtained in this study are summarized as follows:

- The rest times between MS-AS sequences ranged from 2.2 to 6.7 s. As the dam height increases, the natural frequency decreases, requiring longer times for taller dams. The empirical Eqs. (5–7) predict these rest times for dams with 50-150 m heights under a PGA range of 0.05g-1.02g with 5% Rayleigh damping.
- Under the same scaling factor, AS primarily propagated existing cracks through stress concentrations formed at crack tips, which was most evident at the base of Model I. In taller dams, in addition to propagation, new cracks developed along the upstream face due to the effects of higher vibration modes and hydrodynamic pressures.
- At 0.3g–0.4g AS intensities, AS generally widened existing upstream cracks or initiated new ones, with limited extension of base cracks. New upstream cracks became more frequent at 0.5g intensity, especially in taller dams. At this seismicity level, the AS increased the maximum total crack width on the upstream face by approximately 25–30% on average, across all models.
- The evaluation of the severity of cracks according to RILEM TC 104 (1991) classification revealed that Model I remained within the mild category across all cases, while Models II and III occasionally reached moderate damage levels both at the base and upstream regions. Since the upstream cracks are in direct contact with the reservoir, they may pose direct hydraulic safety risks. Therefore, even moderate crack openings may increase the potential for seepage, internal erosion, or localized instability, thereby compromising dam functionality.
- A 93% probability was observed for increased maximum total crack width on the upstream face in the three dam systems when the ratios of 0.5g scaled AS to 0.5g scaled MS exceeded 0.27 for Arias Intensity, 0.37 for sustained maximum acceleration, 0.85 for effective design acceleration, and 0.26 for damage index. 95% Confidence Intervals were determined using 10000 bootstrap resamples: [0.27–0.45] for Arias Intensity, [0.37–0.73] for sustained maximum acceleration, [0.85–0.96] for effective design acceleration, and [0.26–0.40] for damage index. These threshold intervals are empirical, with larger datasets needed for rigorous statistical inference.

With a focus on assessing cracking on dam bodies, the soil-structure interaction was not modeled; therefore, the results are applicable for monoliths on stiff foundations (i.e., foundation moduli, E_f, over structure moduli, E_s, more than 4), or for monoliths in narrow valleys with $E_f/E_s < 2$ (Bybordiani and Arici 2017).

This study demonstrates that aftershocks can significantly amplify damage in concrete gravity dams, particularly in taller dams, through combined crack propagation and initiation mechanisms. The findings provide guidance for assessing dam vulnerability, prioritizing inspections, evaluating hydraulic risks from upstream cracking, and incorporating sequential seismic events into design and emergency planning.

Appendix A. Selected earthquake ground motions

The selected 124 acceleration records for the estimation of the required time interval between main shocks and aftershocks are presented in Table A1.

Table A1. Selected earthquake motions.

#	Year	Event	Station	Comp	Mag	R (km)	PGA (g)
1	1966	Parkfield	Cholame Shandon Array	50	6.2 (M_w)	17.6	0.06
2	1966	Parkfield	Cholame Shandon Array	320	6.2 (M_w)	17.6	0.06
3	1971	San Fernando	LA - Hollywood Stor FF	90	6.6 (M_w)	22.8	0.22
4	1971	San Fernando	LA - Hollywood Stor FF	180	6.6 (M_w)	22.8	0.19
5	1971	San Fernando	Lake Hughes 4	111	6.6 (M_w)	19.5	0.20
6	1971	San Fernando	Lake Hughes 4	201	6.6 (M_w)	19.5	0.16
7	1979	Imperial Valley-06	Agrarias	3	6.5 (M_w)	0.0	0.29
8	1979	Imperial Valley-06	Agrarias	273	6.5 (M_w)	0.0	0.19
9	1979	Imperial Valley-06	El Centro Array 7	140	6.5 (M_w)	0.6	0.34
10	1979	Imperial Valley-06	El Centro Array 7	230	6.5 (M_w)	0.6	0.47
11	1979	Imperial Valley-06	Holtville Post Office	225	6.5 (M_w)	5.4	0.26

12	1979	Imperial Valley-06	Holtville Post Office	315	6.5 (M_w)	5.4	0.22
13	1979	Imperial Valley-06	Victoria	75	6.5 (M_w)	31.9	0.12
14	1979	Imperial Valley-06	Victoria	345	6.5 (M_w)	31.9	0.17
15	1980	Mammoth Lakes-01	Long Valley Dam (Upr L Abut)	0	6.1 (M_w)	12.6	0.43
16	1980	Mammoth Lakes-01	Long Valley Dam (Upr L Abut)	90	6.1 (M_w)	12.6	0.27
17	1980	Mammoth Lakes-01	Mammoth Lakes H. S.	254	6.1 (M_w)	4.5	0.32
18	1980	Mammoth Lakes-01	Mammoth Lakes H. S.	344	6.1 (M_w)	4.5	0.24
19	1980	Mammoth Lakes-02	Long Valley Dam (Upr L Abut)	0	5.7 (M_w)	14.3	0.19
20	1980	Mammoth Lakes-02	Long Valley Dam (Upr L Abut)	90	5.7 (M_w)	14.3	0.07
21	1980	Irpinia, Italy-01	Auletta	0	6.9 (M_w)	9.5	0.06
22	1980	Irpinia, Italy-01	Auletta	270	6.9 (M_w)	9.5	0.06
23	1980	Irpinia, Italy-01	Bagnoli Irpinio	0	6.9 (M_w)	8.1	0.13
24	1980	Irpinia, Italy-01	Bagnoli Irpinio	270	6.9 (M_w)	8.1	0.19
25	1980	Irpinia, Italy-01	Brienza	0	6.9 (M_w)	22.5	0.22
26	1980	Irpinia, Italy-01	Brienza	270	6.9 (M_w)	22.5	0.18
27	1980	Irpinia, Italy-01	Rionero In Vulture	0	6.9 (M_w)	27.5	0.10
28	1980	Irpinia, Italy-01	Rionero In Vulture	270	6.9 (M_w)	27.5	0.10
29	1980	Irpinia, Italy-02	Bagnoli Irpinio	0	6.2 (M_w)	17.8	0.06
30	1980	Irpinia, Italy-02	Bagnoli Irpinio	270	6.2 (M_w)	17.8	0.05
31	1983	Mammoth Lakes-11	Convict Creek	90	5.3 (M_w)	7.1	0.15
32	1983	Mammoth Lakes-11	Convict Creek	180	5.3 (M_w)	7.1	0.09
33	1983	Coalinga-05	Oil City	270	5.8 (M_w)	2.0	0.84
34	1983	Coalinga-05	Oil City	360	5.8 (M_w)	2.0	0.42
35	1983	Coalinga-05	Oil Fields Fire Station - FF	270	5.8 (M_w)	6.3	0.22
36	1983	Coalinga-05	Oil Fields Fire Station - FF	360	5.8 (M_w)	6.3	0.19
37	1983	Coalinga-05	Transmitter Hill	270	5.8 (M_w)	3.7	0.78
38	1983	Coalinga-05	Transmitter Hill	360	5.8 (M_w)	3.7	1.02
39	1984	Morgan Hill	Gilroy Array 2	0	6.2 (M_w)	13.7	0.16
40	1984	Morgan Hill	Gilroy Array 2	90	6.2 (M_w)	13.7	0.21
41	1986	N. Palm Springs	San Jacinto - Valley Cemetary	270	6.1 (M_w)	30.7	0.07
42	1986	N. Palm Springs	San Jacinto - Valley Cemetary	360	6.1 (M_w)	30.7	0.06
43	1986	N. Palm Springs	Sunnymead	225	6.1 (M_w)	37.7	0.10
44	1986	N. Palm Springs	Sunnymead	315	6.1 (M_w)	37.7	0.12
45	1986	Chalfant Valley-02	Benton	270	6.2 (M_w)	21.6	0.21
46	1986	Chalfant Valley-02	Benton	360	6.2 (M_w)	21.6	0.18
47	1986	Chalfant Valley-02	Bishop - Paradise Lodge	70	6.2 (M_w)	15.0	0.17
48	1986	Chalfant Valley-02	Bishop - Paradise Lodge	160	6.2 (M_w)	15.0	0.16
49	1987	Whittier Narrows-01	Alhambra - Fremont School	180	6.0 (M_w)	1.7	0.29
50	1987	Whittier Narrows-01	Alhambra - Fremont School	270	6.0 (M_w)	1.7	0.39
51	1987	Whittier Narrows-01	Glendale - Las Palmas	177	6.0 (M_w)	14.7	0.30
52	1987	Whittier Narrows-01	Glendale - Las Palmas	267	6.0 (M_w)	14.7	0.18
53	1987	Whittier Narrows-01	Glendora - N Oakbank	80	6.0 (M_w)	13.7	0.10
54	1987	Whittier Narrows-01	Glendora - N Oakbank	170	6.0 (M_w)	13.7	0.11
55	1987	Whittier Narrows-01	LA - Century City CC North	0	6.0 (M_w)	26.1	0.07
56	1987	Whittier Narrows-01	LA - Century City CC North	90	6.0 (M_w)	26.1	0.10
57	1987	Whittier Narrows-01	Pasadena - CIT Kresge Lab	90	6.0 (M_w)	6.8	0.11
58	1987	Whittier Narrows-01	Pasadena - CIT Kresge Lab	360	6.0 (M_w)	6.8	0.09
59	1987	Whittier Narrows-01	Pomona - 4th & Locust FF	12	6.0 (M_w)	25.1	0.07
60	1987	Whittier Narrows-01	Pomona - 4th & Locust FF	102	6.0 (M_w)	25.1	0.05

61	1987	Whittier Narrows-02	Alhambra - Fremont School	180	5.3 (M_w)	3.6	0.18
62	1987	Whittier Narrows-02	Alhambra - Fremont School	270	5.3 (M_w)	3.6	0.21
63	1987	Whittier Narrows-02	LA - Hollywood Stor FF	90	5.3 (M_w)	21.0	0.05
64	1987	Whittier Narrows-02	LA - Hollywood Stor FF	360	5.3 (M_w)	21.0	0.09
65	1989	Loma Prieta	Point Bonita	207	6.9 (M_w)	83.4	0.07
66	1989	Loma Prieta	Point Bonita	297	6.9 (M_w)	83.4	0.07
67	1989	Loma Prieta	So. San Francisco, Sierra Pt.	115	6.9 (M_w)	63.0	0.05
68	1989	Loma Prieta	So. San Francisco, Sierra Pt.	205	6.9 (M_w)	63.0	0.11
69	1992	Landers	Mission Creek Fault	0	7.3 (M_w)	27.0	0.13
70	1992	Landers	Mission Creek Fault	90	7.3 (M_w)	27.0	0.13
71	1994	Northridge-01	Beverly Hills - 12520 Mulhol	35	6.7 (M_w)	12.4	0.62
72	1994	Northridge-01	Beverly Hills - 12520 Mulhol	125	6.7 (M_w)	12.4	0.45
73	1994	Northridge-01	Burbank - Howard Rd.	60	6.7 (M_w)	15.9	0.11
74	1994	Northridge-01	Burbank - Howard Rd.	330	6.7 (M_w)	15.9	0.16
75	1994	Northridge-01	LA - Centinela St	155	6.7 (M_w)	20.4	0.45
76	1994	Northridge-01	LA - Centinela St	245	6.7 (M_w)	20.4	0.32
77	1994	Northridge-01	LA - Obregon Park	90	6.7 (M_w)	35.4	0.35
78	1994	Northridge-01	LA - Obregon Park	360	6.7 (M_w)	35.4	0.56
79	1994	Northridge-01	LA - Wonderland Ave	95	6.7 (M_w)	15.1	0.10
80	1994	Northridge-01	LA - Wonderland Ave	185	6.7 (M_w)	15.1	0.16
81	1994	Northridge-01	LA 00	180	6.7 (M_w)	9.9	0.26
82	1994	Northridge-01	LA 00	270	6.7 (M_w)	9.9	0.38
83	1994	Northridge-01	Lake Hughes 12A	90	6.7 (M_w)	20.8	0.17
84	1994	Northridge-01	Lake Hughes 12A	180	6.7 (M_w)	20.8	0.26
85	1994	Northridge-01	Santa Monica City Hall	90	6.7 (M_w)	17.3	0.88
86	1994	Northridge-01	Santa Monica City Hall	360	6.7 (M_w)	17.3	0.37
87	1994	Northridge-01	Sylmar - Converter Sta East	11	6.7 (M_w)	0.0	0.85
88	1994	Northridge-01	Sylmar - Converter Sta East	281	6.7 (M_w)	0.0	0.45
89	1999	Kocaeli, Turkey	Arcelik	0	7.5 (M_w)	10.6	0.21
90	1999	Kocaeli, Turkey	Arcelik	90	7.5 (M_w)	10.6	0.13
91	1999	Chi-Chi, Taiwan	CHY035	E	7.6 (M_w)	12.6	0.25
92	1999	Chi-Chi, Taiwan	CHY035	N	7.6 (M_w)	12.6	0.25
93	1999	Chi-Chi, Taiwan	CHY042	E	7.6 (M_w)	27.5	0.10
94	1999	Chi-Chi, Taiwan	CHY042	N	7.6 (M_w)	27.5	0.07
95	1999	Chi-Chi, Taiwan	CHY052	N	7.6 (M_w)	38.7	0.15
96	1999	Chi-Chi, Taiwan	CHY052	W	7.6 (M_w)	38.7	0.09
97	1999	Hector Mine	Twentynine Palms	90	7.1 (M_w)	42.1	0.07
98	1999	Hector Mine	Twentynine Palms	360	7.1 (M_w)	42.1	0.07
99	1999	Chi-Chi, Taiwan-03	TCU079	E	6.2 (M_w)	0.0	0.34
100	1999	Chi-Chi, Taiwan-03	TCU079	N	6.2 (M_w)	0.0	0.27
101	1999	Chi-Chi, Taiwan-04	CHY035	E	6.2 (M_w)	25.0	0.13
102	1999	Chi-Chi, Taiwan-04	CHY035	N	6.2 (M_w)	25.0	0.12
103	1999	Chi-Chi, Taiwan-05	TCU054	E	6.2 (M_w)	45.3	0.06
104	1999	Chi-Chi, Taiwan-05	TCU054	N	6.2 (M_w)	45.3	0.05
105	1999	Chi-Chi, Taiwan-06	TCU075	E	6.3 (M_w)	24.3	0.11
106	1999	Chi-Chi, Taiwan-06	TCU075	N	6.3 (M_w)	24.3	0.06
107	1999	Chi-Chi, Taiwan-06	TCU120	E	6.3 (M_w)	30.9	0.06
108	1999	Chi-Chi, Taiwan-06	TCU120	N	6.3 (M_w)	30.9	0.06
109	2009	L'Aquila, Italy	L'Aquila - V. Aterno - Colle Grilli	E	6.3 (M_w)	0.0	0.48

110	2009	L'Aquila, Italy	L'Aquila - V. Aterno - Colle Grilli	N	6.3 (M_w)	0.0	0.52
111	2009	L'Aquila (aftershock 1), Italy	L'Aquila - V. Aterno - Colle Grilli	E	5.6 (M_w)	11.1	0.15
112	2009	L'Aquila (aftershock 1), Italy	L'Aquila - V. Aterno - Colle Grilli	N	5.6 (M_w)	11.1	0.11
113	2008	Iwate, Japan	IWTH17	EW	6.9 (M_w)	72.4	0.06
114	2008	Iwate, Japan	IWTH17	NS	6.9 (M_w)	72.4	0.06
115	2008	Iwate, Japan	MYG011	EW	6.9 (M_w)	82.9	0.06
116	2008	Iwate, Japan	MYG011	NS	6.9 (M_w)	82.9	0.08
117	1995	Kozani, Greece	ITSAK	90	6.1 (M_L)	19.5	0.14
118	1995	Kozani, Greece	ITSAK	90	5.3 (M_L)	12.1	0.12
119	1980	Mammoth Lakes	54099 Convict Creek	90	6.1 (M_L)	9.1	0.41
120	1980	Mammoth Lakes	54099 Convict Creek	90	5.7 (M_L)	3.4	0.35
121	1995	Kozani, Greece	ITSAK	0	6.1 (M_L)	19.5	0.22
122	1995	Kozani, Greece	ITSAK	0	5.3 (M_L)	12.1	0.13
123	1980	Mammoth Lakes	54099 Convict Creek	180	6.1 (M_L)	9.1	0.40
124	1980	Mammoth Lakes	54099 Convict Creek	180	5.7 (M_L)	3.4	0.50

The 14 ground motion records to evaluate the seismic performances of concrete gravity dam-reservoir systems are given in Table A2.

Table A2. Selected main shocks-aftershocks.

#	MS/AS	Year	Event	Station	Comp	Mag	R (km)	PGA (g)
1	MS	1980	Mammoth Lakes-01	Long Valley Dam (Upr L Abut)	0	6.1 (M_w)	12.6	0.43
	AS	1980	Mammoth Lakes-02	Long Valley Dam (Upr L Abut)	0	5.7 (M_w)	14.3	0.19
2	MS	1980	Mammoth Lakes-01	Long Valley Dam (Upr L Abut)	90	6.1 (M_w)	12.6	0.27
	AS	1980	Mammoth Lakes-02	Long Valley Dam (Upr L Abut)	90	5.7 (M_w)	14.3	0.07
3	MS	1980	Irpinia, Italy-01	Bagnoli Irpinio	0	6.9 (M_w)	8.1	0.13
	AS	1980	Irpinia, Italy-02	Bagnoli Irpinio	0	6.2 (M_w)	17.8	0.06
4	MS	1980	Irpinia, Italy-01	Bagnoli Irpinio	270	6.9 (M_w)	8.1	0.19
	AS	1980	Irpinia, Italy-02	Bagnoli Irpinio	270	6.2 (M_w)	17.8	0.05
5	MS	1987	Whittier Narrows-01	Alhambra - Fremont School	180	6.0 (M_w)	1.7	0.29
	AS	1987	Whittier Narrows-02	Alhambra - Fremont School	180	5.3 (M_w)	3.6	0.18
6	MS	1987	Whittier Narrows-01	Alhambra - Fremont School	270	6.0 (M_w)	1.7	0.39
	AS	1987	Whittier Narrows-02	Alhambra - Fremont School	270	5.3 (M_w)	3.6	0.21
7	MS	1999	Chi-Chi, Taiwan	CHY035	E	7.6 (M_w)	12.6	0.25
	AS	1999	Chi-Chi, Taiwan-04	CHY035	E	6.2 (M_w)	25.0	0.13
8	MS	1999	Chi-Chi, Taiwan	CHY035	N	7.6 (M_w)	12.6	0.25
	AS	1999	Chi-Chi, Taiwan-04	CHY035	N	6.2 (M_w)	25.0	0.12
9	MS	2009	L'Aquila, Italy	L'Aquila - V. Aterno - Colle Grilli	E	6.3 (M_w)	0.0	0.48
	AS	2009	L'Aquila (aftershock 1), Italy	L'Aquila - V. Aterno - Colle Grilli	E	5.6 (M_w)	11.1	0.15
10	MS	2009	L'Aquila, Italy	L'Aquila - V. Aterno - Colle Grilli	N	6.3 (M_w)	0.0	0.52
	AS	2009	L'Aquila (aftershock 1), Italy	L'Aquila - V. Aterno - Colle Grilli	N	5.6 (M_w)	11.1	0.11
11	MS	1995	Kozani, Greece	ITSAK	0	6.1 (M_L)	19.5	0.22
	AS	1995	Kozani, Greece	ITSAK	0	5.3 (M_L)	12.1	0.13
12	MS	1995	Kozani, Greece	ITSAK	90	6.1 (M_L)	19.5	0.14
	AS	1995	Kozani, Greece	ITSAK	90	5.3 (M_L)	12.1	0.12
13	MS	1980	Mammoth Lakes	54099 Convict Creek	180	6.1 (M_L)	9.1	0.40
	AS	1980	Mammoth Lakes	54099 Convict Creek	180	5.7 (M_L)	3.4	0.50
14	MS	1980	Mammoth Lakes	54099 Convict Creek	90	6.1 (M_L)	9.1	0.41
	AS	1980	Mammoth Lakes	54099 Convict Creek	90	5.7 (M_L)	3.4	0.35

Acknowledgements

None declared.

Funding

The author received no financial support for the research, authorship, and/or publication of this manuscript.

Conflict of Interest

The author declared no potential conflicts of interest with respect to the research, authorship, and/or publication of this manuscript.

Author Contributions

The author confirms sole responsibility for all aspects of the study including conception and design, acquisition of data, analysis and interpretation of data, drafting the manuscript, revising it critically for important intellectual content; and gave final approval of the version to be published.

Data Availability

The datasets created and/or analyzed during the current study are not publicly available, but are available from the corresponding author upon reasonable request.

REFERENCES

Akköse M, Dumanoğlu AA, Bayraktar A (2016). Seismic analysis of arch dams subjected to in-phase and anti-phase ground motions. *Challenge Journal of Structural Mechanics*, 2(2), 85-92.

Akpinar U, Arici Y, Binici B (2023). Post-earthquake effects on the seismic performance of concrete gravity dams. *Structure and Infrastructure Engineering*, 21(1), 10-23.

Alliard PM, Leger P (2008). Earthquake safety evaluation of gravity dams considering aftershocks and reduced drainage efficiency. *Journal of Engineering Mechanics*, 134, 12-22.

Amadio C, Fragiacomo M, Rajgelj S (2003). The effects of repeated earthquake ground motions on the non-linear response of SDOF systems. *Earthquake Engineering & Structural Dynamics*, 32, 291-308.

Ashna KN, Maheshwari P, Viladkar MN (2024). Fragility analysis of a concrete gravity dam under mainshock-aftershock sequences. *Structures*, 61, 106117.

Bybordiani M, Arici Y (2017). The use of 3D modeling for the prediction of the seismic demands on the gravity dams. *Earthquake Engineering & Structural Dynamics*, 46(11), 1769-1789.

Carpinteri A, Valente S, Ferrara G, Imperato L (1992). Experimental and numerical fracture modelling of a gravity dam. *ACI Symposium Publication*, 143, 107-122.

Chen D-H, Yang Z-H, Wang M, Xie J-H (2019). Seismic performance and failure modes of the Jin'anqiao concrete gravity dam based on incremental dynamic analysis. *Engineering Failure Analysis*, 100, 227-244.

Chopra AK (1978). Earthquake resistant design of concrete gravity dams. *Journal of the Structural Division*, 104, 953-971.

Fahlbusch H (2009). Early dams. *Proceedings of the Institution of Civil Engineers – Engineering History and Heritage*, 162(1), 13-18.

Faisal A, Majid TA, Hatzigeorgiou GD (2013). Investigation of story ductility demands of inelastic concrete frames subjected to repeated earthquakes. *Soil Dynamics and Earthquake Engineering*, 44, 42-53.

Fragiacomo M, Amadio C, Macorini L (2004). Seismic response of steel frames under repeated earthquake ground motions. *Engineering Structures*, 24, 2021-2035.

Ghallab A (2020). Simulation of cracking in high concrete gravity dam using the Extended Finite Elements by ABAQUS. *American Journal of Mechanics and Applications*, 8(1), 7-15.

Gopalaratnam VS, Shah SP (1985). Softening response of plain concrete in direct tension. *Journal of the American Concrete Institute*, 82(3), 310-323.

Guo X, Zhang Z, Chen ZQ (2020). Mainshock-integrated aftershock vulnerability assessment of bridge structures. *Applied Sciences*, 10, 6843.

Hacıefendioğlu K, Akköse M, Bayraktar A, Dumanoğlu AA (2015). Shear strain related non-linear stochastic dynamic analysis of rock-fill dams. *Challenge Journal of Structural Mechanics*, 1(2), 59-64.

Hariri-Ardebili MA, Kianoush MR (2014). Integrative seismic safety evaluation of a high concrete arch dam. *Soil Dynamics and Earthquake Engineering*, 67, 85-101.

Hariri-Ardebili MA, Saouma VE (2016). Collapse fragility curves for concrete dams: comprehensive study. *Journal of Structural Engineering*, 142(10), 04016075.

Hatzigeorgiou GD (2010). Behavior factors for nonlinear structures subjected to multiple near-fault earthquakes. *Computers & Structures*, 88, 309-321.

Hatzigeorgiou GD, Beskos DE (2009). Inelastic displacement ratios for SDOF structures subjected to repeated earthquakes. *Engineering Structures*, 31, 2744-2755.

Huang J (2014). Effects of near-fault ground motions on the seismic performance of concrete gravity dams. *Proceedings of the 9th International Conference of Structural Dynamics*, *EURODYN 2014*, Porto, Portugal.

International Commission on Large Dams (2023). World Register of Dams (Database Presentation), International Commission on Large Dams. https://www.icold-cigb.org/GB/world_register/database_presentation.asp [accessed 21-2-2024].

Khanal A (2019). Seismic Performance of Earth Slopes Subjected to Earthquake Mainshock – Aftershock Sequences. *M.Sc. thesis*, University of Texas at Tyler, Texas, USA.

Leger P, Leclerc M (1996). Evaluation of earthquake ground motions to predict cracking response of gravity dams. *Engineering Structures*, 18(3), 227-239.

Li Y, Song R, van de Lindt JW (2014). Collapse fragility of steel structures subjected to earthquake mainshock-aftershock sequences. *Journal of Structural Engineering*, 140(12), 04014095.

Lokke A, Chopra AK (2013). Response Spectrum Analysis of Concrete Gravity Dams Including Dam-Water-Foundation Interaction. PEER Report 2013/17, Pacific Earthquake Engineering Research Center, Headquarters at the University of California, Berkeley.

Maekawa K, Okamura H, Pimanmas A (2003). Non-Linear Mechanics of Reinforced Concrete. 1st ed. CRC Press, London, UK.

Mangalathu S, Shokrabadi M, Burton HV (2019). Aftershock Seismic Vulnerability and Time-Dependent Risk Assessment of Bridges. PEER Report 2019/04, Pacific Earthquake Engineering Research Center, Headquarters at the University of California, Berkeley.

Meguro K, Tagel-Din H (2000). Applied element method for structural analysis: theory and application for linear materials. *Structural Engineering/Earthquake Engineering*, 17(1), 21s–35s.

Mignan A (2014). The debate on the prognostic value of earthquake foreshocks: A meta-analysis. *Scientific Reports*, 4, 4099.

Mooney CZ, Duval RD (1993). Bootstrapping: A Nonparametric Approach to Statistical Inference. Sage University Paper Series on Quantitative Applications in the Social Sciences, 07-095. Newbury Park, CA, USA.

Pang R, Xu B, Zhang X, Zhou Y, Kong X (2019). Seismic performance investigation of high CFRDs subjected to mainshock-aftershock sequences. *Soil Dynamics and Earthquake Engineering*, 116, 82-85.

Pekau OA, Zhu X (2008). Effect of seismic uplift pressure on the behavior of concrete gravity dams with a penetrated crack. *Journal of Engineering Mechanics*, 134(11), 991-999.

Pirooz RM, Habashi S, Massumi A (2021). Required time gap between mainshock and aftershock for dynamic analysis of structures. *Bulletin of Earthquake Engineering*, 19, 2643-2670.

RILEM TC 104 (1991). Damage classification of concrete structures. The state of the art report of RILEM Technical Committee 04-DCC activity. *Materials and Structures*, 24(142), 253-259.

Risk Management Solutions (2008). Risk Management Solutions Reconnaissance Report: The 2008 Wenchuan Earthquake: Risk Management Lessons and Implications. Risk Management Solutions, Newark, CA, USA.

Sadeghi MH, Moradloo J (2022). Seismic analysis of damaged concrete gravity dams subjected to mainshock-aftershock sequences. *European Journal of Environmental and Civil Engineering*, 26, 2417-2438.

Sommerfeld A (1949). Partial Differential Equations in Physics. 1st ed. Academic Press, New York.

Soysal Albostan BF (2021). Discrete Element Based Analyses of Structure-Reservoir Problem for Gravity Dams. *Ph.D. thesis*, Middle East Technical University, Ankara, Turkey.

Soysal BF, Arici Y, Tuncay K (2023). A modified applied element model for the simulation of plain concrete behaviour. *Magazine of Concrete Research*, 75, 325-338.

Soysal BF, Arici Y (2024). The use of discrete element models for the seismic assessment of concrete gravity dams. *Structures*, 70, 107831.

SRC (n.d.). Dams & earthquakes. Seismology Research Centre. https://www.src.com.au/earthquakes/seismology-101/dams-earthquakes [accessed 21-2-2024].

Toikka L, Grover L, Hull A, Rossiter M (2019). Site-specific seismic analysis for concrete gravity dams: a case study from Ontario. *12th Canadian Conference on Earthquake Engineering*, Quebec, QC, Canada, 1-8.

United States Geological Survey (2015). Magnitude 7.8 earthquake Nepal Aftershocks. United States Geological Survey. https://www.usgs.gov/news/featured-story/magnitude-78-earthquake-nepal-aftershocks [accessed 21-2-2024].

Wang G, Wang Y, Lu W, Yan P, Zhou W, Chen M (2017). Damage demand assessment of mainshock-damaged concrete gravity dams subjected to aftershocks. *Soil Dynamics and Earthquake Engineering*, 98, 141-154.

Wang M, Chen J, Wu L, Song B (2018). Hydrodynamic pressure on gravity dams with different heights and the Westergaard correction formula. *International Journal of Geomechanics*, 18(10), 04018134.

Wang G, Wang Y, Lu W, Yan P, Chen M (2020). Earthquake direction effects on seismic performance of concrete gravity dams to mainshock-aftershock sequences. *Journal of Earthquake Engineering*, 24, 1134-1155.

Wang X, Bathe KJ (1997). Displacement/pressure based mixed finite element formulations for acoustic fluid-structure interaction problems. *International Journal for Numerical Methods in Engineering*, 40, 2001-2017.

Wei Q, Shen L, Dunai L, Kövesdi B, Elqudah S, Cao M (2024). Quantitative evaluation on the effects of the spatial variability in concrete materials on seismic damage of concrete gravity dams. *Engineering Fracture Mechanics*, 307, 110287.

Wen R, Zhou Z, Li X, Yang C, Wang Y, Liu Q, Cui J (2009). The strong ground motion observation for the Wenchuan aftershock. *Earthquake Science*, 22, 181–187.

Zhai Y, Zhang L, Bi Z, Zhang H, Cui, B (2022). Seismic performance evaluation of AAR-affected concrete gravity dams under main aftershock sequence. *Soil Dynamics and Earthquake Engineering,* 157, 107258.

Zhang L, Zhai Y, Chen D, Cui X (2019). Study on influence of dam foundation damage on seismic safety of gravity dam under combined action of main shock and aftershock. *IOP Conference Series: Earth and Environmental Science*, 304, 042063.

Zhang L, Zhai Y, Cui B, Tang Y, Bi Z (2021). A novel method for constructing main-aftershock sequences and its application in the global damage accumulation effects analysis of gravity dams. *Shock and Vibration*, 3, 1-12.

Zhang S, Wang G, Sa W (2013). Damage evaluation of concrete gravity dams under mainshock-aftershock seismic sequences. *Soil Dynamics and Earthquake Engineering*, 50, 16-27.